MODELING LOCALIZED HEATING INDUCED SIZE EFFECTS IN SEMICONDUCTOR DEVICES

by

Canberk Dündar

B.S., Mechanical Engineering, Yıldız Technical University, 2017

Submitted to the Institute for Graduate Studies in
Science and Engineering in partial fulfillment of
the requirements for the degree of
Master of Science

Graduate Program in Mechanical Engineering

Boğaziçi University

2020

ACKNOWLEDGEMENTS

I would like to thank my advisor Dr. F. Nazlı Dönmezer Akgün for her invaluable guidance throughout my Master study. Also, I would like to express my gratitude for her mentorship and patience. I would also like to express my deepest appreciation to my committee, for reviewing my work, giving helpful advice, and sharing their constructive criticism.

I would also like to thank Dr. Sukwon Choi so that this research could be completed. Furthermore, This research was supported by the TUBITAK (Grant no: 115E756 and Grant no: 119F049), without either of which this work would not have been possible.

Of course, without the love and support of my parents, this study could not have been possible. I cannot thank my mother and my father enough. I cannot repay them with anything for what they have done for me all this life.

Finally, I would like to thank to Duygu my best friend, lover, and constant source of support.

ABSTRACT

MODELING LOCALIZED HEATING INDUCED SIZE EFFECTS IN SEMICONDUCTOR DEVICES

Micro and nano scale semiconductor devices could undergo localized self-heating that obscures phonon transport and leads to size effects and peak device temperatures. Consequently, device performance and lifetime are degraded. The profile of the localized heating is the main contributor to the size effects and a comprehensive numerical investigation is conducted for understanding profile effects. Also, besides numerical methods, accuracy of micro-Raman and thermoreflectance thermal imaging (TTI) experiments for capturing the peak device temperature is investigated. It was observed that although the aspect ratio of heat generation area alters the size effects, area was found as the main factor. Horizontal and vertical lengths of the profile have dissimilar impact on the peak temperature. Moreover, heat flux boundary simplification is tested with sub-continuum model that could alleviate computational costs. If the heat generation profile laterally spread, the phonon Boltzmann transport equation (BTE) model with boundary flux approximation can estimate the size effects with 0.5-8% errors. Also, this approximation yields ∼0.6-3.1% error in AlGaN/GaN transistor electro-thermal model. Virtual experiments showed that neither the micro-Raman nor the visible TTI can determine the peak temperature in AlGaN/GaN transistor and device structure does not change the accuracy markedly. TTI yields smaller error, nevertheless, it can be up to ∼21°C. Finally, these numerical calculations were proven by the actual visible TTI and the novel UV TTI experiments. The visible TTI experiment and continuum scale models underestimated the device peak temperature by ∼20°C. Furthermore, the agreement between the UV TTI method and the phonon BTE calculations proved the size effects experimentally.

ÖZET

YARI İLETKENLERDE LOKAL ISINMADAN KAYNAKLANAN BOYUT ETKİLERİNİN MODELLENMESİ

Mikro ve nano boyutlardaki yarı iletken cihazlarda görülen lokalize ısı üretimi, fonon taşınımını etkileyip, boyut etkilerine sebep olabilir. Boyut etkileri bu cihazlarda yüksek sıcaklık değerlerinden sorumludur. Ayrıca, cihaz performansı ve ömrünü olumsuz etkiler. Lokalize ısınma profili boyut etkilerinin ana etkenlerindendir ve profil etkilerinin anlaşılabilmesi için detaylı bir nümerik çalışma yürütülmüştür. Bununla birlikte, yarı iletken cihazlarda sıcaklık ölçümünde kullanılan mikro-Raman ve TTI deneysel yöntemlerinin, boyut etkilerini ölçebilme doğruluğu incelenmiştir. Sonuçlar, ısınma profilinin en-boy oranının etkisine rağmen, alan büyüklüğünün en etkin faktör olduğunu göstermiştir. Yatay ve dikey uzunlukların etkisi ise farklıdır. Bununla birlikte, sınır ısı akısı yaklaşımının doğruluğu, fonon taşınımının dahil edildiği termal model ile test edilmiştir. Sınır akısı yaklaşımı fonon BTE ile çözüldüğünde, yatayda yayılmış üretim profillerinin oluşturduğu boyut etkilerini %0.5-8 hata ile hesaplayabildiği görülmüştür. Ayrıca, aynı yaklaşım AlGaN/GaN elektro-termal modelinde boyut etkilerini %∼0.6-3.1 hata ile hesaplamıştır. Sanal deney sonuçları, mikro-Raman ve TTI yöntemlerinin gerçek cihaz sıcaklığını hesaplayamayacağını göstermiştir. Cihaz yapısının deneysel yönteme etkisinin az olduğu görülmüştür. Son olarak, nümerik hesaplamalar görünür TTI ve UV TTI gerçek deneyleri ile ispatlanmıştır. Görünür TTI ve sürekli termal model, pik sıcaklığı ∼20°C daha az hesaplamıştır. UV TTI ve fonon BTE sonuçlarının uyumu ise, boyut etkilerini deneysel olarak kanıtlamıştır.

TABLE OF CONTENTS

ACKNOWLEDGEMENTS i
ABSTRACT ii
ÖZET iii
LIST OF FIGURES vi
LIST OF TABLES xi
LIST OF SYMBOLS xii
LIST OF ACRONYMS/ABBREVIATIONS xvii
1. INTRODUCTION 1
1.1. Semiconductor Materials 1
1.2. Semiconductor Devices 3
1.3. Localized Self-Heating in Semiconductor Devices 6
1.4. Thermal Characterization of Localized Heating 9
1.4.1. Thermal Models and Size Effects 10
1.4.2. Experiments 16
1.5. Motivation 18
1.6. Outline of Thesis 19
2. SIZE EFFECTS CAUSED BY JOULE HEATING 20
2.1. Continuum Model 22
2.2. Sub-continuum Model 26
2.2.1. Gray Model and Relaxation Time Approximation 29
2.2.2. Finite Volume Discrete Ordinates Method 32
2.2.2.1. Angular Discretization of Phonon BTE 33
2.2.2.2. Spatial Discretization of Phonon BTE 35
2.3. Results 46
3. A CASE STUDY: AlGaN/GaN HEMTS 51
3.1. AlGaN/GaN HEMTs and Joule Heating Profile 51
3.2. Multiscale Model 56
3.2.1. Electrical Model 59

3.2.2. Thermal Models 65
3.2.2.1. Continuum Scale Thermal Model 65
3.2.2.2. Sub-continuum Scale Thermal Model 67
3.3. Results 68
4. COMPARISON OF THERMAL MODELS WITH EXPERIMENTS 76
4.1. Virtual Experiment 76
4.1.1. Micro-Raman 76
4.1.2. Thermoreflectance Thermal Imaging 79
4.1.3. Model 81
4.1.4. Results 84
4.2. Actual Experiments 89
4.2.1. Device Structure and Continuum Model 89
4.2.2. Visible TTI Measurements 93
4.2.3. UV TTI Measurements 95
4.2.4. Sub-continuum Model 99
5. CONCLUSIONS AND FUTURE RESEARCH 103
REFERENCES 107

LIST OF FIGURES

Figure 1.1. (a) and (b) represent partially filled states and overlapped bands such as in metals. Insulators and semiconductors are depicted by (c) and (d), respectively. 1

Figure 1.2. Semiconductor applications: (a) base station, (b) LED, (c) Quantum well laser. 4

Figure 1.3. Operation fields of semiconductor materials. 6

Figure 1.4. AlGaN/GaN HEMT (a) device structure, (b) Localized heat generation. 7

Figure 1.5. (a) FinFet and heat generation profile and (b) quasi-vertical and vertical GaN diode. 8

Figure 1.6. Arrhenius plot of GaN-on-Si transistor. 9

Figure 1.7. Thermal model for GaN HEMT: (a) Device and (b) mesh structure. 10

Figure 1.8. Monatomic lattice chain representation. 11

Figure 1.9. Dispersion for the monatomic lattice chain. 13

Figure 1.10. Phonon-phonon scattering (P_1, P_2 and P_3 refer to different phonons.). 14

Figure 1.11. Diffusive (COMSOL) and sub-continuum (DOM) solution difference in the device channel. 15

Figure 1.12. Thermoreflectance thermal imaging of GaN HEMT. 17

Figure 2.1. The investigated domain with (a) volumetric heat generation and (b) heat flux boundary. 20

Figure 2.2. Transition from (a) heat generation to (b) heat flux. 21

Figure 2.3. (a) Spatial discretization according to finite volume method, (b) nodes depending on grid number. 23

Figure 2.4. Phonon dispersion curve of GaN. 28

Figure 2.5. (a) Spatial discretization according to finite volume method, (b) angular discretization. 32

Figure 2.6. (a) SN quadratures in an octant in which each different number implies different weighing factor, (b) S4 quadratures in an octant. 34

Figure 2.7. (a) Specular reflection boundary condition, (b) diffuse reflection boundary condition. 42

Figure 2.8. Discrepanies between continuum and sub-continuum approach in terms of volumetric heat generation. 46

Figure 2.9. Discrepancy between continuum and sub-continuum approach in terms of heat flux boundary application. 48

Figure 2.10. Deviation between heat flux and volumetric heat generation results in phonon BTE. 49

Figure 3.1. 2-D structure of AlGaN/GaN HEMT. 51

Figure 3.2. I-V curve of an AlGaN/GaN HEMT. 53

Figure 3.3. Hotspot in AlGaN/GaN HEMT. 54

Figure 3.4. Joule heating profile in AlGaN/GaN HEMT operating at P =4 W/mm. (a) and (c) show device with gate field plate structure, (b) and (d) represents devices without field plate. 55

Figure 3.5. 2-D structure of the (a) investigated AlGaN/GaN HEMT and (b) single finger of the device. 57

Figure 3.6. Process for multiscale model. 58

Figure 3.7. Device model for electrical simulation. 63

Figure 3.8. I-V curve for the modeled device. 64

Figure 3.9. 3-D thermal model for diffusive device simulation. 66

Figure 3.10. Sub-continuum model for the device. 67

Figure 3.11. Heat generation distribution when device operates at (a) V_G=0, P= 1 W/mm, (b) V_G=0, P= 2 W/mm, (c) V_G=-2 V, P= 1 W/mm, (d) V_G=-2 V, P= 2 W/mm. 69

Figure 3.12. Integrated Joule heating data of (a) P = 1 W/mm, (b) P = 2 W/mm. 71

Figure 3.13. Temperature distribution in the device channel when the device operates with (a) V_G= 0 V, (b) V_G = - 2 V. 72

Figure 3.14. Difference between volumetric heat generation and the heat flux boundary approximations. 74

Figure 4.1. Raman shift with the temperature change in GaN 77

Figure 4.2. Micro-Raman probe region. 78

Figure 4.3. Thermoreflectance. 79

Figure 4.4. CCD-based TTI setup. 81

Figure 4.5. Micro-Raman and TTI probe regions in the (a) non-field plated and (b) field plated AlGaN/GaN HEMT. 82

Figure 4.6. Location of the numerical micro-Raman and TTI experiment results in the electro-thermal model coupled with the phonon BTE. 83

Figure 4.7. Temperature distribution in the 2DEG when the V_G = -2 V for (a) field plated and (b) non-field plated device. 85

Figure 4.8. Micro-Raman deviation from the device peak temperature with (a) Fourier estimation and (b) phonon BTE estimation. 86

Figure 4.9. TTI deviation from the device peak temperature with (a) Fourier estimation and (b) phonon BTE estimation. 87

Figure 4.10. (a) 2-D scheme of the fabricated AlGaN/GaN HEMT. (b) Optical image of the device by CDD camera used in the TTI measurements. 90

Figure 4.11. I-V curve of the device under DC operating conditions. 91

Figure 4.12. Electro-thermal simulation results for the V_G= -1 V and V_G= 2.5 V when the power is 2.5 W/mm. (a)-(b) Joule heating data for partially pinched-off and fully open channel conditions, respectively. (d)-(e) Surface temperature distributions for partially pinched-off and fully open channel, respectively. 92

Figure 4.13. TTI results when the power is 2.5 W/mm (a)-(b) Illustration of the TTI probe regions. (c) TTI measurement of the device operated with the partially pinched-off (V_G = -1 V) condition. (d) Results for fully open channel condition (V_G = 2.5 V). 94

Figure 4.14. (a) Light source spectrum for both UV and visible sources. (b) Absorption in the device layout related to wavelength. (c) Linearized absorption. 96

Figure 4.15. (a) UV TTI probe region. (b) Probe region representation on the real device. Temperature distribution in the probe region when the power dissipation is 5 W/mm for (c) partially pinched-off and (d) fully open channel conditions. 97

Figure 4.16. UV-TTI, visible TTI, and diffusive simulation comparison for (a) partially pinched-off condition with 2.5 W/mm, (b) fully open channel condition with 2.5 W/mm, (c) partially pinched-off condition with 5 W/mm, (d) fully open channel condition with 5 W/mm. . . 98

Figure 4.17. (a) Phonon BTE domain, (b) temperature distribution in the device channel. 101

LIST OF TABLES

Table 1.1. Properties of GaN, SiC, Si, and GaAs. 5

LIST OF SYMBOLS

A	Area
$\mathbf{A}$	Coefficient matrix
B	Amplitude
$\mathbf{C}$	Boundary and flux vector
CV	Control Volume
C_{th}	Thermoreflectance coefficient
D_x	Volumetric heat generation length in x axis
D_y	Volumetric heat generation length in y axis
E	East central node in finite volume method (subscript *or* superscript)
E_C	Conduction band energy
E_V	Valance band energy
G_L	Lattice energy gain
H	Height
J_p	Hole current density
J_n	Electron current density
K_{ij}	Scattering matrix
L	Length
L_D	Drain length
L_{FP}	Fieldplate length
L_G	Gate length
L_{GD}	Gate-drain gap length
L_{GS}	Gate-source gap length
L_S	Source length
L_x	Domain length in x axis
L_y	Domain length in y axis
N	North central node in finite volume method (subscript *or* superscript)

N	Total number of nodes
N_A	Acceptor concentration
N_D	Ionized donor concentration
N_{atoms}	Number of atoms
P	Power
R	Reflectivity
$R_{net,n}$	Recombination rate for electrons
$R_{net,p}$	Recombination rate for holes
S	South central node in finite volume method (subscript *or* superscript)
$\vec{S}_L$	Lattice energy flux
$\vec{S}_n$	Electron energy flux
$\vec{S}_p$	Hole energy flux
$\vec{s}_i$	Unit vector in angular space
$\mathbf{T}$	Nodal temperature vector
T	Temperature
T_{diff}	Diffsuive temperature boundary
$(T_{max,BTE})_{HeatFlux}$	The maximum temperature calculated by BTE when the heat flux boundary is applied.
$(T_{max,BTE})_{HeatGeneration}$	The maximum temperature calculated by BTE when the volumetric heat generation is applied.
V_D	Drain voltage
V_G	Gate voltage
W	West central node in finite volume method (subscript *or* superscript)
W_L	Lattice energy density
W_n	Electron energy density
W_{n0}	Electron equilibrium energy density
W_p	Hole energy density
W_{p0}	Hole equilibrium energy density
a	Coefficients in finite volume method

a_i	Heat Flux boundary length
a_r	Aspect ratio
c	Specific heat capacity
d	Spatial resolution
$\mathbf{e}$	Nodal energy density vector
e	East boundary in finite volume method (subscript *or* superscript)
e	Phonon energy density
e^0	Phonon equilibrium density
f	Phonon distribution function
f_n^{td}	Thermal diffusion constant for electrons
f_p^{td}	Thermal diffusion constant for holes
g	Group (subscript)
$\dot{g}$	Volumetric heat generation
$\dot{g}'$	Volumetric heat generation for per unit depth
$\hbar$	Reduced Planck constant
i	Angular direction (subscript)
$\mathbf{k}$	Wavevector
k	Thermal conductivity
l	Quantum number
m	Mass
m_n	Effective mass of electrons
m_p	Effective mass of holes
n	Power constant
n	North boundary in finite volume method (subscript *or* superscript)
q	Electronic charge
$\vec{q}$	Heat flux
s	South boundary in finite volume method (subscript *or* superscript)
t	Time *or* thickness

t_{FP}	Fieldplate thickness
t_{pass}	Passivation thickness
u	Displacement
$\vec{v}$	Phonon group velocity
w	West boundary in finite volume method (subscript *or* superscript)
w_i	Weight constant for directions
x	x axis
y	y axis
z	z axis
ΔT	Temperature difference
ΔR	Reflectivity difference
Δ_x	Control volume length in x axis
Δ_y	Control volume length in y axis
$\hat{K}_n$	Electron thermal conductivity
$\hat{K}_p$	Hole thermal conductivity
$\hat{K}_L$	Lattice thermal conductivity
Λ	Mean free path
γ_i	y-axis component of the unit vector
δ_{ij}	Dirac delta function
ε	Emissivity
ζ	Spring constant
λ	Wavelength
λ_{Source}	Source wavelength
$\lambda_{Scattered}$	Scattered photon wavelength
μ_i	x-axis component of the unit vector
ξ_i	z-axis component of the unit vector
π	Pi number
ρ	Density
ρ_{trap}	Trap density
τ	Relaxation time

ω	Frequency
$\emptyset$	Electric potential
δa	Equilibrium position
$D(\omega)$	Phonon density of states

LIST OF ACRONYMS/ABBREVIATIONS

1-D	One-dimensional
2-D	Two-dimensional
2DEG	Two-dimensional electron gas
3-D	Three-dimensional
AlGaAs	Aluminium gallium arsenide
AlGaN	Aluminium gallium nitride
BOX	Burried oxide
BTE	Boltzmann transport equation
BTI	Bias temperature instability
CCD	Charge coupled device
CMOS	Complementary metal oxide semiconductor
Cu	Copper
DC	Direct current
DOM	Discrete ordinates method
FVDOM	Finite volume discrete ordinates method
FinFet	Fin field effect transistor
GTR	Gate resistance thermometry
GaAs	Gallium arsenide
GaN	Gallium nitride
Ge	Germanium
HEMT	High electron mobility transistor
HFET	Heterojunction field effect transistor
IR	Infrared
LA	Longitudinal acoustic
LBM	Lattice Boltzmann method
LDMOS	Laterally diffused metal oxide semiconductor
LED	Light emitting diode
LO	Longitudinal optical

LUS	Linear upwind scheme
MESFET	Metal semiconductor field effect transistor
MOSFET	Metal oxide field effect transistor
MTTF	Mean time to failure
NA	Numerical Aperture
PECVD	Plasma enhanced chemical vapor deposition
QUICK	Quadratic upstream interpolation for convective kinematics
RF	Radio frequency
SOI	Silicon on insulator
Si	Silicon
SiC	Silicon carbide
Si_3N_4	Silicon nitride
SiO_2	Silicon dioxide
TA	Transverse acoustic
TCAD	Technology computer aided design
TO	Transverse optical
TTI	Thermoreflectance thermal imaging
UV	Ultraviolet

1. INTRODUCTION

1.1. Semiconductor Materials

Solid materials can be classified into three different groups considering their electrical conductivity: Conductors, insulators, and semiconductors. Each material type has distinct electrical properties that stem from the atomic structure and these properties enable them to be utilized in different applications. Basically, the differentials are associated with the electronic energy bands or atomic energy levels.

Group of electronic energy levels that electrons are allowed to fill constitute electron energy bands and these band structures define electrical properties of a solid material [1]. A band can be occupied partially or fully (valance band) by electrons. Also, there are empty bands in materials, known as conduction bands. Between the filled and empty bands, electrons are not allowed to exist at certain states, these states form the band gap [1, 2] . The states of these bands in different materials are depicted in Figure 1.1. In solid materials, to induce an electric current, free electrons (electrons in the conduction band) are required. Free electrons are created by exciting charges from filled to empty states. This excitation energy depends on the band structure. In other words, if a band is partially occupied and there are empty states below band gap or filled and empty bands overlap, excitation over Fermi energy is observed at room

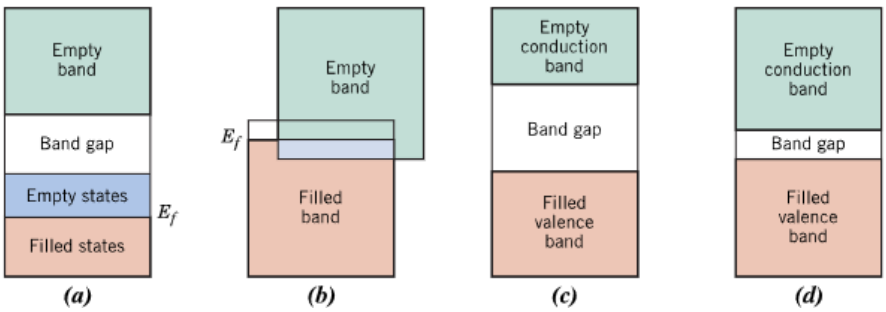


Figure 1.1. (a) and (b) represent partially filled states and overlapped bands such as in metals. Insulators and semiconductors are depicted by (c) and (d), respectively [2].

temperature. Otherwise, the given energy must be equal or surpass the value of band gap to move electrons to conduction band. Therefore, the band gap determines the electrical conductivity of materials since it defines the amount of energy necessary to make a material electrically conductive.

In metals with partially filled bands or overlapped band structures (Figure 1.1 (a) and (b)), electrons become free by relatively small energy, thus applying a small energy can contribute to large number of free electrons. This behavior can be explained by the free electron model [3] in which valance electrons within a metallic solid create an electron gas, and by applying a small electric field, current can be obtained. However, in insulators and semiconductors to excite electrons to conduction band, an amount of energy exceeding band gap is required, which distinguishes insulators and semiconductors from metals (Figure 1.1 (c) and (d)). Also, this energy can be in the form of heat, light, or electric field depending on the band gap and the temperature dependence. The difference between the insulators and the semiconductor solids relies on the amount of band gap energy [2]. The band gap of an insulator is bigger than a semiconductor material, thus much more energy is required for moving electrons from valance band to conduction band, consequently. For instance, Silicon dioxide (SiO_2) has a band gap of 9 eV at 300 K [4] and is operated as an electrical insulator in microelectronics. On the other hand, Silicon (Si), a well-known semiconductor, has 1.14 eV at 300 K [5] and facilitates many solid-state applications especially in microelectronics such as conventional transistors [6–8].

Some solid materials show semiconductor behavior without external augmentation, which are called intrinsic semiconductors, for instance, bulk silicon (Si) and germanium (Ge). Also, compounds such as gallium nitride (GaN) can be intrinsic semiconductor. Furthermore, a semiconductor solid can be acquired by adding impurities and changing electrical behavior of a host material inherently. These types of materials are called extrinsic semiconductors and the process is known as doping. Doping process depends on the impurity atom. By adding an impurity atom that has enough electrons at outer shell to remain relatively free after creating covalent bonds

with the host atom, electrons require a little excitation energy is required for electron movement. By this method, electron charge concentration can be increased by adding impurity atoms. These semiconductors are called n-type semiconductors and the impurity atom is known as donor [9]. Another extrinsic type of semiconductor is p-type semiconductor. As a result of the choice of impurity atoms, it has more positive charges, called holes, than electrons. Accordingly, by applying external energy, holes and electrons can change position, which facilitates charge movement. Yet, in p-type semiconductors electrical conductivity stems from holes instead of electrons, and positive charges are predominant [9]. By virtue of their properties, behavior of semiconductor materials can be manipulated in accordance with desired application. These versatile materials are harnessed for building solid-state devices which are used in many fields such as automotive, military, and space applications [10].

1.2. Semiconductor Devices

Contemporary microelectronics and information technology rely on semiconductor devices, for instance transistors are the integral part the today's technology. With the research on semiconductor physics, vacuum tubes in computers and radios were supplanted by silicon transistors for logic gates. The invention of transistors led to miniaturized electronic circuits and increased the computational power and speed significantly. Following the invention, the number of transistors within a silicon chip were about 30 in 1965 [11]. Along with the improvements such as the development of metal-oxide-field-effect transistor (MOSFET) and complementary metal-oxide-semiconductors (CMOS), this number increased dramatically and exceeded ten million in 2001 [12]. Today, besides silicon transistors, there are variety of transistor applications and the number of transistors in a chip exceeds billion [13], and the electronics industry depending on transistors worth of $4 trillion [14].

Transistors can be used as an electrical switch in an electrical circuit [8], or they can amplify signals in radio frequency (RF) amplifiers in high power applications [10] such as base stations (Figure 1.2 (a) [15]). In accordance with the implementation field,

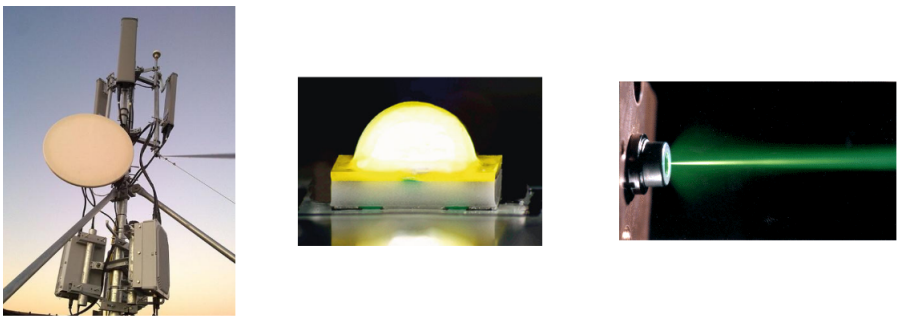


Figure 1.2. Semiconductor applications: (a) base station [15], (b) LED [17], (c) Quantum well laser [18].

there are distinctive types of transistor structures and materials. For instance, the most common transistor type is silicon metal-oxide-field-effect transistor (MOSFET) and is used in integrated circuits [16]. On the other hand, applications of semiconductors are not confined to transistors, they are widely utilized in light emitting diodes (LEDs) and lasers shown in Figure 1.2 (b) and (c) [17,18]. There are various LED applications, such as transportation lighting, general lighting, medical implementations and so on [17,19,20]. Also, lasers have similar structures with LEDs, yet, by virtue of their higher output power and speed compared the LEDs, these types of devices are used in many areas regarding sensors, microelectronics fabrication, and communication [16, 21].

Along with the advancements in fabrication techniques over the past 60 years, the number of transistors, especially MOSFETs, in an integrated circuit doubles in virtually 2 years, which results higher computational power and today's technological infrastructure. This trend was introduced by Gordon Moore in 1965, and it is acknowledged as Moore's law [22]. However, the trend has started to plateau as enhancements approach towards physical limits and fabrication methods become more expensive [11, 13, 14, 23]. Scaling down a transistor length towards atomic scale ($\sim$10 nm) impairs current control on device channel, for instance, required voltage for turning a transistor off rises exponentially with channel length [11]. Furthermore, at atomic scales quantum tunneling can be observed which could make a transistor uncontrollable.

To cope with these limitations and overcome the forecasted end of the Moore's law, devices with different structures and materials have been suggested. For instance, fin field-effect transistor (FinFet) has been developed which has three-dimensional gate working as multiple gates on transistor [24, 25]. Furthermore, in 2020, TSMC and Samsung announced the production of the smallest transistor, 5nm FinFet based on silicon, in an integrated circuit [13,26]. A different type of MOSFET structure, laterally diffused metal-oxide-semiconductor (LDMOS) has been operated for RF applications such as for mobile networks [27–29]. Metal-semiconductor field-effect transistor (MESFET) were also introduced for power electronics applications [30, 31]. Another device structure that draws attention is high electron mobility transistors (HEMTs) or heterojunction field effect transistors (HFET) [32]. In these types of devices, heterojunction structure along with semiconductor properties facilitates higher power and frequency applications [10, 33].

Beside device structure and layout, semiconductor material properties are also imperative for attaining better performance. To operate at more challenging conditions, conventional semiconductors, Si especially, are being supplanted by wide band gap semiconductor materials [10, 33]. These materials, such as GaN and SiC, have relatively higher band gap energies and their properties compared with conventional semiconductors are represented in the Table 1 [10, 34]. As a result of their high energy gap, wide bang gap materials such as GaN and SiC have higher breakdown voltages,

Table 1.1. Properties of GaN, SiC, Si, and GaAs [10,34].

Parameter	**GaN**	**SiC**	**Si**	**GaAs**
Electron mobility ($cm^2/V \cdot s$)	1800	900	1400	8500
Energy gap (eV)	3.5	3.26	1.12	1.1
Breakdown electric field (MV/cm)	3.3	3	0.3	0.4
Thermal conductivity ($W/cm \cdot K$)	1.3	4.9	1.5	0.5
Saturation drift velocity ($M \cdot cm/s$)	27	27	10	10

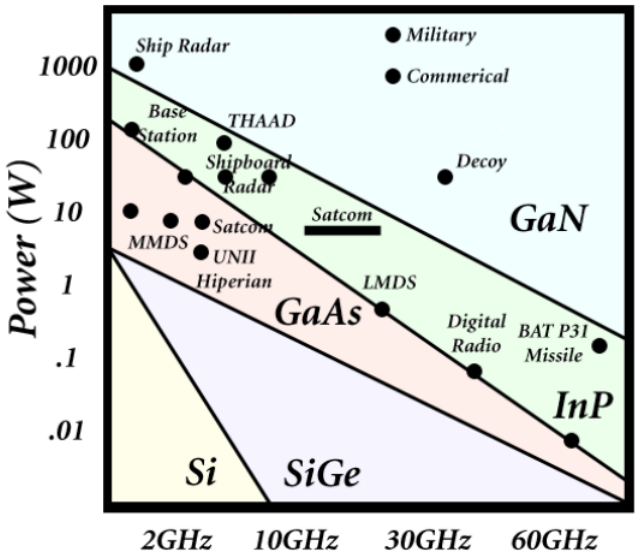


Figure 1.3. Operation fields of semiconductor materials [15].

therefore they can operate at higher temperatures and power conditions. Also, the high saturation velocity contributes to robustness at high frequency applications [10,33,34]. Their ability to facilitate high power, frequency applications in smaller dimensions, attracts attention. For instance, in terms of power density, frequency, and efficiency, AlGaN/GaN high electron mobility transistors (HEMTs) provide higher performance than Si counterparts [35,36]. Furthermore, maximum frequency of 400 GHz has been achieved with GaN HEMT [37]. Therefore, conventional GaAs HEMTs, LDMOSs, and Si MOSFETs have been overpowered by AlGaN/GaN HEMTs for high power applications in automotive, military, and space applications [34,38,39]. Operation fields of solid-state devices based on material are presented in Figure 1.3 [15]. It is seen that for many high power and frequency applications, wide band gap materials are needed.

1.3. Localized Self-Heating in Semiconductor Devices

The functionality of the semiconductor devices, transistors, LEDs, and lasers, rely upon the control of charge flow within the device layers. The electric current inside the device is regulated by the applied potential difference on the region in which charge movement occurs (i.e. channel). Depending on the applied electric field, electrons can gain high amount of kinetic energy, particularly in devices utilized in power electronics.

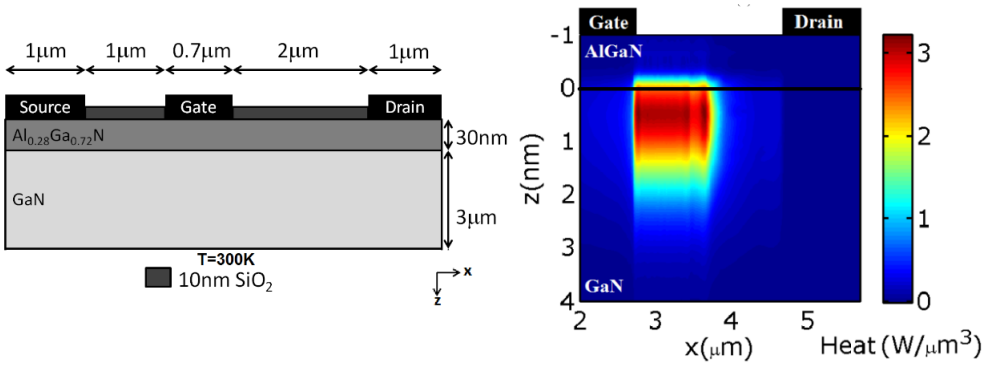


Figure 1.4. AlGaN/GaN HEMT (a) device structure, (b) Localized heat generation [40].

A moving electron within a medium may transfer its energy via scattering events with crystal defects, electrons, or lattice vibrations, which spawns self-heating phenomenon in such solid-state devices. Heat generation within a semiconductor, therefore, is result of the kinetic energy transfer from the electrons to lattice vibrations (i.e. Joule heating).

For instance, in AlGaN/GaN HEMTs, whose basic 2-D structure of is shown in Figure 1.4 (a) [40] electrons flow from the source part to drain part of the device around the AlGaN/GaN interface. In a normally-on device, applying a negative voltage between source and gate contacts confine the electron movement area in channel and create depletion region, which contributes to localized heat generation area, shown in Figure 1.4 (b). Reversely, applying a positive potential difference widen the Joule heating area [32]. Besides biasing conditions, device modifications for regulating nonuniform electric fields in active channel, such as field-plate structure and passivation layer, also have an influence on heat generation profile [32]. The confined localized heat generation, as small as 50 nm [41], near the drain side of the gate [32] can lead to hot-spot formation in which temperature is significantly higher than the rest of the device. Not only HFETs but also devices such as FinFets [42], laser and light emitting diodes [43, 44], and MOSFETs [45] can be subjected to the localized Joule heating. BOX (buried oxide) layer in a FinFET, which have low thermal conductivity, often contributes to confinement of already small, nanometer sized self-heating region illustrated in Figure 1.5 (a) [42]. As shown in Figure 1.5 (b) localized heat generation is

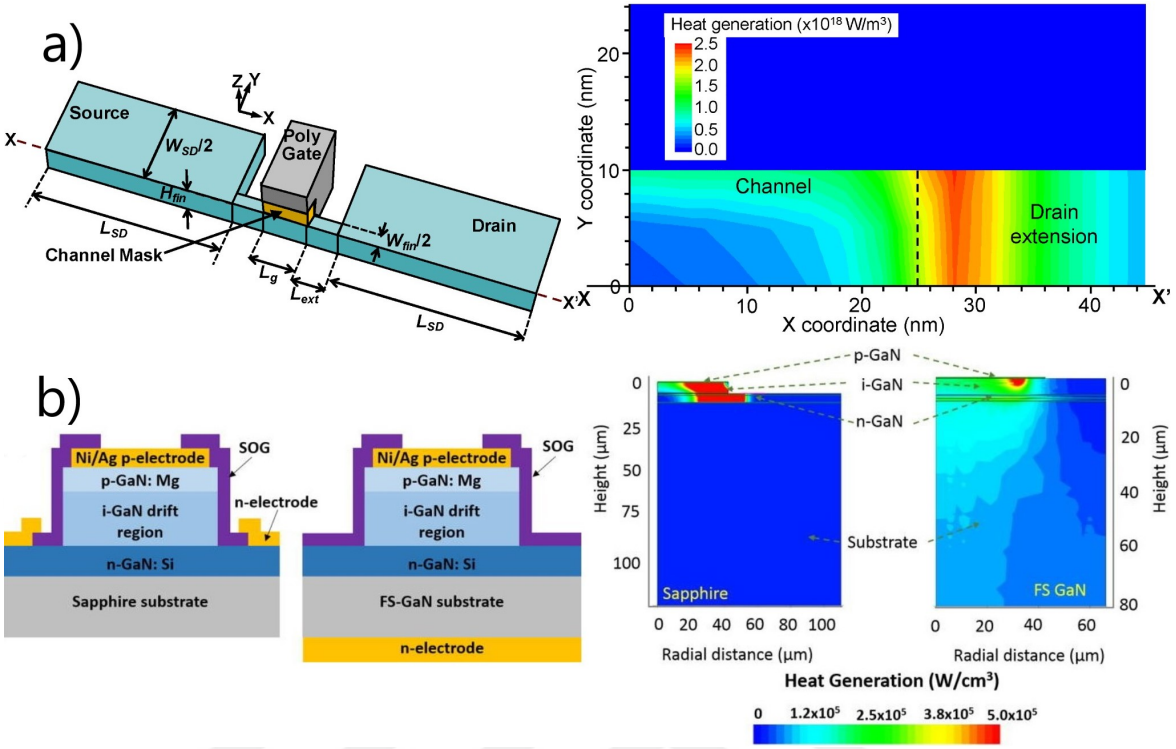


Figure 1.5. (a) FinFet and heat generation profile [42] and (b) quasi-vertical and vertical GaN diode [43].

also present near the junction of vertical or quasi-vertical GaN diodes [43]. Localized Joule heating in MOSFETs utilized in high power applications can be as small as 30 nm [45] and thermal problems are magnified by the passivation layer due to the low thermal conductivity of silicon dioxide.

Temperature rise stemming from the localized Joule heating affects charge concentration, mobility, and electrical conductivity inherently [46]. Thus, increased operating temperature impairs control of device behavior. Also, packing more devices in a smaller area leads to overheating and causes reliability issues [47, 48]. Mean-time-to-failure (MTTF) of devices, indicator of lifetime, is generally determined by conducting Arrhenius model which is a function of junction temperature of devices [49]. According to Arrhenius model, average lifetime descends exponentially with junction temperature rise which can be seen from Figure 1.6 [50].

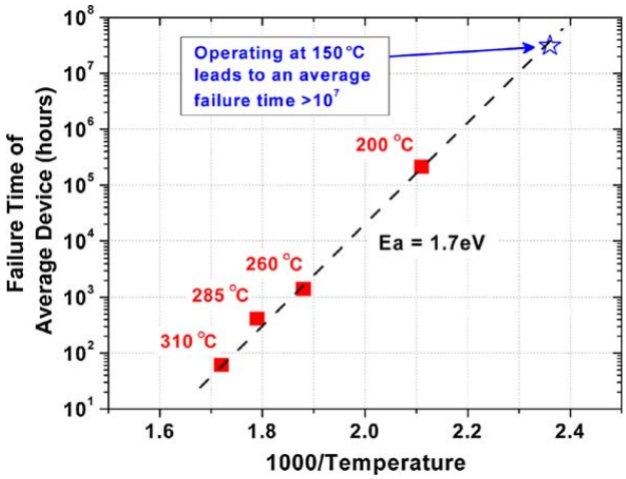


Figure 1.6. Arrhenius plot of GaN-on-Si transistor [50].

Together with the dissipation issues, self-heating can lead to device failure as it causes mechanical stress, undesirable chemical reactions, and altered electron transport [51]. As a result of thermal stress spawned by localized heat generation, lattice defects occur which obscure charge movement, and this degradation process is called bias temperature instability (BTI). BTI brings about the degradation of threshold voltage, thermoconductance, and drain current [52]. It is known that because of self-heating the drain current can drop by 15% in silicon on insulator (SOI) devices [53], which affects HFETs [54], FinFets, and MOSFETs. This phenomenon is called the current collapse. As a result of the degradation, devices operate with decreased microwave power and higher resistance. Moreover, particularly in high power LEDs and lasers, self-heating causes to total device failure, wavelength shift or the change of color that device emits [55]. The average lifetime of a LED chip also changes exponentially with the junction temperature. A study asserted that the increase of junction temperature by 10°C drops the average lifetime of a LED chip by 24,000 hours [56].

1.4. Thermal Characterization of Localized Heating

As the hot-spot temperature, due to localized self-heating, is the peak temperature values in devices, it is crucial to investigate localized heat generation profiles and thermal behavior of these devices. This can be done via various numerical models

and/or experiments depending on the desired accuracy and resolution.

1.4.1. Thermal Models and Size Effects

Although research on semiconductor devices have been done to understand the aspect of electronic performance mostly, thermal performance and analysis of devices also conducted for various cases. One common approach for assessing device temperature is conducting electro-thermal coupled simulations. With this approach, firstly, electrical simulation is performed for obtaining heat generation resulting from electron-lattice interplays, then temperature distribution is acquired by finite element analysis by Fourier's law of heat conduction. Heller et al. and Benbakhti et al. investigated self-heating and temperature effects on electrical behavior of AlGaN/GaN HEMTs by fully coupled electro-thermal analysis [57, 58]. Thermal stress in AlGaN/GaN HEMT caused by localized hot-spot was investigated by Venkatachalam et al. [41]. Pomeroy at al. showed the operation condition effects on average life time testing [59]. Besides lateral HEMT structures, temperature distribution in vertical and quasi-vertical power GaN transistors was assessed by Dallas et al. and Zhang et al. [43,60]. Also, reliability study of silicon FinFET device was done by coupled method [42]. Thermal analyses of both high power and silicon LEDs were conducted, yet it should be noted that in LED simulations, it is common that heat generation is introduced to models as a heat flux boundary [55, 61]. Such approximation is used for transistors modeling also [32, 51].

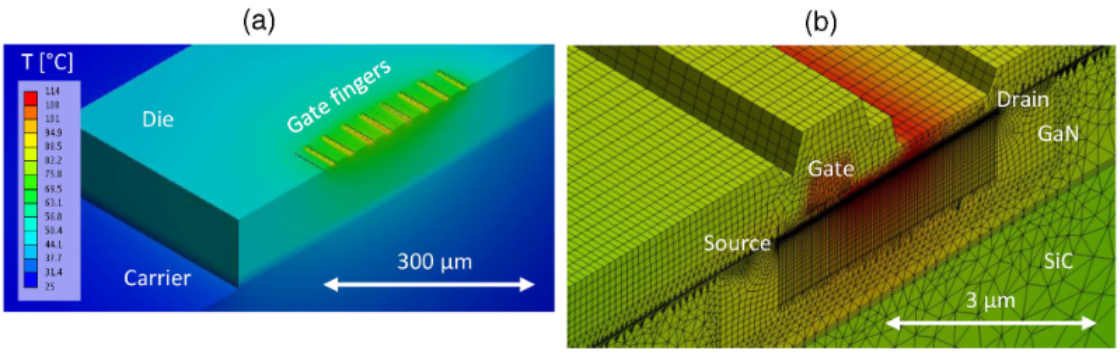


Figure 1.7. Thermal model for GaN HEMT: (a) Device and (b) mesh structure [59].

However, electro-thermal models using diffusive heat transfer assumption underestimate the peak temperature values in device channels owing to size effects which occurs when the lattice vibrations are obstructed by the small size of the heat generation region [40]. When this is the case, a closer look into microscopic heat transport mechanism in devices is necessary. Thus, phonon concept should be understood to build accurate thermal models in semiconductor devices with localized heat generation.

In crystal solids, a lattice is defined as periodical and identical atomic structures. In semiconductor and insulators materials lattice vibrations, systematic vibration of atoms in other words, are the main contributors of the heat transport contrary to metal solids in which electrons are responsible for transport. For instance, the amount of electron density (1023 cm^{-3}) in metal solids is significantly higher than the density within a typical semiconductor solid (<1018 cm^{-3}) [1]. As a result of this, heat transport in semiconductor solids are carried out predominantly by lattice vibrations. Nevertheless, the charge influence on heat transport is only important when the semiconductor is heavily doped. As atoms in a solid are attached to each other by repulsive and/or attractive forces, the vibration of any atom of the solid affects other atoms. This situation is often described by the mass spring system, similar to simplest 1-D monatomic lattice chain illustrated in Figure 1.8. From heat transport perspective, a part of the semiconductor solid having higher energy (for example higher temperature) has amplified atomic vibrations that propagate towards the areas having less energy (for example colder temperature). This describes the energy (heat) transport through atomic vibrations.

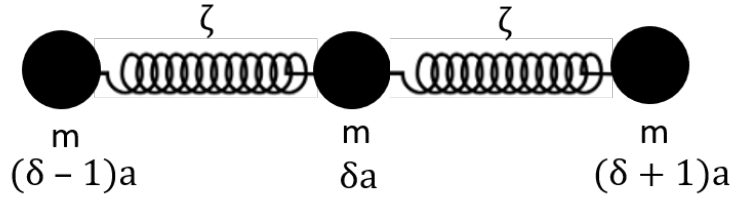


Figure 1.8. Monatomic lattice chain representation.

The quantum mechanical description of lattice waves is called phonons. Thus, phonon is a fictitious entity that defines quantized lattice waves. An atomic system explained by the mass-spring approximation in Figure 1.8 creates a phonon gas inside a solid that are responsible for heat transport by virtue of their scattering events with other phonons, electrons, or lattice impurities throughout solid medium. However, since phonon is a quantized system, they can only have discrete energy values which creates bands similar to the electronic bands. The allowable energy states of phonons in a semiconductor solid can be acquired by either solution of Schrödinger equation or wave equation. Below the classical approach is given:

$$m\frac{\partial^2 u}{\partial t^2} = \zeta a^2 \frac{\partial^2 u}{\partial x^2} \tag{1.1}$$

where u is the displacement of atoms, t is time, m is atomic mass, ζ is spring constant and a is the atomic position. And the solution for this type of wave equation is searched in the form of following [1]:

$$u_a = B\exp(-i(\omega t - \boldsymbol{k}\delta a)) \tag{1.2}$$

where $\boldsymbol{k}$ is wavevector, ω is frequency and δa is the equilibrium position, and B is the amplitude. Hence, solving the equation the frequency can be obtained as below:

$$\omega = 2(\zeta/m)^{1/2}|\sin ka/2| \tag{1.3}$$

and the wavevector from the boundary conditions can be written as below:

$$\boldsymbol{k} = 2\pi l/N_{atoms}a \quad l = 0, \pm 1, \pm 2, \ldots \tag{1.4}$$

where N is the number of atoms. It can be seen that only discrete number of frequencies, thus energy levels, exist for the monatomic chain and they are determined by the l. Although, this solution considers classical mechanic approach, solution of the Schrödinger equation also yields same frequency and wavevector relationship for this

1-D approximation.

The relationship between the wavevector and frequency is called phonon dispersion and it is used for representing the phonon behavior within a lattice. For a 3-D real crystal, there are 3 different quantum numbers (n, l, m), hence more wavevectors associated with these quantum numbers are exists. The 3-D solution of Schrödinger equation and obtaining dispersion relations for a semiconductor material are out of scope of this research, however, dispersion relation is important for understanding electron-phonon interactions. Considering the monatomic lattice chain, the phonon dispersion is plotted as Figure 1.9. The figure depicts the phonon frequency and wavevector relation which shows the energy change of a lattice vibration through the position of the phonon since the wavevector includes position information. Also, the phonon speed which is called group velocity can also be calculated from the slope for a give phonon group. The phonon energy and the group speed are decisive for modeling the heat transport as the relaxation processes, for instance the propagation distance before scattering events, rely upon these features.

The distance that a phonon travels along before any scattering events is called phonon mean free path (Λ) which is integral definition for heat transport within crys-

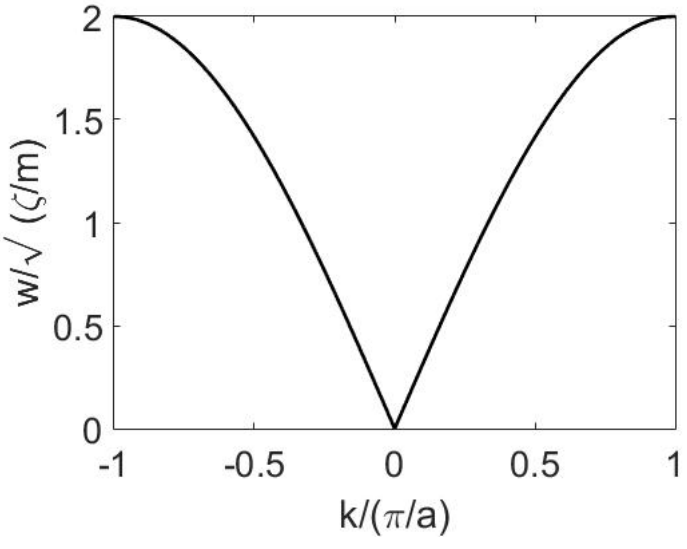


Figure 1.9. Dispersion for the monatomic lattice chain.

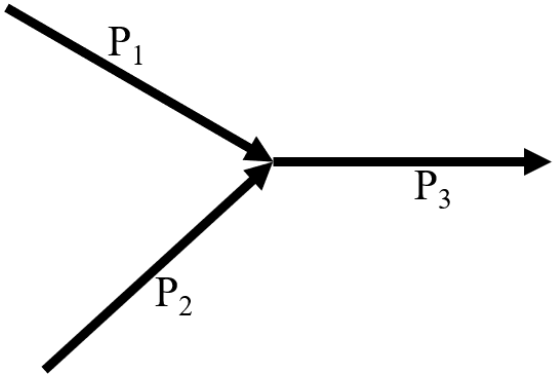


Figure 1.10. Phonon-phonon scattering (P_1, P_2 and P_3 refer to different phonons.).

tal solids. As shown in Figure 1.10, phonons travel a distance before scattering and forming new phonon. The size of heat generation area can affect phonon propagation if it is as small as phonon scattering distance [62]. When the heat generation size or characteristic size of a domain, that hosts localized heat generation, is comparable with the phonon mean free path of phonons, relaxation process is affected undesirably. If the size of the heat generation area comparable with the phonon mean free path, phonons propagating in heat generation region cannot relax their energy effectively since such phonons interact with high energy phonons within the medium before complete their mean free path distance. These size effects lead to sub-continuum heat transport and cannot be captured by diffusive continuum assumption by conducting Fourier's law of heat conduction formulation since it does not incorporate phonon interaction information [62].

The mean free path of the phonons in silicon varies from 30 nm to 300 nm [63], and it has been reported that phonons which are responsible for heat transport in GaN solid propagate ∼400 nm before scattering events [64,65]. These mean free path values are enough for inducing sub-continuum heat transport in silicon and GaN devices as heat generation area sizes can be on the order of few nanometers depending on the biasing condition [32]. In order to account for size effects, electro-thermal models need auxiliary description for phonon transport such as atomistic Green's function, molecular dynamics, and Boltzmann transport equation (BTE) [54].

Phonon effects in Si MOSFETs have been investigated widely; the influence of different silicon phonon bands on heat transport were reported by including electronic nature of device [45]. Also, Si MOSFET operation on temperature was investigated by electro-thermal model coupled with BTE equation [66]. A fully coupled electro-thermal model including phonon transport was conducted for understanding size effects and biasing conditions in AlGaN/GaN HEMT [67]. Accuracy of solution methods for phonon transport in GaN medium regarding lattice Boltzmann (LBM) method and discrete ordinates method (DOM) was investigated [68]. Figure 1.11 shows that in a GaN power transistor, solution of the diffusive heat transfer assumption underestimates the temperature rise in the device channel compared the phonon BTE equation solution based on DOM. Finally, influence of mean free path of GaN phonons on the hot-spot temperature of HFETs was shown by accounting for whole HEMT package [40].

Certain assumptions and simplifications are used for device thermal analysis. For instance, applying a uniform heat generation near an adiabatic boundary is a common approach to approximate device operations since heat transport predominantly occurs through heat generation area near a boundary, to the substrate and heat sink [63, 69]. For example, comparison of phonon models in SOI was demonstrated by using a single heat generation profile near adiabatic boundary [62, 70]. Along with a single heat

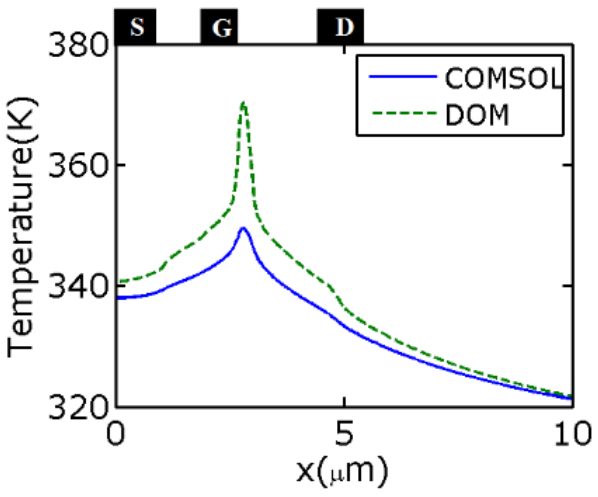


Figure 1.11. Diffusive (COMSOL) and sub-continuum (DOM) solution difference in the device channel [40].

generation profile, partially heated upper boundary with a constant temperature is a common approach for understanding phonon transport [63, 71]. Also, in these sub-continuum models, size effects are generally attributed to lateral length of heat generation area compared to phonon mean free path. However, device operation conditions, geometrical augmentations, or biasing effects changes the heat generation distribution vertically, horizontally or they can change generation area size. Thus, representing a device with a single uniform Joule heating profile and considering only lateral length could lead to errors, yet the Joule heating profile effects on sub-continuum thermal models are missing in the literature. Furthermore, the use of heat flux boundary approximation in LED and transistor finite element research [32,55], was not investigated by sub-continuum methods. For certain heat generation profiles with low errors this approximation can alleviate substantial computational power, which will be demonstrated with phonon transport. Therefore, localized Joule heating profile effects and heat flux boundary simplification should be assessed for more accurate thermal models.

1.4.2. Experiments

Experimental methods used for device temperature characterization are classified into three sections: Electrical, physical, and optical [72]. With physical methods temperature measurements are carried out by assessing heat transfer from device to a thermometer. These methods need contact with the probe region and thus can alter the device operation temperature [72]. To overcome this liquid crystal thermometry, a physical method, is suggested for the temperature detection in power transistors [73]. The functionality of the electrical methods is based on the premise that electrical behavior of devices relies upon temperature, therefore device temperature can be obtained by examining the electrical properties of devices. Gate resistance thermometry (GTR), which inspect change of resistance as a function of temperature, is used for GaN transistor temperature detection [74]. Assessment of the radiation features pertinent to probed semiconductor medium constitutes optical methods. Optical methods are non-contact and can provide temperature map of a device with relatively higher spatial resolution. Thus, they are widely used for temperature characterization in semiconductor

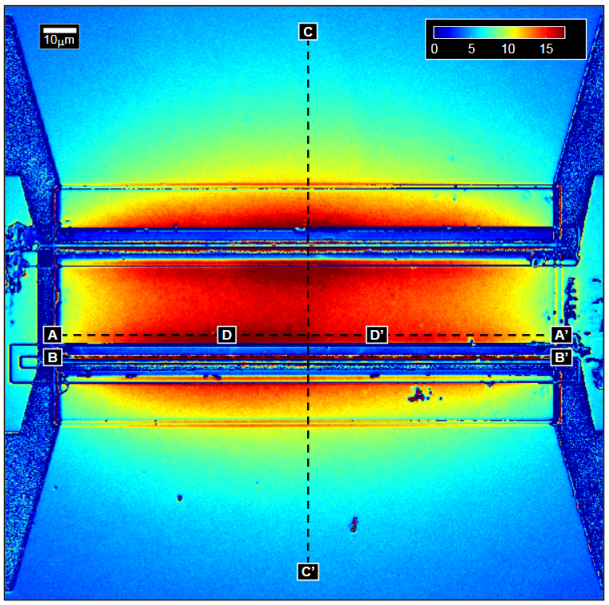


Figure 1.12. Thermoreflectance thermal imaging of GaN HEMT [82].

devices. For instance, the investigation of channel temperature of AlGaN/GaN transistors were done by infrared emission (IR) [75], thermoreflectance imaging (TTI) [76], photoluminescence [77], and Raman thermometry [78], which are all optical methods. Raman thermometry and thermoreflectance imaging were also used for thermal characterization of silicon MOSFETs [79,80]. Moreover, researchers tried to determine the junction temperature of LEDs by Raman thermometry and TTI [81]. However, each experimental method has different implementation area and spatial resolution. For instance, temperature map of a device surface can be obtained by infrared thermography, but its resolution is ∼4-5 µm [72], and for devices having nanometer scale buried active channels, obtaining only the surface temperature profile with low resolution is a drawback. With micro-Raman method depending on the wavelength of the photon beam, temperature values can be acquired from the inner layers with higher spatial resolution of ∼1 µm [78]. On the other hand, recently higher sub-micron resolution was achieved by the thermoreflectance imaging [82], shown in Figure 1.12, yet this method also provides surface temperatures only. Therefore, the experimental characterization of the hot-spot temperatures can be difficult and less accurate due to their resolutions and limitations considering the buried location of the hot-spot, caused by stacked nature of the semiconductor devices. Thermal models are required for understanding

actual temperature values in such devices.

Although the micro-Raman and TTI are commonly used for device thermal characterization, their accuracy was not investigated considering size-effects. The validation of these methods were conducted by electro-thermal methods [73, 83] that do not account for phonon transport which could lead significant errors. Thus, accuracy of these two methods should be investigated considering sub-continuum thermal transport.

1.5. Motivation

The peak temperature values of semiconductor devices are responsible for thermal degradation mechanisms that affect overall device performance and reliability. Localized self-heating is responsible for high peak temperatures and size effects. Many researchers focused on understanding impacts of thermal behavior of devices on performance or reliability. Some studies did not incorporate the size effects and phonon transport in their solutions and thus underestimated the temperature values. On the other hand, there are studies investigating the phonon transport in semiconductor devices such as silicon transistors and AlGaN/GaN HEMTs. However, detailed analysis of the effects of localized heat generation region's size, shape, and location has not been investigated previously. The effects of Joule heating profile will be investigated in this work for a semiconductor medium by accounting for size effects and phonon transport with Boltzmann Transport Equation. Also, validity of implementation of heat generation profile as a heat flux with Boltzmann transport equation will be analyzed. Moreover, by using the multiscale electro-thermal model which accounts for the sub-continuum effects, the preciseness of the micro-Raman and thermoreflectance imaging (TTI) methods has been investigated numerically for an AlGaN/GaN HEMT having different geometrical properties and operation conditions. Finally, as a result of the collaborative research, a novel experimental technique called "UV thermoreflectance imaging" has been suggested and the ballistic thermal transport method conducted for comparison.

1.6. Outline of Thesis

The work in this thesis is explained in 5 chapters. In Chapter 2, details of the continuum scale and phonon BTE based numerical models built to understand the Joule heating profile effects on hot-spot temperature are given. Phonon BTE is solved using gray phonon and relaxation time and Joule heating is applied both as heat flux and heat generation to investigate the effects of heat generation and heat flux boundary conditions on nanoscale heat transfer.

In Chapter 3, a real device, AlGaN/GaN HEMT, is modeled with coupled electro-thermal models to understand the effect of biasing conditions on Joule heating profiles and nanoscale heat transfer. Hydrodynamic transport model is employed for the electrical simulations carried at two different biasing conditions for devices with different geometrical properties (field plated and without field plated device). Both continuum and sub-continuum approaches presented in Chapter 2 are used to investigate the nanoscale thermal effects in electrically modeled devices.

In Chapter 4, the accuracy and success of the experimental micro-Raman and thermoreflectance imaging methods regarding the peak temperature detection is investigated using an electro-thermal numerical model similar to one introduced in Chapter 3. To do this, in the virtual experiment subsection, fictitious experimental probe regions are created for the AlGaN/GaN HEMT model used in Chapter 3. Temperature predictions of the virtual experiments are obtained with both continuum and sub-continuum approaches and the results are compared. Lastly, in the actual experiment subsection, a geometrically different AlGaN/GaN HEMT structure operated at different biasing conditions is modeled and measured by TTI and UV TTI approach

Finally, in Chapter 5, findings in this thesis are summarized and discussed. Accordingly, future research areas are suggested.

2. SIZE EFFECTS CAUSED BY JOULE HEATING

The nanometer scale Joule heating profiles cause size effects in devices, which lead to peak temperature values that cannot be captured by diffusive approaches. Also, device operation conditions such as biasing conditions or device architecture can affect the heat generation profile by changing the horizontal and vertical length of the confined generation region.

In GaN HEMTs or vertical structured transistors, modeling Joule heating near an adiabatic boundary is a common approach since majority of the heat is carried in the opposite direction of this boundary [15, 70, 84]. Moreover, in some cases this heat generation happens in such a thin region that heat generation can be modeled as heat flux [51, 54]. Heat flux simplification is often used in continuum models with reasonable accuracy, yet its accuracy is not tested in sub-continuum approaches. Thus, to understand the heat generation profile effects on the thermal size effects and thus the maximum temperature in a semiconductor material, GaN domain with distinct Joule

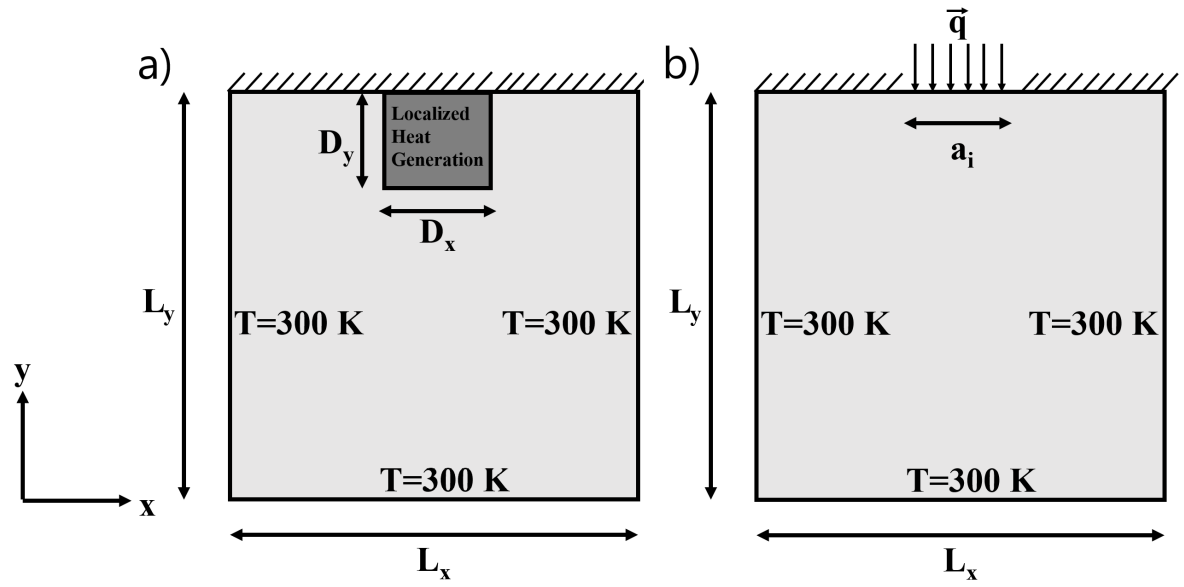


Figure 2.1. The investigated domain with (a) volumetric heat generation and (b) heat flux boundary.

heating profiles is modeled using both continuum and sub-continuum approaches. Heat generation areas with different aspect ratios, sizes, and power densities are introduced into the 2-D domain near an adiabatic boundary and the heat flux simplification is also investigated.

The investigated domain for the volumetric heat generation and the heat flux implementation is shown in Figure 2.1. The vertical and horizontal lengths of the domain are set constant with L_x=L_y = 4 µm. For the volumetric heat generation calculations (Figure 2.1(a)), the upper boundary is set to adiabatic and the rest has prescribed temperature of T=300 K. In the same model, the sizes of the heat generation areas are defined as D_x and D_y. The area sizes of heat generation region (D_x x D_y) vary from 0.004 µm^2 to 0.1 µm^2 by increment of 0.02 µm^2 The aspect ratio of the generation area is defined with a_r =D_x/D_y and is is shifted from 1/32 to 32 linearly. For the heat flux simplification (Figure 2.1(b)), the heat flux values ($\vec{q}$) are generated from the heat generation profiles used in the previous case. To do this, each heat generation area is integrated along y-axis, hence the heat flux values are acquired as a function of x. Figure 2.2 illustrates how the volumetric heat generation data in Figure 2.2(a) is converted to heat flux in Figure 2.2(b). The horizontal length of the upper wall subjected to the heat flux condition is defined with a_i=D_x and the rest of this boundary is set adiabatic. The other boundaries are prescribed temperature as in volumetric heat generation case. Three different uniform volumetric heat generation

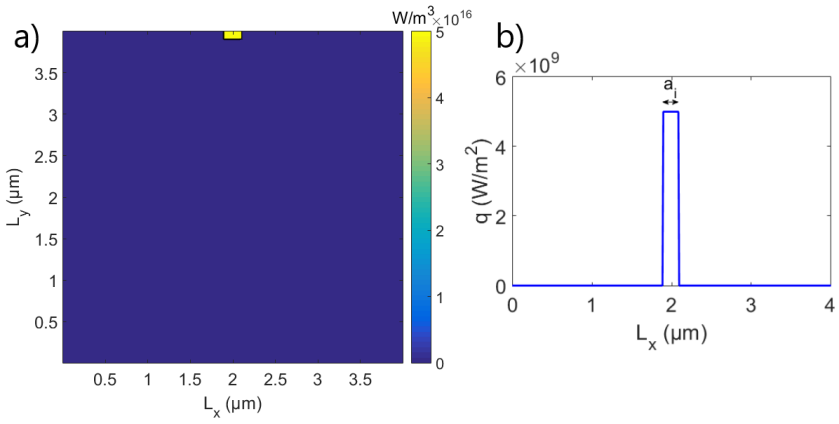


Figure 2.2. Transition from (a) heat generation to (b) heat flux.

values for per unit depth are defined, which are P = 1 W/mm, P = 3 W/mm, and P = 10 W/mm. It should be noted that these volumetric heat values can also be interpreted as solid-state device operating conditions.

The details of the continuum and sub-continuum thermal models used for determining size effects in these domains are given next.

2.1. Continuum Model

Although continuum scale solution cannot capture phonon events and size effects in the domain, it is solved before the sub-continuum model for comparison purpose and to provide initial values for the sub-continuum model, which uses an iterative approach.

Continuum scale approach assumes diffusive heat transport in a medium because of temperature gradient. Therefore, to calculate heat conduction, Fourier's law of heat conduction is solved numerically, which states that heat flux is proportional to the negative temperature gradient. It is written as:

$$\vec{q} = -k.\nabla T \left(\mathrm{W/m^2}\right) \tag{2.1}$$

where $\vec{q}$ is heat flux vector, k is bulk thermal conductivity of material and T is the temperature.

Regarding Equation 2.1, general heat equation for a domain can be written in terms of the balance between the heat fluxes entering and leaving the domain. Thus, governing equation for diffusive domain can be obtained as:

$$\rho c \frac{\partial T}{\partial t} = \dot{g} + \nabla \cdot (k \nabla T) \left(\mathrm{W/m^3}\right) \tag{2.2}$$

in which c is bulk specific heat as the medium is an incompressible solid. ρ is density and $\dot{g}$ stands for volumetric heat generation within the domain.

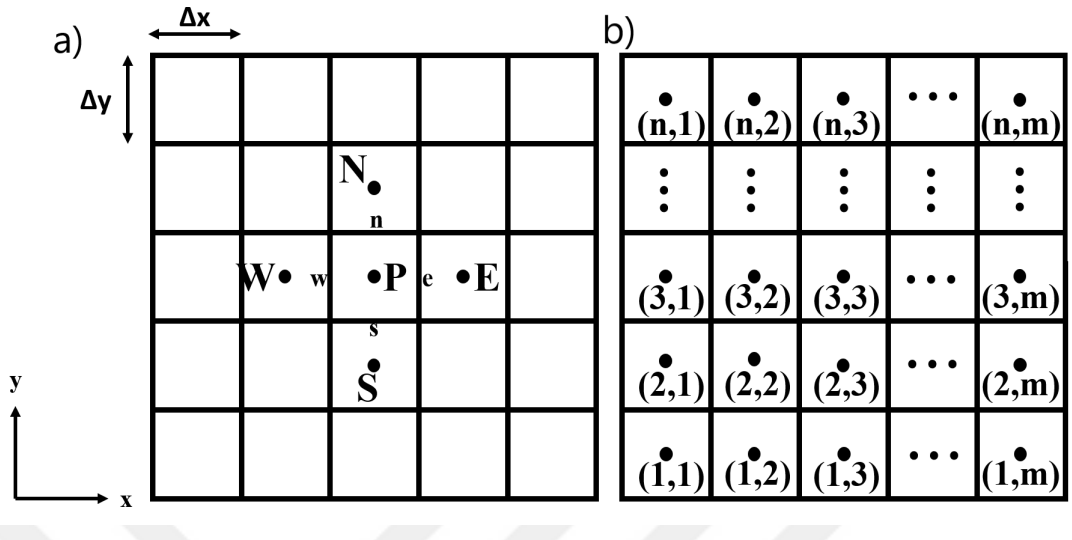


Figure 2.3. (a) Spatial discretization according to finite volume method, (b) nodes depending on grid number.

The steady state form of Equation 2.2 is solved by finite volume method in 2-D cartesian coordinates. In this method, temperature values of a node within the discretized volume is calculated. Information required for determining a temperature at the central node is obtained by boundaries of the volume. Therefore, to solve it, spatial discretization of the equation is needed for the 2-D domain represented in Figure 2.3.

Discretization in the finite volume method starts with integrating governing equation over the control volume as:

$$\int_{CV} \nabla \cdot \left(k \frac{\partial T}{\partial x} \right) dV + \int_{CV} \nabla \cdot \left(k \frac{\partial T}{\partial y} \right) dV + \int_{CV} \dot{g} dV = 0 \tag{2.3}$$

After that, for representing the equation in terms of boundary fluxes, Equation 2.3 can be transformed by using the divergence theorem:

$$\int_{A} \vec{n} \cdot \left(k \frac{\partial T}{\partial x} \right) dA + \int_{A} \vec{n} \cdot \left(k \frac{\partial T}{\partial y} \right) dA + \dot{g}' \Delta_x \Delta_y = 0 \tag{2.4}$$

where $\dot{g}'$ is heat generation for per unit depth. Also, integration parts of Equation 2.4

define the flux balance entering and leaving the control volume at both vertical and horizontal directions, thus, these integrals can be approximated as in Equation 2.5:

$$\left(k_w A_w \frac{\partial T_w}{\partial x}\right) - \left(k_e A_e \frac{\partial T_e}{\partial x}\right) + \left(k_s A_s \frac{\partial T_s}{\partial y}\right) - \left(k_n A_n \frac{\partial T_n}{\partial y}\right) + \dot{g}' \Delta_x \Delta_y = 0 \qquad (2.5)$$

In Equation 2.5, subscripts with lowercase w, e, s, and n indicate the information at the west, east, south, and north face of the control volume, respectively. To construct coefficient matrix, these face properties should be written in terms of the temperature at the central node of the neighbor volumes. This can be done by different discretization schemes that influence accuracy, yet central differencing scheme is used for diffusive calculations in this thesis since it provides adequate accuracy for diffusive heat transport. Also, the other schemes will be discussed in BTE discretization. By using central differencing scheme and assuming that thermal conductivity is not changed with position in the 2-D domain (k_w=k_e=k_s=k_n), derivatives at the control volume boundaries can be written as:

$$\frac{dT_w}{\partial x} = \frac{T_W - T_p}{\Delta_x} \qquad (2.6)$$

$$\frac{\partial T_e}{\partial x} = \frac{T_P - T_E}{\Delta_x} \qquad (2.7)$$

$$\frac{\partial T_s}{\partial y} = \frac{T_S - T_p}{\Delta_y} \qquad (2.8)$$

$$\frac{\partial T_n}{\partial y} = \frac{T_p - T_N}{\Delta_y} \qquad (2.9)$$

Finally, by substituting these terms into Equation 2.5, governing equation for interior nodes can be written as:

$$a_p T_p = a_W T_w + a_E T_E + a_s T_s + a_N T_N + \frac{\dot{g}' \Delta_x \Delta_y}{k} \tag{2.10}$$

where a_P, a_W, a_E, a_S, and a_N are coefficients given in the form of:

$$a_p = 2\left(\frac{\Delta_y}{\Delta_x} + \frac{\Delta_x}{\Delta_y}\right) \tag{2.11}$$

$$a_W = a_E = \frac{\Delta_y}{\Delta_x} \tag{2.12}$$

$$a_S = a_N = \frac{\Delta_x}{\Delta_y} \tag{2.13}$$

However, this form of the governing equation is only applicable for interior nodes in the domain, thus for the prescribed temperature, adiabatic, and prescribed heat flux conditions, discretized form of the boundary nodes should account for these conditions:

$$T_{\text{surface}} = T_{\text{prescribed}} \tag{2.14}$$

$$\left(\frac{\partial T}{\partial n}\right)_{\text{Surface}} = 0 \tag{2.15}$$

$$k\left(\frac{\partial T}{\partial n}\right)_{\text{surface}} = -\vec{q} \tag{2.16}$$

As a result of the discretization, depending on the number of nodes in the x and y directions, total N number of nodes and algebraic equations are obtained as illustrated in Figure 2.3 (b). These set of equations are written in the matrix form:

$$\begin{bmatrix} a_{11} & a_{12} & a_{13} & \dots & a_{1N} \\ a_{21} & a_{22} & a_{23} & \dots & a_{2N} \\ a_{31} & a_{32} & a_{33} & \dots & a_{3N} \\ \vdots & \vdots & \vdots & \vdots & \vdots \\ a_{N1} & a_{N2} & a_{N3} & \dots & a_{NN} \end{bmatrix} \begin{bmatrix} T_1 \\ T_2 \\ T_3 \\ \vdots \\ T_N \end{bmatrix} = \begin{bmatrix} C_1 \\ C_2 \\ C_3 \\ \vdots \\ C_N \end{bmatrix} \tag{2.17}$$

The matrix composed of the coefficients, a_{mn}, is called the coefficients matrix and is denoted by $\mathbf{A}$. $\mathbf{T}$ is a vector of nodal temperature values within the control volume, and $\mathbf{C}$ vector is generated from the heat generation and/or boundary flux terms. Consequently, in continuum model nodal temperatures can be obtained as below:

$$\mathbf{T} = \mathbf{A}^{-1}\mathbf{C} \tag{2.18}$$

The matrix system shown in Equation 2.18 is solved by MATLAB easily since it is a linear system of equations.

2.2. Sub-continuum Model

To account for the size effects and phonon propagation in the 2-D domain depicted in Figure 2.1, a model for phonon transport is needed. There are different ways to model phonon transport, and each has unique advantages and drawbacks. Three of which are molecular dynamics, atomistic Green's function, and BTE [63, 85, 86]. Phonon transport with molecular dynamics approach is carried out by taking movement of atoms or molecules into account in the given domain. This is done by incorporating interatomic potentials into Newton's equation of motion. Although this model yields accurate information for a given domain, applying it over a domain larger than the

atomic scale increases computational cost substantially.

Another way of calculating phonon transport is using Green's function. Although it has been used for electron transport initially, it can be used for phonon transport in atomic scale. It is generally used for relatively small systems, therefore, computational cost is a problem in domains bigger than the atomic scale.

BTE is solved for domains larger than the atomic scales. Therefore, in this thesis so as to account for phonon effects, phonon BTE is solved.The variation of the statistical distribution of phonons are expressed in Phonon BTE as in Equation 2.19:

$$\frac{\partial f}{\partial t} + \vec{v} \cdot \nabla f = \left(\frac{\partial f}{\partial t}\right)_{scatt} \tag{2.19}$$

where f represents the phonon distribution function which includes phonon properties of position, direction, frequency, and polarization. Phonon distribution function (f) is altered in the domain in the wake of the scattering events such as phonon-phonon and electron-phonon interactions. The phonon distribution is also influenced by the scattering events among phonons and boundaries and lattice impurities. Therefore, these interplays are incorporated into calculations by the term at the right-hand side of Equation 2.19. Also, $\vec{v}$ indicates the speed of phonon modes in material which is called phonon group velocity. Phonon group velocity can be calculated for each phonon mode considering the gradient of dispersion curve, as in Equation 2.20, where ω stands for the frequency, and $\boldsymbol{k}$ is the wavevector.

$$\vec{v} = \frac{\partial \omega}{\partial \boldsymbol{k}} \tag{2.20}$$

Therefore, to solve phonon BTE, these properties of the phonons in a solid medium are needed. In real crystals, phonon dispersion is different than the monatomic lattice presented by Figure 2.4. For example, dispersion relation of GaN (Gallium Nitride), a wide band semiconductor having wurtzite structure, can be seen from the

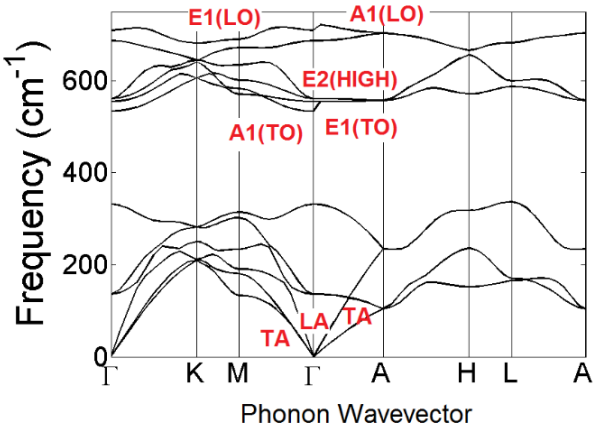


Figure 2.4. Phonon dispersion curve of GaN [54].

Figure 2.4 [54]. This figure depicts the relation between the phonon frequencies and wavevectors in GaN medium (for x axis in this figure). It can be seen that only discrete phonon frequencies are allowed along the x-axis direction of the wavevectors as phonons are defined as quantized lattice vibrations. There are 12 number of phonon modes in GaN crystal. These modes can be separated into two main branches regarding their magnitude of frequency. Phonon modes having lower frequency are called acoustic phonons. Moreover, acoustic phonons have zero frequency at the zone center in where wavevector also zero. The phonon modes with higher frequency levels are called optical phonons. Figure 2.4 depicts: 3 acoustic and 9 optical phonon modes out of 12 modes in GaN crystal. The waves are also grouped in accordance with their relationship between the vibration direction and the wave propagation direction. If the direction of the vibration and the propagation direction are perpendicular, then the wave is called transverse wave. Besides, when the direction of the vibration and the wave propagation direction are parallel, the wave is acknowledged as longitudinal wave. In Figure 2.4, one of the acoustic phonon modes is transverse (TA) and the rest of the acoustic modes are longitudinal (LA). On the other hand, 6 out of 9 optical phonons show transverse behavior and the rest of the optical phonons are longitudinal which are named as TO and LO, respectively.

Solving BTE in Equation 2.19 for all phonons in the crystal is not easy since the phonon distribution function needs variables such as position, direction, frequency,

and polarization for the all phonons. Hence, approximations can be used to ease this computational effort. Approximated models can be divided into two sub-groups: Gray models and non-gray models.

Non-gray models consist of two different approaches that are called two-fluid model and full dispersion model. In the two-fluid model, two types of phonons are defined in the domain which are either responsible for heat transport or act as a reservoir. However, it has been reported that two-fluid model overestimates the peak temperature value in the domain [62]. Unlike the two-fluid model, the full dispersion model accounts for all phonon modes in the crystal, and it is the most comprehensive model. In this model, contribution to heat transport from all phonon modes are calculated. However, in this thesis gray model, that considers only single phonon group, is used for the sub-continuum approach.

2.2.1. Gray Model and Relaxation Time Approximation

As shown in Figure 2.4, there are different phonon modes and group velocities corresponding to these phonon modes. Notwithstanding, the gray approach is based on the premise that there are only one phonon group and one group velocity correspondingly. Although full dispersion method is more accurate, the discrepancy between single phonon mode approximation is small for GaN [87]. This stems from the substantially fast relaxation of optical phonons [88, 89] to acoustic phonons in GaN, which enables to neglect interplays between optical and acoustic phonons. However, for materials in which impacts of different phonon modes are predominant, full dispersion models should be used.

In this study phonon BTE is solved with the gray model and relaxation time approximations. To simplify Equation 2.19 in gray model, firstly, phonon distribution function is written in terms of an integrated energy density as:

$$e(T) = f\hbar w D(w) \tag{2.21}$$

where e is energy density, f is phonon distribution function, $\hbar$ is reduced Planck's constant, w is frequency, and $D(w)$ is phonon density of states. Thus, using integrated energy density instead of a phonon distribution function, the energy density form is derived [86]:

$$\frac{\partial e}{\partial t} + \vec{v} \cdot \nabla e = \left(\frac{\partial e}{\partial t}\right)_{\text{scatt}} \tag{2.22}$$

In this form of phonon BTE, wavevector and polarization of phonons are omitted as integrated energy density is function of direction and position of a phonon only. Also, to represent phonon scattering events the relaxation time approximation is used. With this approach, equilibrium energy density of lattice and phonon energy densities are defined separately. Due to the scattering events, the energy densities of phonons change and attain an equilibrium state which is the equilibrium energy density of lattice. This relaxation process takes place a certain amount of time which is defined by the *relaxation time*. In accordance with the relaxation time approach, Equation 2.22 can be rewritten as below:

$$\frac{\partial e}{\partial t} + \vec{v} \cdot \nabla e = \frac{e_0 - e}{\tau} + \dot{g} \tag{2.23}$$

where e is phonon energy density, and e_0 is equilibrium energy density. The volumetric heat is incorporated into equation by $\dot{g}$. Also, $\vec{v}$ represents phonon group velocity, however, it should be noted that since it is gray approximation, $\vec{v}$ stands for only one group of phonons. The relaxation time is indicated by τ. Equation 2.23 is the final form of the gray model and relaxation time approximation for calculating phonon transport. After finding each equilibrium density in lattice, corresponding lattice temperature is found by Equation 2.24:

$$e_0 = cT \tag{2.24}$$

where c is bulk specific heat, and T is the lattice temperature.

Phonon properties and bulk material properties can be related by using kinetic theory which is written as:

$$k_{bulk} = \frac{1}{3} c \vec{v}^2 \tau \tag{2.25}$$

in which k_{bulk} represents bulk thermal conductivity of material. Finally, phonon mean free path, relaxation time, and group velocity can be related as in Equation 2.26:

$$\Lambda = \vec{v}\tau \tag{2.26}$$

To solve gray phonon BTE, two different procedures can be followed in order to determine single phonon group properties. These approaches diverge regarding calculation of *mean free path*, *relaxation time*, and *phonon group velocity*. In the first approach the *phonon mean free path* is defined in accordance with the thermal conductivity accumulation results [90]. After that, *phonon group velocity* and *relaxation time* values are calculated based on Equations 2.25 and 2.26 . In the second approach, instead of mean free path of phonons, *phonon group velocity* is defined. For this approach, the averaged group velocity of acoustic phonons in the Brillouin zone is selected since acoustic phonons contributes heat transport mostly in the lattice. After that similar to the first approach, *mean free path* and *relaxation time* values are acquired from Equations 2.25 and 2.26. In this chapter, the first approach is used by setting the *phono mean free path* of the GaN to 400 nm since it has been shown that phonons with *mean free path* of ∼400 nm or higher participate heat transport predominantly [64,65]. Constant thermal conductivity of 150 W/mK is selected [40], which can be interpreted as reflecting the worst case scenario. Also, the specific heat of the GaN is set to 2.57×10^6 $\mathrm{Jm^{-3}K^{-1}}$ [54]. Therefore, by using the kinetic theory and the mean free path relation, the *phonon group velocity* is calculated $v = 438$ m/s. Inherently, the *relaxation time* for phonon scattering events is determined as $\tau = 914$ ps.

2.2.2. Finite Volume Discrete Ordinates Method

To solve phonon BTE, different numerical methods have been proposed previously for both gray and non-gray approaches. The solution can be conducted by Monte Carlo simulations, lattice Boltzmann method, or finite volume discrete ordinates method (FVDOM). Despite its accuracy, it has been reported that solving Monte Carlo method is not efficient for large domains such as semiconductor devices [86]. Both lattice Boltzmann method and FVDOM are effective in domain larger than 1 µm, yet they diverge regarding angular space discretization. To calculate phonon propagation accurately, along with spatial discretization, angular space discretization is also crucial in 2-D domains. It has been shown that lattice Boltzmann method cannot set enough phonon direction in the angular space which leads to ray effects [54], and results errors in temperature estimation. Therefore, finite volume discrete ordinates method is used in this study for solving gray phonon BTE.

In the FVDOM, phonon BTE is discretized for both angular and spatial space separately. Unlike classical finite volume method used for solving Fourier's law of

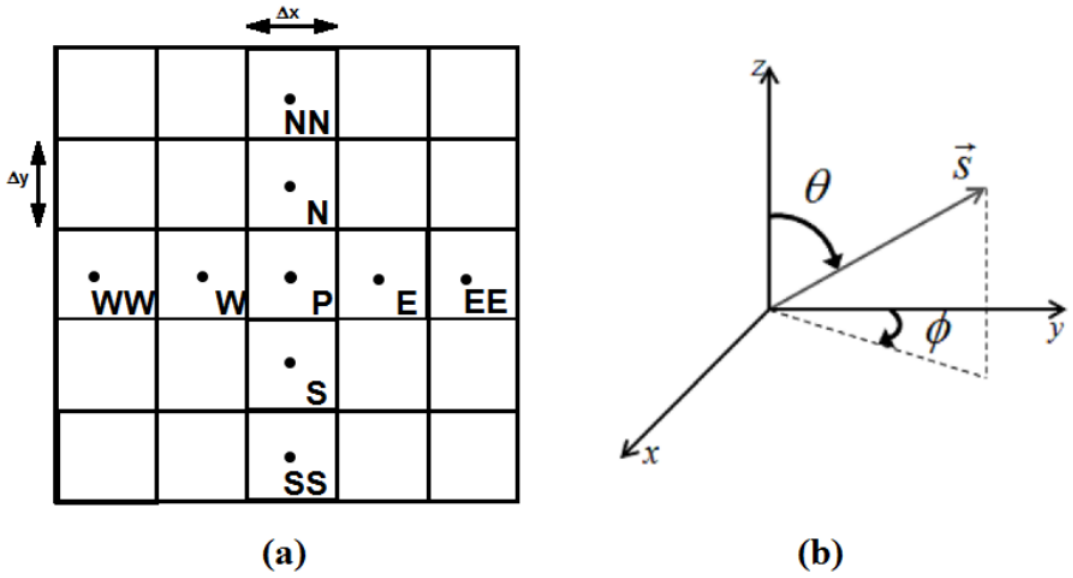


Figure 2.5. (a) Spatial discretization according to finite volume method, (b) angular discretization [54].

heat conduction, in this method, angular space should also be defined in order to account for different phonon propagation directions. Figure 2.5 represents the separate discretization of angular and spatial spaces.

2.2.2.1. Angular Discretization of Phonon BTE. The reason for implementing angular discretization is that spatial discretization of phonon BTE cannot account for phonon transport alone. Allowing phonons to propagate only in spatial points is not adequate. Consequently, discretization of angular space facilitates phonon movement along distinct directions in space, which imitates phonon transport effectively. Steady state angular discretized form of the gray phonon BTE is written as below:

$$\vec{s}_i \cdot \nabla \vec{v}_i e_i = \frac{e_i^0 - e_i}{\tau} + \dot{g}_i \tag{2.27}$$

In this form of the equation, subscript i denotes angular directions of variables, and $\vec{s}_i$ is the unit vector for each direction i.

Hence, by doing this, each property at nodal points in the spatial space is defined as accumulation of directional properties. The value of unit vectors and the number of directions rely upon the discretization method. Angular discretization can be implemented via S_N quadratures method, control angle method, and Gauss Legendre [91]. In this thesis S_N quadratures method is used for discretization since it eliminates ray effects and is relatively easy to implement.

In the S_N quadratures method, each central nodal point within the control volume can be treated as a sphere. At the center of this sphere, phonons propagate through distinct trajectories. Each direction is represented with i as in Equation 2.27, and directions are defined by a unit vector $\vec{s}_i(\mu_i, \gamma_i, \xi_i)$ and weighting constant w_i. It is practical approach to define directions in the octant of a spherical space, for instance directions of S_4 quadratures for angular discretization in an octant is given in Figure 2.6 [92].

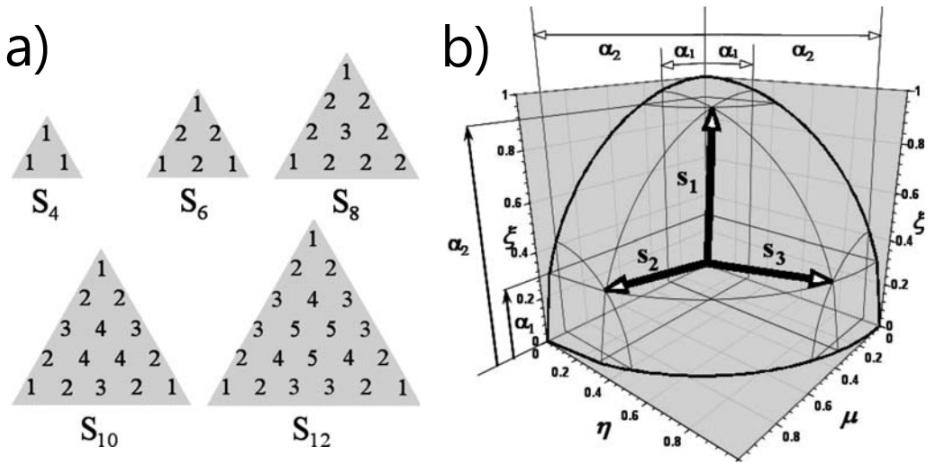


Figure 2.6. (a) SN quadratures in an octant in which each different number implies different weighing factor, (b) S4 quadratures in an octant [92].

Also, weighting factors are determined by considering Equations 2.28- 2.30.

$$\sum_{i=1}^{\text{Total direction}} w_i = 4\pi \tag{2.28}$$

$$\sum_{i=1}^{\text{Total direction}} |w_i \mu_i| = \pi \tag{2.29}$$

$$\sum_{i=1}^{\text{Total direction}} \left|w_i \mu_i^2\right| = \pi \tag{2.30}$$

Equation 2.29 stands for conservation of first moment, which facilitates determination of heat flux vectors. Moreover, with Equation 2.30, the conservation of the second moment is covered, which contributes to the rotational invariance. It should be noted that besides these restrictions, directions and weighting factors for S_N quadratures method can be found in the literature. To discretize phonon BTE in angular space quadrature values are obtained from the Fiveland's study [93]. Finally, after finding di-

rectional energies and weighting factors for angular discretization, lattice temperature is obtained by the correlation below:

$$e^0 = \sum_{i=1}^{\text{Total direction}} e_i w_i = c\,(T - T_{ref}) \tag{2.31}$$

2.2.2.2. Spatial Discretization of Phonon BTE. To solve Phonon BTE, angular discretized form of the gray phonon BTE equation is need spatial discretization which is implemented by finite volume method (FVM). The procedure for finite volume discretization is same with the solution of Fourier's law of heat conduction in the continuum scale model section. Overall, the 2-D domain, which is subjected to diffusive heat transport previously, is discretized into control volumes, which is called grid generation. The phonon energy densities at each central node of this domain are calculated by the information obtained from the neighboring control volumes. The difference between the spatial discretization of diffusive equation and phonon BTE rely upon the discretization scheme which will be explained in detail.

As conducted before for the diffusive governing equation, to implement finite volume method, first, angular discretized form of the phonon BTE is integrated over a control volume:

$$\int_{CV} \nabla \cdot (v_g \cdot s_i \cdot e_i)\, dV = \int_{CV} \frac{e_0 - e_i}{\tau} dV + \int_{CV} \dot{g} dV \tag{2.32}$$

After that, for representing the left-hand side of Equation 2.32 in terms of boundary fluxes, the equation can be transformed by using the divergence theorem:

$$\int_{A} \vec{n} \cdot (v_g \cdot s_i \cdot e_i)\, dA = \int_{CV} \frac{e_0 - e_i}{\tau} dV + \int_{CV} \dot{g} dV \tag{2.33}$$

The left-hand side of Equation 2.33 can be written as flux balance since it represents the phonons entering and leaving a control volume with different directions and energy densities attributed to them. Also, considering the values on the right-hand side are

constant in the control volume, Equation 2.33 is written as follows:

$$v_g s_{i,x} \Delta_y \left(e_i^w - e_i^e\right) + v_g s_{i,y} \Delta_x \left(e_i^s - e_i^n\right) = \frac{e_0^P - e_i^P}{\tau} \Delta_x \Delta_y + \dot{g}_i' \Delta_x \Delta_y \tag{2.34}$$

where $\dot{g}_i'$ is heat generation for per unit depth and lowercase letters represent the surfaces of the control volume (west, east, south, and north). Moreover, subscript x and y for unit vector ($s_{i,x}$, $s_{i,y}$) imply the horizontal or vertical components of the unit vector for a direction i.

However, Equation 2.34 is not sufficient alone for numerical calculation since the energy densities are defined by the boundary values of the control volume. As stated before obtaining information about phonon energy densities (e_i^w, e_i^e, e_i^s, e_i^n) entering or leaving from the surface of the control volume depends on the chosen discretization scheme, such as first order upwind, linear upwind, central differencing, or QUICK scheme. These discretization schemes must satisfy necessary properties, three of which are conservativeness, boundedness and transportiveness.

Conservativeness, basically, ensures the conservation of fluxes entering and leaving from the faces of control volume [94]. Considering Boltzmann transport equation, the energy densities of phonons entering and leaving the control volume from different directions must be equal for consistent results regarding whole domain. In numerical methods, after creating discretized equation, coefficients matrix is established, and iterative methods are performed with an initial guess until results converge. Boundedness is a constraint that provides the convergence of solution. Scarborough stated that coefficient matrix should be diagonal to attain convergence [95]. Lastly, transportiveness property considers the direction of a flow and its influence. Thus, it incorporates directional information into solution which is important for phonon propagation.

Given that accurate discretization scheme is crucial for calculations, it must be selected in a delicate manner as it should satisfy restrictions stated to obtain reasonable results. Regarding different discretization schemes, each has advantages and

disadvantages depending on the application. Although, first order upwind scheme satisfies conservativeness, boundedness and transportiveness, it has been stated that it yields highly diffusive transportation which ends up with error [96]. In the central differencing scheme, face values are calculated by the overall value of the central node (P) and the neighboring node. The central differencing scheme is used for diffusive heat transport as stated in the previous section, yet this approach diminishes the transportiveness property in terms of phonon propagation. Another effective scheme for many applications QUICK introduced by Leonard [97] accounts for second neighboring nodal points (NN, SS, WW, EE) for calculating properties of the central node P. However, study [15] showed that QUICK leads to errors if there is a sharp gradient which can be observed in ballistic heat transfer mechanism. Among these discretization schemes, linear upwind scheme (LUS) [98] is the most reasonable choice for phonon propagation since it admits conservativeness, boundedness, transportiveness and accuracy. Therefore, it is used for phonon BTE calculations in this study. In the LUS properties on the faces are calculated in accordance with the direction of the flow and second neighboring nodal points.

The same 2-D domain discretized for diffusive calculations is used for phonon BTE in the subcontinuum approach, yet the difference is that the second neighboring information is used for determining central nodal point in accordance with the LUS. Figure 2.5(a) illustrates the 2-D domain with second neighboring nodal points. Therefore, according to the linear upwind scheme surface energy densities in Equation 2.34 can be written as following:

$$e_i^e = e_i^p + \frac{e_i^P - e_i^W}{2} \quad (\rightarrow) \tag{2.35}$$

$$e_i^e = e_i^E + \frac{e_i^E - e_i^{EE}}{2} \quad (\leftarrow) \tag{2.36}$$

$$e_i^w = e_i^W + \frac{e_i^W - e_i^{WW}}{2} \quad (\rightarrow) \tag{2.37}$$

$$e_i^w = e_i^P + \frac{e_i^P - e_i^E}{2} \quad (\leftarrow) \tag{2.38}$$

$$e_i^n = e_i^P + \frac{e_i^P - e_i^S}{2} \quad (\uparrow) \tag{2.39}$$

$$e_i^n = e_i^N + \frac{e_i^N - e_i^{NN}}{2} \quad (\downarrow) \tag{2.40}$$

$$e_i^s = e_i^S + \frac{e_i^S - e_i^{SS}}{2} \quad (\uparrow) \tag{2.41}$$

$$e_i^s = e_i^P + \frac{e_i^P - e_i^N}{2} \quad (\downarrow) \tag{2.42}$$

It should be noted that the value of the integrated energy density changes with the direction of the phonon propagation. For instance, if the phonon propagates towards node (P) to node (E) the energy density at the east surface of the control volume is different than the phonon propagation in reverse direction. These propagation directions stem from the angular discretization which is presented before. Hence, the surface values of a phonon also rely upon the horizontal and vertical components of the unit vector. Substituting Equations 2.35- 2.42 into Equation 2.34, the governing equation for interior nodes can be obtained as following:

$$\begin{aligned} a_i^P e_i^P = a_i^N e_i^N + a_i^{NN} e_i^{NN} + a_i^S e_i^S + a_i^{SS} e_i^{SS} + a_i^E e_i^E + a_i^{EE} e_i^{EE} + a_i^W e_i^W \\ + a_i^{WW} e_i^{WW} - \sum_J K_{ij} e_j^P - \dot{g}_i' \end{aligned} \tag{2.43}$$

in which summation term represents the scattering events and is called scattering matrix and is defined by the steps below:

$$\frac{e_0^P - e_i^P}{\tau} = \frac{\sum_j w_j e_j - e_i^P}{\tau} = \sum_J \left(\frac{w_i}{\tau} - \frac{\delta_{ij}}{\tau} \right) e_j^p \tag{2.44}$$

where δ_{ij} is dirac delta. Moreover, coefficients can be determined depending on the phonon direction which can be acquired from the unit vector. Thus, considering the unit vector for the 2-D domain $\vec{s_i}(\mu_i,\gamma_i) = \mu_i\mathbf{i}+\gamma_i\mathbf{j}$, coefficients can be defined as following:

$$a_i^E = \begin{cases} \frac{-2v_g\mu_i}{\Delta_x}, \mu_i < 0 \\ 0 \quad , \mu_i > 0 \end{cases} \tag{2.45}$$

$$a_i^W = \begin{cases} \frac{2v_g\mu_i}{\Delta_x}, \mu_i > 0 \\ 0 \quad , \mu_i < 0 \end{cases} \tag{2.46}$$

$$a_i^N = \begin{cases} \frac{-2v_g\gamma_i}{\Delta_y}, \gamma_i < 0 \\ 0 \quad , \gamma_i > 0 \end{cases} \tag{2.47}$$

$$a_i^S = \begin{cases} \frac{2v_g\gamma_i}{\Delta_y}, \gamma_i > 0 \\ 0 \quad , \gamma_i < 0 \end{cases} \tag{2.48}$$

$$a_i^{EE} = \begin{cases} \frac{-v_g\mu_i}{2\Delta_x}, \mu_i < 0 \\ 0 \quad , \mu_i > 0 \end{cases} \tag{2.49}$$

$$a_i^{WW} = \begin{cases} \frac{v_g \mu_i}{2\Delta_x}, \mu_i > 0 \\ 0 \quad , \mu_i < 0 \end{cases} \tag{2.50}$$

$$a_i^{NN} = \begin{cases} \frac{-v_g \gamma_i}{2\Delta_y}, \gamma_i < 0 \\ 0 \quad , \gamma_i > 0 \end{cases} \tag{2.51}$$

$$a_i^{SS} = \begin{cases} \frac{v_g \gamma_i}{2\Delta_y}, \gamma_i > 0 \\ 0 \quad , \gamma_i < 0 \end{cases} \tag{2.52}$$

The coefficient of the central node can be defined by summation of functions:

$$a_i^P = f_1 + f_2 + f_3 + f_4 \tag{2.53}$$

$$f_1 = \begin{cases} \frac{3v_g \mu_i}{2\Delta_x}, \mu_i > 0 \\ 0 \quad , \mu_i < 0 \end{cases} \tag{2.54}$$

$$f_2 = \begin{cases} \frac{-3v_g \mu_i}{2\Delta_x}, \mu_i < 0 \\ 0 \quad , \mu_i > 0 \end{cases} \tag{2.55}$$

$$f_3 = \begin{cases} \frac{3v_g \gamma_i}{2\Delta_y}, \gamma_i > 0 \\ 0 \quad , \gamma_i < 0 \end{cases} \tag{2.56}$$

$$f_4 = \begin{cases} \frac{-3v_g \gamma_i}{2\Delta_y}, \gamma_i < 0 \\ 0, \gamma_i > 0 \end{cases} \tag{2.57}$$

Therefore, along with the coefficients, Equation 2.43 is the governing equation for the interior nodes of the 2-D domain subjected to the sub-continuum heat transport. However, to include boundary conditions, modifications are needed for Equation 2.43. Below is a list of boundary conditions and their application to phonon BTE solutions.

Temperature: The easiest boundary modification is prescribed boundary temperature. If the boundary has a specified temperature, it is assumed that energy densities of the phonons propagating towards the domain from the boundary have the same energy that can be derived from the temperature of the boundary as follows:

$$e_{i,inwardboundary} = cT_{boundary} \tag{2.58}$$

It should be noted that since the linear upwind scheme is used for discretization scheme, fictitious neighboring nodal points outside the domain are modelled as having prescribed temperature for this kind of boundary.

Adiabatic Boundary: An adiabatic boundary can be modelled by two distinct approaches which are *specular* and *diffuse* reflections. With the *specular* approach, phonon energy densities having diverse directions and proceeding towards the *specular* boundary are reflected by the same properties. This can be expressed as:

$$e_{reflected} = e_{in} \tag{2.59}$$

where e_{in} stands for phonons moving through specular boundary, and $e_{reflected}$ is phonons that are reflection of the e_{in}. Figure 2.7 (a) shows this type of boundary. However, it has been stated that the fully reflective boundary cannot calculate the real phonon behaviors at the adiabatic boundary [99], so that the *diffuse* reflection conditions should be used. In *diffuse* reflection condition, instead of reflecting at the boundary, phonons having the equilibrium energy density at the boundary propagate towards the domain. Therefore, this situation can be written in terms of equilibrium

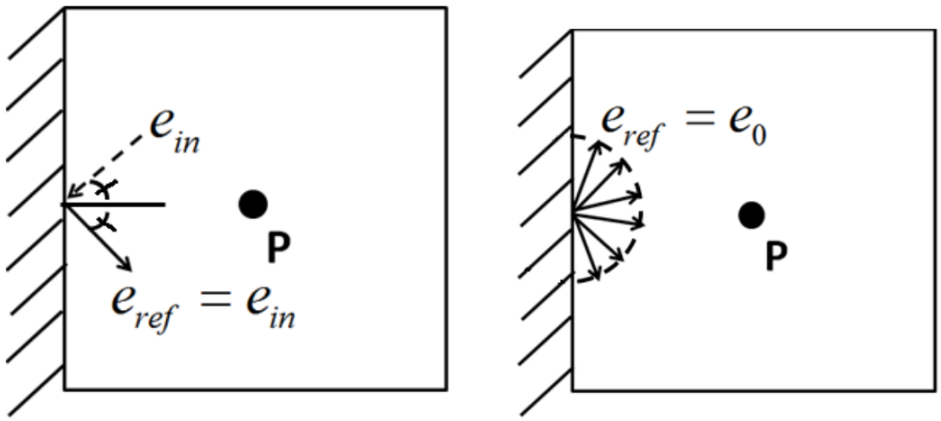


Figure 2.7. (a) Specular reflection boundary condition, (b) diffuse reflection boundary condition. [54]

phonon energy density at the boundary.

$$e_i^{inward} = \sum_j w_j e_j \tag{2.60}$$

To separate outward phonon propagation from inward phonon propagation, Equation 2.59 can be written as:

$$e_i^{inward} = \sum_j w_j e_j^{outward} \alpha_j + \sum_j w_j e_j^{inward} (1 - \alpha_j) \tag{2.61}$$

In Equation 2.61, the value of α_j changes in accordance with the phonon direction or the unit vector. For instance, considering a diffusive reflection boundary at the upper wall of a 2-D domain (at y_{max}), the value of the α_j than can be defined as:

$$\alpha_j = \begin{cases} 1 & , \quad \gamma_i > 0 \\ 0 & , \quad \gamma_i < 0 \end{cases} \tag{2.62}$$

Since the e_i^{inward} is constant for all directions at the boundary, Equation 2.61 can be rearranged as following

$$e_i^{inward} = \frac{\sum_j w_j e_j^{outward} \alpha_j}{1 - \sum_j w_j (1 - \alpha_j)} \tag{2.63}$$

Constant heat flux: In order to define a constant heat flux at a boundary in phonon BTE calculations, steps analogous to *diffuse* reflection modifications are followed. However, firstly, heat flux in terms of the phonon energy densities should be defined. Considering the upper wall again, if heat flux is implemented to the boundary, it can be defined as:

$$\vec{q} = \sum_j S_{j,y} w_j e_j^{inward} v_g \tag{2.64}$$

where $S_{j,y}$ is unit vector component along the y-axis for a given direction. Since there is a one band in the gray phonon BTE model, v_g is constant. Also, inward and outward phonon propagations can be separated as below:

$$\frac{\vec{q}}{v_g} = \sum_j S_{j,y} w_j e_j^{\text{outward}} \alpha_j + \sum_j S_{j,y} w_j e_j^{\text{inward}} (1 - \alpha_j) \tag{2.65}$$

The value of α_j changes in accordance with the phonon direction, and Equation 2.62 is valid for this case also. Assuming that inward phonons propagate with same energy density in each direction as a result of the applied heat flux from the boundary, Equation 2.65 can be written as:

$$e_j^{inward} = \frac{1}{\sum_j S_{j,y} w_j (1 - \alpha_j)} \left(\frac{\vec{q}}{v_g} - \sum_j S_{j,y} w_j e_j^{outward} \alpha_j \right) \tag{2.66}$$

As a result of the discretization, depending on the number of nodes, algebraic equations are obtained for each direction. The solution for the coefficient matrix is written as below:

$$\mathbf{Ae} = \mathbf{C} \tag{2.67}$$

where the **A** represents the coefficients matrix and the diagonal terms of the scattering matrix. It can be written as following:

$$\begin{bmatrix}
a_i^P + K_{ii} & a_i^E & a_i^{EE} & \dots & a_i^N & \dots & a_i^{NN} & \dots & & & & & & & \\
\vdots & & & & & & & & & & & & & & \\
 & & & & & & \ddots & & & & & & & & \\
\dots & a_i^{SS} & \dots & a_i^S & \dots & a_i^{WW} & a_i^W & a_i^P + K_{ii} & a_i^E & a_i^{EE} & \dots & a_i^N & \dots & a_i^{NN} & \dots \\
 & & & & & & & & \ddots & & & & & & \\
 & & & & & & & & & & & & & & \vdots \\
 & & & & & & & \dots & a_i^{SS} & \dots & a_i^S & \dots & a_i^{WW} & a_i^W & a_i^P + K_{ii}
\end{bmatrix} \tag{2.68}$$

where K_{ii} represents the diagonal terms of the scattering matrix. Also, the energy density matrix **e** can be written as below:

$$\mathbf{e} = \begin{bmatrix} e_{i,1} \\ e_{i,2} \\ e_{i,3} \\ e_{i,4} \\ \vdots \\ \vdots \\ \vdots \\ e_{i,N} \end{bmatrix} \tag{2.69}$$

Finally, the matrix **C** incorporates boundary effects, volumetric heat generation, and the off-diagonal parts of the scattering matrix.

$$\mathbf{C} = \begin{bmatrix} C_{i,1} \\ C_{i,2} \\ C_{i,3} \\ C_{i,4} \\ \vdots \\ \vdots \\ \vdots \\ C_{i,N} \end{bmatrix} + \sum_{J} K_{ij} e_j \left(1 - \delta_{ij}\right) \tag{2.70}$$

The matrix system shown in Equation 2.67 is solved by MATLAB built-in function generalized minimum residual method. The procedure followed can be summarized by this: For the 2-D domain, first, the diffusive governing equation is solved by the finite volume method explained earlier. After obtaining the temperature values for each nodal point within the control volumes, these values are used for calculating initial energy densities for each direction. Afterwards, the matrix system shown in Equation 2.67 is solved and is revised for each direction successively by generalized minimum residual method. Rest of the procedure after the first initialization is carried out by iterations until the left and right-hand sides of Equation 2.67 become adequately closer depending on the tolerance. Finally, the lattice temperatures can be obtained from Equation 2.31.

The domain in Figure 2.1 is discretized by 640,000 nodes spatially (800×800). In order to discretize angular space for phonon BTE, S_3 quadaratures is used. Therefore, 12 distinct directions are defined to phonons at each nodal point. Along with the angular discretization, the degree of freedom for the gray phonon BTE becomes $12 \times 640,000 = 7,680,000$.

2.3. Results

In Figure 2.8, the discrepancies between the continuum and sub-continuum approaches in terms of heat generation application are represented by their maximum temperature rise (from the 300 K base temperature) estimation difference in the domain. Thus, these differences can be interpreted as size effects that cannot be captured by the continuum model. Since the thermal conductivity is set constant, a linearity has been observed between the temperature rise values and the power input, therefore the temperature rise values are given with a constant multiplier n which indicates the power input. The value of n takes 1, 3, and 10 for power conditions 1 W/mm, 3 W/mm, and 10 W/mm, respectively. Therefore, for the all area sizes, the aspect ratios, and the simulation types, the maximum temperature rise values increase with a higher power input.

In Figure 2.8, for all power conditions and aspect ratios, the highest temperature difference between continuum and non-continuum simulations occur with the smallest heat generation area (0.004 µm^2). Also, the difference between the two methods is inversely proportional to the area size. For example, considering the constant $a_r = 2$ profiles, when the heat generation area is decreased from 5A to A, the difference of the

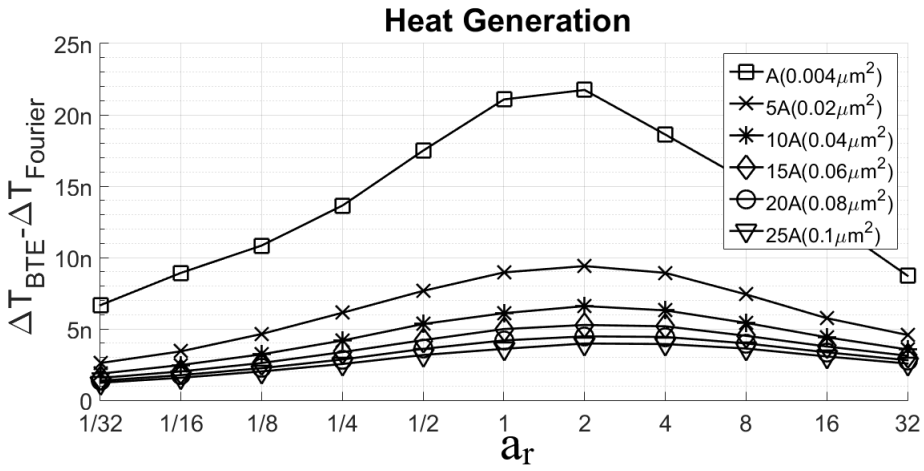


Figure 2.8. Discrepanies between continuum and sub-continuum approach in terms of volumetric heat generation.

continuum and the sub-continuum approaches $\sim 12.3n$°C. Yet, if the generation area is decreased from 25A to 20A, only $\sim 0.5n$°C increment occurs.

When the heat generation area size and power input are kept constant, the highest differences between the two methods are observed when the heat generation region aspect ratio is a_r=2. Since the heat generation is defined adjacent to an adiabatic boundary, which also acts as a symmetry boundary condition, a_r=2 corresponds to a square heat generation profile with equal and large distance to constant temperature boundaries acting as heat sinks. Thus, the difference between the two methods can be as high as $\sim 21.7n$°C when the smallest heat generation area (A) having a_r=2 is applied. With the same aspect ratio, this difference drops to $\sim 3.9n$°C if the area is the biggest (25A). Increasing and decreasing the aspect ratio, while keeping the heat generation area constant, decreases the maximum temperature difference. For instance, the highest difference reported as $\sim 21.7n$°C decreases by $\sim 15n$°C and $\sim 13n$°C when the aspect ratio is changed to 1/32 and 32, respectively. Also, horizontal and vertical lengths affect the temperature rise slightly different. This behavior is seen in all cases, such that when the inverse ratios of the aspect ratios are compared, the heat generation profiles with a longer horizontal length always yield slightly higher discrepancy between the continuum and sub-continuum approaches if the area size is kept constant. The trend can be attributed to the symmetry condition adjacent to the heat generation and diffusive reflective boundary in the phonon BTE model. Results show that, in devices, alongside the lateral length of the Joule heating profile, area size and the power conditions have significant impact on the size effects as well. Moreover, if the localized Joule heating profile is sharp (around a_r=2) in a device, sub-continuum methods must be used due to magnified size effects. When the Joule heating profile is horizontally or vertically spread and has a relatively big area size, continuum models could be used for device characterization in low power conditions.

The results of the heat flux boundary condition on thermal size effects of localized Joule heating is given by Figure 2.9. The area values in this figure stand for the area size of the integrated heat generation area. According to Figure 2.9, for the con-

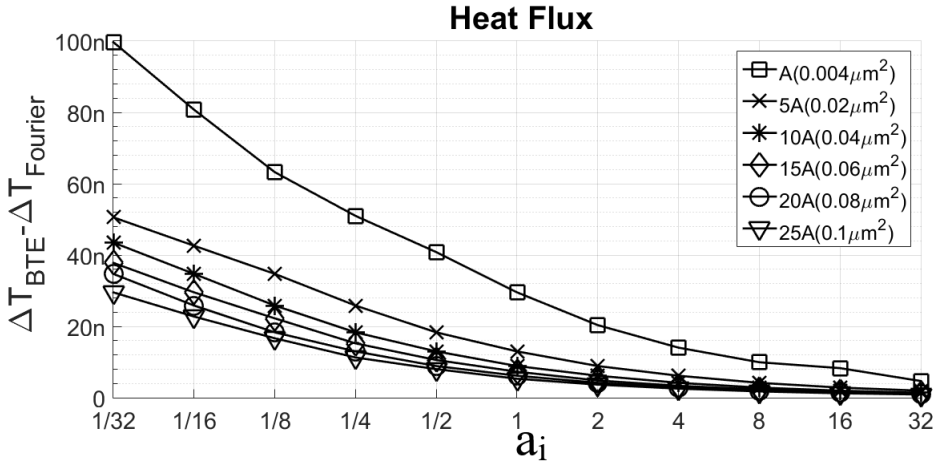


Figure 2.9. Discrepancy between continuum and sub-continuum approach in terms of heat flux boundary application.

stant heat generation area sizes and the power inputs, highest temperature difference between sub-continuum and continuum model is observed when the a_i is 1/32 and it drops significantly if the a_i approaches to 32. Since heat flux data is acquired by the integration over the y-axis, when the power is same and the flux data is derived from a heat generation area with a smaller aspect ratio, higher amount of heat flux is applied to a smaller region on the boundary. This enhances the size effects more and leads to higher difference between the two methods. The highest difference between the continuum and sub-continuum estimations is $\sim 100n^{\circ}$C when the area and the aspect ratio of the integrated generation profile are A and 1/32, respectively. Yet, this deviation can be as small as $\sim 4.6n^{\circ}$C when a_i =32. Also, the minimum difference between the continuum and sub-continuum approaches is $\sim 0.9n^{\circ}$C when the heat source area and aspect ratio, thus the length of the region where heat flux is applied, are largest. When the a_i =32, the temperature difference between sub-continuum and continuum models changes only by $\sim 3.5n^{\circ}$C, when the area is changed from A to 25A. Aside from the smallest integrated area size (A), implementation of the rest of the area sizes as a boundary flux yield almost the same maximum temperature difference ($\sim 0.5n^{\circ}$C) between the continuum and sub-continuum methods. Therefore, devices with horizontally spread Joule heating profiles could be modeled as boundary flux in continuum methods without causing size effects much if the power is low enough and

the area size is relatively big. However, it should be avoided for high powers and small area sizes. Also, it must be avoided if the Joule heating profile in a device is vertically predominant.

Finally, to understand if the size effects can be estimated by heat flux approximation instead of volumetric heat generation in domain, the peak temperature differences in the two methods are compared. As size effects can only be captured by phonon BTE solution, only sub-continuum results from the heat generation and the boundary flux applications are considered. The ability of heat flux approximation to determine volumetric heat generation effects on the maximum temperature is given by error calculation which is given as following:

$$\text{Error} = \frac{(T_{\text{max,BTE}})_{\text{HeatFlux}} - (T_{\text{max,BTE}})_{\text{HeatGeneration}}}{(T_{\text{max,BTE}})_{\text{HeatGeneration}}} \tag{2.71}$$

where $(T_{max,BTE})_{HeatFlux}$ and $(T_{max,BTE})_{HeatGeneration}$ represent the maximum temperatures occur in the domain as a result of heat flux boundary and volumetric heat generation.

The errors are given in Figure 2.10. Since the error values do not change with constant n factor unlike the temperature differences presented previously, the errors

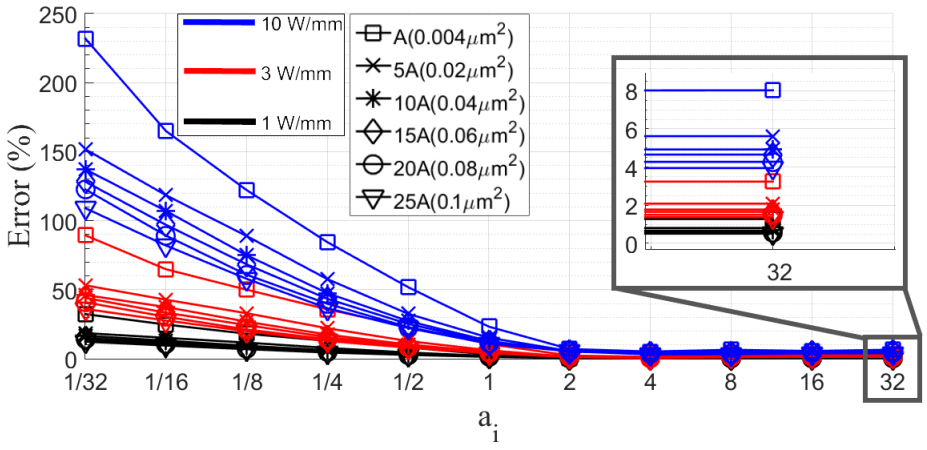


Figure 2.10. Deviation between heat flux and volumetric heat generation results in phonon BTE.

for all three power conditions are given separately in Figure 2.10. It can be seen that, for the same area size and aspect ratio, a higher power input always yields higher error when the volumetric heat generation is approximated by heat flux boundary. However, same trends are observed for all power conditions. Errors surge with using heat generation areas with a smaller aspect ratio. Also, when the aspect ratio of the integrated heat generation area (a_i) approaches to 1/32, the rate of change of the increment rise significantly with a smaller heat generation area. For instance, the error can reach up to ∼230%, ∼89%, and ∼32% with the smallest area and aspect ratio when the powers for per unit depth are 10 W/mm, 3 W/mm, and 1 W /mm, respectively. Whereas, when the area size is increased to 25A, for the same aspect ratio these values drop to ∼109%, ∼36%, and ∼13% for 10 W/mm, 3 W/mm, and 1 W/mm, respectively. After the $a_i = 2$, along with increasing the aspect ratio of integrated generation area, the area size influence on the error and the discrepancy between the two methods drop significantly. Considering the errors when the $a_i = 32$, for the highest power input, errors vary from ∼4% to ∼8% depending on the area size, which can be seen in Figure 2.10 zoomed-in view. These errors drop to 3.2% and 1.5% for the 3 W/mm. Lastly, when the power is 1 W/mm the errors for heat flux implementation are found between 1.2% and 0.5% depending on the area size. Therefore, the heat flux approximation instead of volumetric heat generation relies upon the heat generation profile and the power input. If the heat generation profile is vertically predominant, approximation could lead to error as much as ∼230% with 10 W/mm. Although area size alters the error, for a vertically predominant profile high errors persist. On the other hand, when the profile is horizontally spread, it has been observed that error values range from ∼0.5% to ∼8%. Thus, if a device is subjected to horizontally spread Joule heating, size effects can be modeled with a heat flux boundary by using BTE, which could ease computational cost.

3. A CASE STUDY: AlGaN/GaN HEMTS

3.1. AlGaN/GaN HEMTs and Joule Heating Profile

As discussed in Chapter 1, many semiconductor devices suffer from the sub-continuum heat transport as a result of nanometer scale self-heating regions. However, the devices operated for high power applications are affected most due to the nonuniform electric field distribution and the high-power densities. High power transistors are pertinent example for these devices. Particularly, AlGaN/GaN HEMTs (Figure 3.1) are subject to non-diffusive heat transport since they are engineered to operate at high power conditions at which conventional silicon-based devices cannot. Therefore, to see the sub-continuum heat transport effects in a real device, in this chapter, an AlGaN/GaN HEMT is simulated by an electro-thermal model which accounts for the size effects. However, first, the working principles of the AlGaN/GaN HEMTs should be understood.

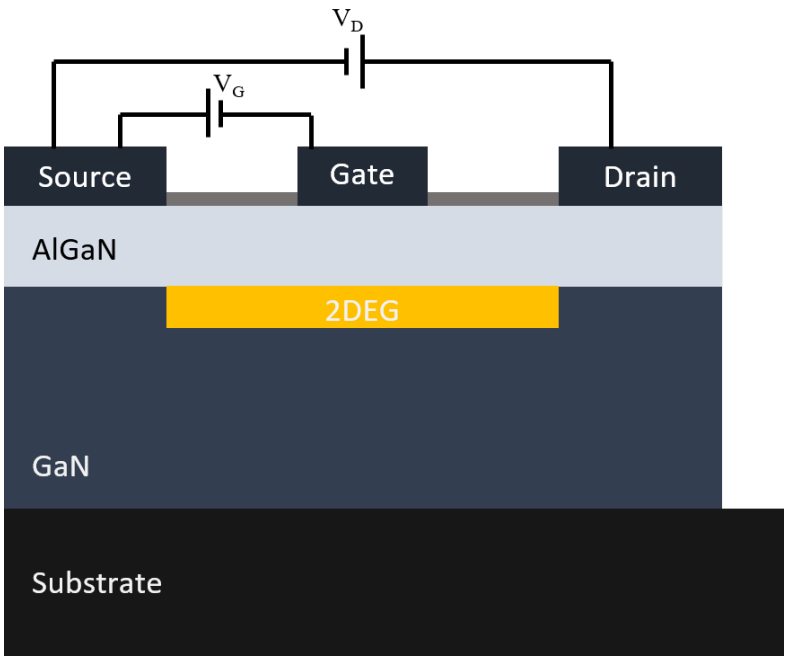


Figure 3.1. 2-D structure of AlGaN/GaN HEMT.

GaN (Gallium Nitride) is acknowledged to be a wide bandgap semiconductor. Thus, as explained in the introduction, GaN has higher band gap compared to conventional semiconductor materials and is used prevalently in solid-state devices. Also, the comparison of the material properties between GaN and the other prevalent materials is given in Table 1. GaN has bandgap of 3.4 eV [100], and due to the high bandgap value, it has high break down voltage (3 MV/cm) [100]. As the breakdown voltage represents the adequate amount of voltage to free electrons in a semiconductor material, the high breakdown voltage of GaN facilitates GaN based devices to operate at higher voltage values. Since operating temperature effects electrical conductivity, as a result of wide bandgap, GaN devices can operate at higher temperature values compared to silicon devices. Moreover, high current densities can be obtained by virtue of the large electron saturation velocity (3×10^7cm/s) [100]. Due to the unique properties of GaN, AlGaN/GaN HEMTs become invaluable for high power applications, such as advance radar systems, high frequency electronic devices [10].

Besides unique properties of GaN, the features that differentiate AlGaN/GaN HEMTs from other transistors are AlGaN/GaN heterojunction and piezoelectric polarization of GaN. The heterojunction is created by utilizing molecular beam epitaxy commonly [101]. By merging two semiconductors with different band structures, electrical behavior at the interface is affected by the properties of the materials. The AlGaN/GaN interface creates discontinuity in the electron band structure at the GaN side of the interface. Thus, electrons are trapped at the GaN side of the interface which is called quantum well. Also, by virtue of the piezoelectricity of GaN, carrier density is increased at the interface since the AlGaN layer induces strain. The region, where trapped electrons reside and the electric current occurs, is called 2DEG (two-dimensional electron gas).

Although there are varieties of AlGaN/GaN HEMT designs, a regular device structure consists of contacts, AlGaN/GaN interface and substrate, which can be seen in Figure 3.1. Source, gate, and drain parts are used for regulating electrical behavior of the device and current flow from source to drain. Therefore, these parts are created

by highly conductive materials such as gold, copper, and titanium. Passivation layer on the device surface hinders the electron leakage from the device channel, and this layer is generally crated by nitride or oxide insulators. The GaN layer enables conductive environment to the electron gas along with AlGaN as explained before. Also, the substrate is utilized for removing heat from the localized heat generation region and mechanical support. Thus, the substrate layer is selected from materials with high thermal conductivity, such as silicon carbide (SiC) or sapphire. For more intense operation conditions, diamond can also be used.

Along with the interface, the functionality of the device depends on the applied voltages from the contacts which are shown in Figure 3.1. By applying a voltage between the source and gate contacts (V_G), electrons at the interface can be controlled. If positive voltage is applied between the source and gate, trapped electrons are excited and electric current is induced. However, electric current can still be induced even there is no voltage difference due to the high density of the trapped electrons in GaN. Moreover, applying a positive voltage to the gate yields higher electric current which is called open channel condition. Reversely, by applying a negative voltage between the source and the gate, electric current is confined to a smaller region in the channel, which reduces amount of the current.

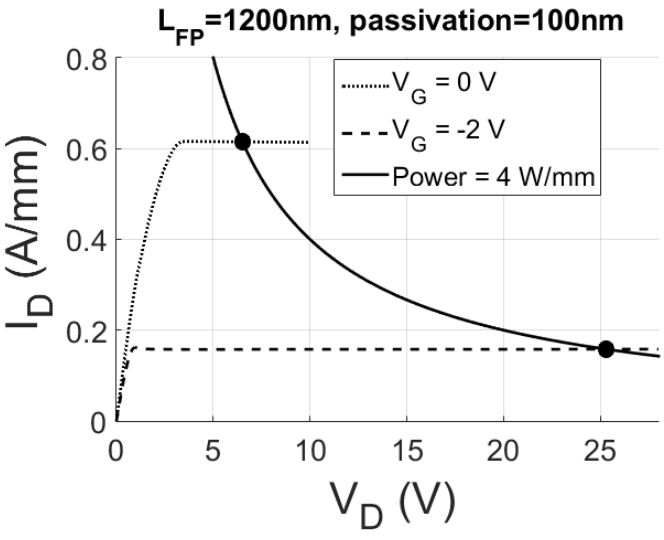


Figure 3.2. I-V curve of an AlGaN/GaN HEMT [32].

Electrical behavior of AlGaN/GaN HEMT under DC operating condition is given in Figure 3.2, and the relation of current, drain voltage and gate voltage is called biasing conditions. It can be seen that the current between the source and drain contacts is regulated by the potential difference between the source and gate, which is called gate voltage. In the I-V curve, the relation between the drain voltage and current changes at a threshold voltage which is called knee voltage. Before the knee voltage, current rises along with the drain voltage increment and this region is called linear region. After exceeding the knee voltage, the region is called saturation region in which current becomes constant. Also, it can be seen from Figure 3.2, when the device operates at partially pinched-off condition (V_G= -2 V), channel current decreases significantly so that to operate at same power condition higher drain voltage is required. After some critical potential difference between source and drain, device reaches to pinched-off condition in which electrons cannot pass through drain and the value of current becomes zero.

Although there are mechanical and electrical issues having bearing on the reliability of the AlGaN/GaN HEMTs, objective of this study will be confined to investigating thermal aspects which are also associated with the other degradation instances. As explained in Chapter 1, thermal issues are associated with the Joule heating in the device due to the electron flow inside the 2DEG region. It has been reported that depending on the operation condition, lateral size of the Joule heating profile in the AlGaN/GaN HEMTs can be found nanometer scale, which highlights the importance

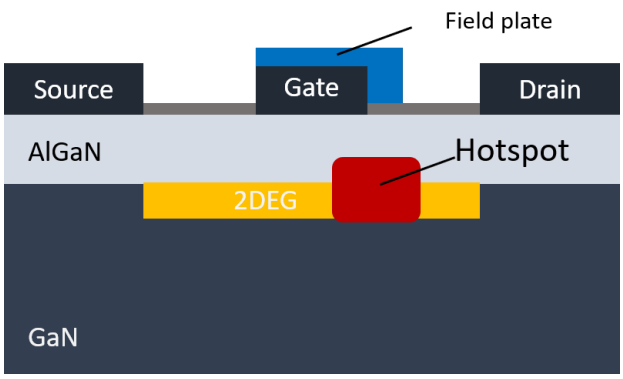


Figure 3.3. Hotspot in AlGaN/GaN HEMT.

of the sub-continuum heat transport in these devices. The localized heat generation in these devices generally occurs at the drain side of the gate which is illustrated in Figure 3.3. This area is generally called hot-spot in which peak device temperatures are observed. The formation of Joule heating profile in the 2DEG region depends on biasing condition of the device and device structure, such as the auxiliary parts like the field plates and passivation layers. When the device operates under partially pinched-off condition, the area in which electrons can pass through is confined by the electric field, thus electrons scatter with phonons in a smaller region. This phenomenon causes smaller heat generation profiles around the hot-spot region, and it leads to higher peak temperature values. Inherently, under the partially pinched-off condition, size effects are magnified. These biasing effects can be seen from Figure 3.4. This shows that compared to open channel condition (V_G=0 V), the heat generation profile occurs in a more confined region when the device operates with negative gate voltage, which is anticipated to bring about more pronounced size effects in the domain.

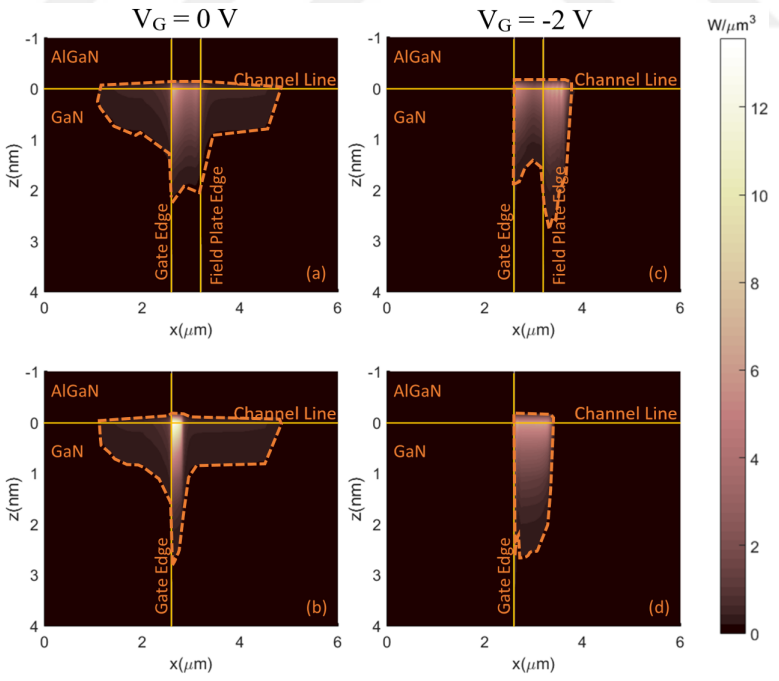


Figure 3.4. Joule heating profile in AlGaN/GaN HEMT operating at P =4 W/mm. (a) and (c) show device with gate field plate structure, (b) and (d) represents devices without field plate. [32]

To spread the localized heat generation in the device and to cope with high temperature values, several approaches have been investigated. As explained before, substrate layer with high thermal conductivity can be used for effective heat removal. However, since the Joule heating results from the nonuniform electric field distribution in the 2DEG, methods for regulating electric field are also used for thermal management. The field plate structure, given in Figure 3.3, is a striking example for the current technology regarding the regulation of electric field and the Joule heating distribution in the device.

Although the field plate and the passivation layers are used for regulating electric field primarily, their effects on the hot-spot temperature have been investigated for different device layouts. The field plate structure can be placed on the source and the gate metal contacts. For instance, with the dual field plate concept, both source and gate contacts have field plate, and the effects of this concept were investigated with electro-thermal approaches [102, 103]. Also, single field plate structures are also used prevalently. It is known that a single field plate placed either on the gate or the source metal contacts can regulate electric field and spread localized heat generation, such as it was reported that by changing the field plate length on the source contact, the maximum device temperature can be altered [32].It can be seen from Figure 3.4 that the Joule heating profile can be changed by the gate field plate.

Consequently, localized heat generation profile can be changed by device parameters and non-uniform profile occurs. Therefore, instead of a fictitious domain, a real device structure is modeled with electro-thermal multiscale model coupled with phonon BTE. The heating profile effects on the device peak temperature and the accuracy of the heat flux approximation in the device is discussed in this chapter.

3.2. Multiscale Model

Multiscale model is needed for investigating the Joule heating profiles in AlGaN/GaN HEMTs. Since size effects are anticipated in the 2DEG region of the de-

vice, multiscale model should include phonon BTE model also. Moreover, the results from the multiscale model are used in the next chapter for assessing accuracy of the experimental methods. Thus, a complete multiscale model that has a package level AlGaN/GaN HEMT device and accounting for sub-continuum thermal transport is created.

Quarter of the investigated device structure is given in Figure 3.5 with symmetry condition. It can be seen that the device has multiple gate, source, and drain metal contacts. These types of devices are called multi-finger devices, and the peak temperature values are observed at the inner finger of the device. For thermal analysis, 8 finger AlGaN/GaN HEMT is modelled in this study. So as to incorporate package level heat transport into the model, a realistic GaN HEMT is modelled as given in Figure 3.5. It is important to model all layers since they impact the heat removal from the hot-spot, hence influence maximum temperature. Thus, along with the AlGaN and the GaN layers, model also includes SiC substrate and copper package, as well as epoxy between the substrate and the package.

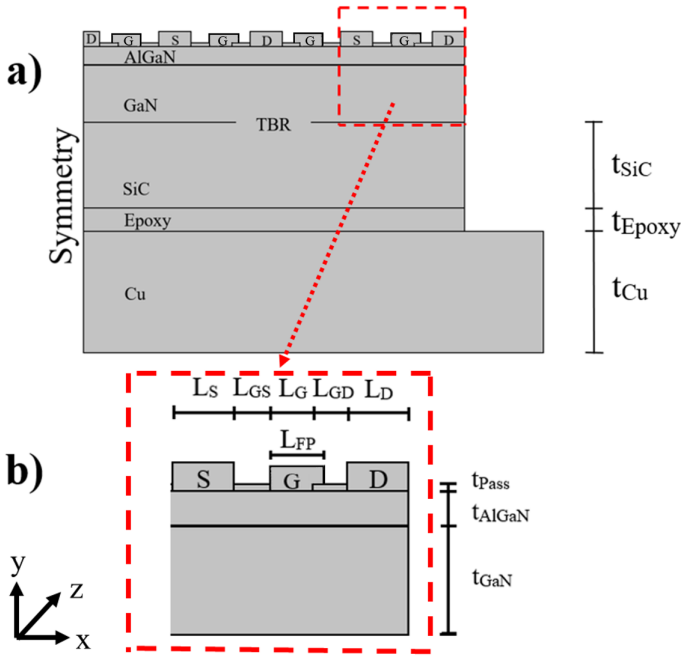


Figure 3.5. 2-D structure of the (a) investigated AlGaN/GaN HEMT and (b) single finger of the device.

The lengths of the metal contacts are defined 600 nm, 46 µm, 28 µm for the gate (L_G), the source (L_S), and the drain (L_D), respectively. The distance between the gate and source contacts (L_{GS}) is set to 1 µm. Also, the gap between the gate and drain contacts (L_{GD}) is defined 2.4 µm. The device is modelled with gate field plates and without field plates for comparison purpose. For the gate field plated device, the length of the field plate (L_{FP}) is defined 1000 nm, and the thickness of the field plate (t_{FP}) is set to 300 nm. Also, the device has a passivation layer of 200 nm(t_{pass}) Si_3N_4. The AlGaN and GaN layers are defined with 20 nm (t_{AlGaN}) and 5 µm (t_{GaN}) thicknesses, respectively. The SiC substrate has t_{SiC} =125 µm thickness, 600 µm length and 300 µm width through z-axis. Also, the copper package is defined with, t_{Cu} = 4 mm thickness, 30 mm length and 15 mm width on z-axis. Finally, t_{epoxy}= 20 µm is defined between the SiC and Cu layers.

The steps given in Figure 3.6 are followed in the multiscale model to understand the Joule heating profile effects in the AlGaN/GaN HEMT. First, electrical simulation is conducted for obtaining the heat generation distribution in the device. Only one finger of the device is modelled in the electrical simulations as it was reported that the presence of the neighboring fingers does not affect the electrical behavior [41]. Also, the electrical model for the single finger(Figure 3.5 (b)) is modelled in the 2-D domain to reduce computational effort since the width of the gate is much longer than the active channel length. After obtaining heat generation data, 3-D diffusive thermal model is employed. The heat generation data is implemented in the 3-D diffusive

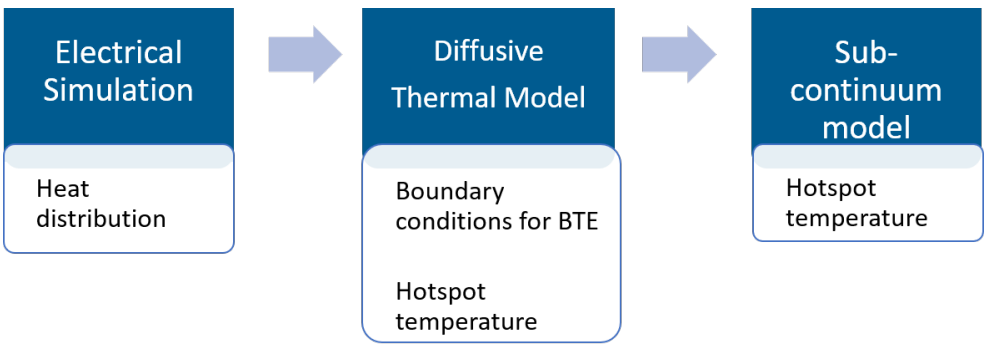


Figure 3.6. Process for multiscale model.

model to mimic AlGaN/GaN HEMT operation. The 3-D model includes all layers given in Figure 3.5 (a), and the results from this model are important for calculating the phonon BTE. The boundary conditions and the average thermal conductivity value for the the phonon BTE model are obtained via the 3-D model. Lastly, by using the phonon BTE model presented in Chapter 2, the maximum temperature at the hotspot region is calculated by accounting for size effects. Since each step is conducted in a separate platform, electrical simulation and thermal model are explained individually.

3.2.1. Electrical Model

The accuracy of the electro-thermal multiscale model can be attributed to prediction of the Joule heating in the operating device. As explained in Chapter 1, Joule heating starts with the electron-phonon interactions within the device active layer, thus modelling the electron transport accurately is imperative for the device simulation.

Electron transport can be modelled by various approaches regarding the required accuracy for a given domain. For instance, the Schrödinger-Poisson equations can determine the electron flow. However, this method needs high computational performance for 2-D and 3-D domains since the two coupled equations are solved numerically. Another way of calculating electron transport in the domain is Monte Carlo method. In this method, the domain can be modelled by either considering electron transport only or also including acoustic and optical phonon events. Thus, AlGaN/GaN HEMTs were modelled using this method in the past [104, 105]. Yet, it is not effective if the computational efficiency is desired. Lastly, the Boltzmann transport equation can be operated for electron transport simulations. From the electron BTE, drift diffusion, thermodynamic, and hydrodynamic equation sets are derived for semiconductor device analyses. The drift-diffusion model is an isothermal model, so it is not accurate for obtaining self-heating data. In the thermodynamic method, electrical behavior is coupled with lattice temperature, yet the scattering events between the charge carriers and lattice are not computed. However, in the hydrodynamic method, interplays between the charge carriers are accounted, and it has been asserted that devices with confined

active layer should be modelled with hydrodynamic method instead of thermodynamic method [106].

In this study electrical simulation for AlGaN/GaN HEMT is conducted by using Sentaurus TCAD by Synopsys. It is a package program and AlGaN/GaN studies were carried out by using this software previously [32,40,54,90]. This package program offers drift-diffusion, thermodynamic, hydrodynamic, and full band Monte Carlo simulations for semiconductor devices [106]. As the localized heat generation occurs in very small regions in the AlGaN/GaN HEMTs, the detailed device structure in Figure 3.5 (b) is solved by hydrodynamic model. Before temperature and carrier scattering correlations in the hydrodynamic model, electrostatic potential and continuity equations must be incorporated into the model. From the Poisson equation electrostatic potential can be calculated as in Equation 3.1 [106]:

$$\frac{\nabla \cdot (\varepsilon . \nabla \emptyset) + \rho_{trap}}{q} = (N_A - N_D + n - p) \tag{3.1}$$

Here, $\emptyset$ refers to electric potential, q is electronic charge, n and p stand for electron and hole densities in the domain, ρ_{trap} is charge density including trap and fixed charge information. Lastly, N represents the concentration and subscripts D and A implies ionized donors and acceptors, respectively.

Along with the electrons, holes are responsible for electrical conductivity in the semiconductor domain also, therefore, electron and hole continuity equations are included in the model together as [106]:

$$\nabla \cdot \overrightarrow{J_n} = q \left(R_{net,n} + \frac{\partial n}{\partial t} \right) \tag{3.2}$$

$$\nabla \cdot \overrightarrow{J_p} = -q \left(R_{\text{net},p} + \frac{\partial p}{\partial t} \right) \tag{3.3}$$

where $\vec{J}$ represents the current density of electron and holes, R_{net} is net recombination rate for electron and holes.

In the hydrodynamic model, current densities for electron and holes not only includes carrier potentials but also carrier concentration, carrier temperature, mass distribution in the domain, thus they are written as following:

$$\frac{\overrightarrow{J_n}}{\mu_n} = \left[n\nabla E_C + \lambda_n f_n^{td} kn\nabla T_n + kT_n\left(\nabla_n - n\nabla \ln \gamma_n - 1.5n\nabla \ln m_n\right)\right] \tag{3.4}$$

$$\frac{\overrightarrow{J_p}}{\mu_p} = \left[p\nabla E_V - \lambda_p f_p^{td} kp\nabla T_p + kT_p\left(-\nabla_p + p\nabla \ln \gamma_p + 1.5p\nabla \ln m_p\right)\right] \tag{3.5}$$

where E_C and E_V stand for energies of conduction band and valance band, respectively. Effective masses for electron and holes are defined with m_n and m_p. The γ and λ values are calculated depending on whether Fermi statistic or Boltzmann statistic is used for the model. f_n^{td} and f_p^{td} are thermal diffusion constants. Also, the electron and hole temperatures are written as T_n and T_p, respectively.

In the hydrodynamic model, after defining the Poisson and continuity equations, energy equations are solved for obtaining electron, hole, and lattice temperatures. Therefore, energy equations for these terms are incorporated into the model as [106]:

$$\frac{\partial W_n}{\partial t} + \nabla \cdot \overrightarrow{S_n} = \overrightarrow{J_n} \cdot \frac{\nabla E_C}{q} + \left.\frac{dW_n}{dt}\right|_{coll} \tag{3.6}$$

$$\frac{\partial W_p}{\partial t} + \nabla \cdot \overrightarrow{S_p} = \overrightarrow{J_p} \cdot \frac{\nabla E_V}{q} + \left.\frac{dW_p}{dt}\right|_{coll} \tag{3.7}$$

$$\frac{\partial W_L}{\partial t} + \nabla \cdot \overrightarrow{S_L} = \left.\frac{dW_L}{dt}\right|_{coll} \tag{3.8}$$

In these energy equations, W represents energy densities for electrons, holes and lattice with subscripts n, p, and L, respectively. Also, energy flux values are incorporated with $\vec{S_L}$, $\vec{S_p}$, and $\vec{S_n}$ values. And these values are written as:

$$\overrightarrow{S_n} = -\left(\frac{2.5 r_n \lambda_n k T_n}{q}\overrightarrow{J_n} + 2.5 r_n \lambda_n f_n^{hf} \hat{\mathrm{K}}_n \nabla T_n\right) \tag{3.9}$$

$$\overrightarrow{S_p} = \left(\frac{2.5 r_p \lambda_p k T_p}{q}\overrightarrow{J_p} - 2.5 r_p \lambda_p f_p^{hf} \hat{\mathrm{K}}_p \nabla T_p\right) \tag{3.10}$$

$$\vec{S_L} = -\hat{\mathrm{K}}_L \nabla T_L \tag{3.11}$$

In the flux equations, $\hat{\mathrm{K}}_n$, $\hat{\mathrm{K}}_p$, and $\hat{\mathrm{K}}_L$ are thermal conductivity for electrons, holes, and lattice, respectively. The r and f values are parameters to change physical results of the model by increasing influence of either convective or diffusive transports, and these values are set to 0.6 and 1 by default for r and f, respectively.

Moreover, collision terms of the energy equations represent scattering events for electrons, holes, and lattice. In the lattice, scattering events are written as following [106]:

$$\left.\frac{\partial W_L}{\partial t}\right|_{coll} = G_L + \epsilon_n \frac{W_n - W_{n0}}{\tau_n} + \epsilon_p \frac{W_p - W_{p0}}{\tau_p} \tag{3.12}$$

In this equation, equilibrium energy densities are defined by W_{n0} and W_{p0} for electrons and holes. Also, it is assumed that scattering events occurs in a time span which is defined by τ_n and τ_p for electrons and holes. Finally, the energy rise in the lattice as a result of generation and recombination events is given by G_L.

The single finger of the AlGaN/GaN HEMT shown in Figure 3.5 (b) is simulated by the Sentaurus TCAD using hydrodynamic model, and the electrical behavior of

the device and the heat generation in the domain are determined. The source and drain lengths in the single finger model are modelled as L_D=L_S =1 µm to reduce mesh size since it was reported that length of these metal contacts does not affect the electrical behavior of the device [107]. The boundary conditions for the solution of the hydrodynamic model are defined as following: The source and the drain contacts are defined as ohmic contacts with the resistance of R_S=R_D = 4 Ω. Also, the gate contact is a Schottky barrier which is a potential barrier and it has been defined in the model with ϕ = 1.48 eV barrier height [108]. In order to calculate temperature distribution in the domain, thermal boundary condition for the bottom layer of the GaN buffer layer is defined as 300 K, and the rest of the domain is set to adiabatic. To account for realistic model, trap density in the GaN layer is defined as N_{trap}= 3×10^{18} cm^{-3} and its cross section is set to σ_{trap}= 1×10^{-15} cm^{-2} [109]. The charge concentration at the AlGaN/GaN interface is calculated by using the definition from the study [110]. Consequently, the charge concentration is calculated 1.56×10^{13} C/µm. Finally, electron saturation velocity is defined 1×10^{7} cm/s, and the electron mobility within the GaN layer is calculated by Equation 3.13 [32]:

$$\mu = 1375 \left(\frac{T}{T_b} \right) \text{(W/mK)} \tag{3.13}$$

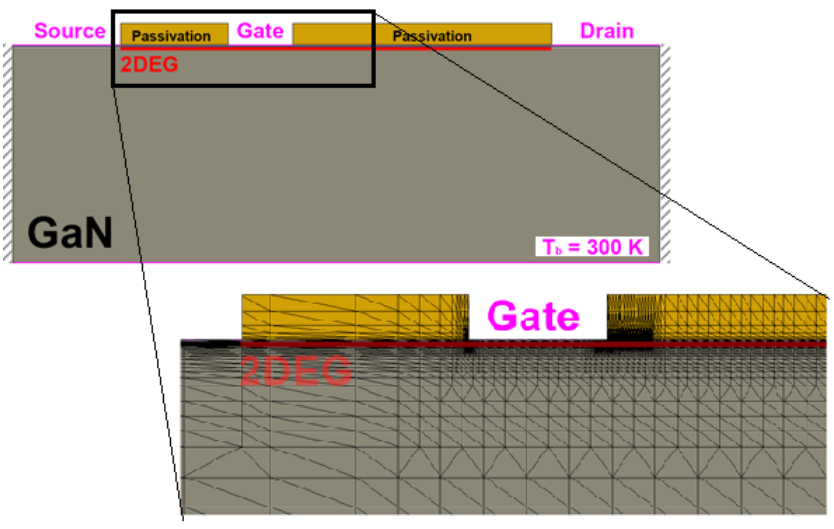


Figure 3.7. Device model for electrical simulation.

The Sentaurus device model is shown in Figure 3.7. In this model, more than 250,000 grid elements are used for spatial discretization and as it is shown in Figure 3.7, grid distribution becomes finer around the channel, especially drain side of the gate in order to capture the uninform peak electric field and resulting heat generation distribution. Since direct current operating condition is common application for device reliability investigations, in this study electrical model is simulated with the same condition. Although AlGaN/GaN HEMTs are generally operated for radio frequency applications, it has been reported that if the operating voltage is lower than 50 V, direct current simulations can estimate RF operating temperatures with small error [59]. The self-heating investigation for the device is conducted for two power conditions P = 1 W/mm and 2 W/mm. Also, to see biasing effects on the heat generation distribution, the device is simulated with the gate voltages of V_G = 0 V and V_G = -2 V. The I-V curve from the electrical simulation results are given in Figure 3.8. The I-V curve is same for both field plated and without field plated devices since the operation condition is selected as direct current [111]. When the V_G= -2 V, voltage between the drain and source contacts are increased to 6.5 V and 12.7 V to reach the 1 W/mm and 2 W/mm, respectively. For the open channel condition (V_G = 0 V) the drain voltage is raised to 2 V and 3.2 V, respectively. The heat generation data obtained from these

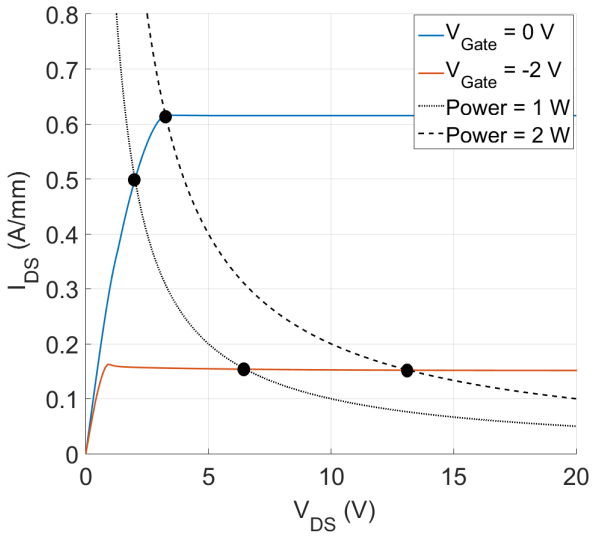


Figure 3.8. I-V curve for the modeled device.

simulations are given in the results.

3.2.2. Thermal Models

3.2.2.1. Continuum Scale Thermal Model. Although the lattice temperature from the electrical model is calculated by the electron, hole and lattice interactions, the electrical model only includes single finger and the AlGaN/GaN section of the device. However, having multiple fingers affects temperature distribution in the domain, for instance the peak temperature is observed in the innermost finger. Also, the substrate and the package layers impact the heat dissipation as well. However, modelling this whole device by electrical simulation increases computation cost dramatically. Therefore, after obtaining the heat generation data for the 2DEG region from the electrical simulations, 3-D thermal model is built for modelling the actual device. More important, to solve the phonon BTE at the hotspot region, boundary conditions and the average thermal conductivity values are extracted in this 3-D model. The 3-D diffusive thermal model is constructed by using COMSOL Multiphysics program which solves diffusive heat transport equation with finite element method. The device model is shown in Figure 3.9. This model is created with two different geometries: One having gate field plate structure and the other without field plate.

The material of the metal contacts is defined gold and the thermal conductivity of these contacts are set to k_{Au}= 3.18 W/cmK [111]. Thermal conductivity of the AlGaN and GaN layers are set same with $k_{AlGaN,GaN}$=100$(T/300)^{-0.5}$ W/mK [32] since the conductivity difference is very small and the AlGaN layer is thin (20 nm). The SiC substrate layer is defined with k_{SiC}=395$(T/293)^{-1.29}$ W/mK [112]. Also, to represent the bonding between the substrate and the copper package, epoxy layer is defined between these layers with the thermal conductivity of k_{Epoxy}= 60 W/mK [32]. Cu package and the Si_3N_4 passivation layer are set with conductivity of k_{Cu}=401 W/mK and $k_{Si_3N_4}$=30 W/mK, respectively [32]. Another thermal property that should be accounted for in the model is the thermal boundary resistance between the GaN and the substrate layer. During fabrication and integration of materials impurities and

nucleation layers are created [113] which contribute to the thermal boundary resistance. Hence, the resistance between these layers are included in the model with TBR = 3.3×10^{-8} m^2K/W [87]. Since the quarter of the eight-finger device is modelled, left and front cross sections are defined as symmetry boundary conditions. Also, since the convective heat transfer is negligible, upper surface of the device is also set adiabatic. Finally, the rest is assumed to have constant temperature of 300 K. Implementation of the heat generation data as a volumetric heat generation in the 3-D model increases mesh requirement significantly. Since the heat generation profile occurs predominantly in the lateral directions, data is integrated along its thickness and implemented as a boundary flux constant along the z-axis at the AlGaN/GaN interface for each finger. These steps are analogous to heat flux data transition in Chapter 2. This approximation is accurate enough since the finite element model solves diffusive heat transport and examples can be found in the literature [32, 51, 54]. Finally, the model is discretized spatially with ∼9 million elements. It can be seen from Figure 3.9 that compared the substrate layer, finer mesh is introduced to AlGaN and GaN layers which is extremely fine around the drain side of the gate to capture ununiform heat generation and its inherent temperature distribution.

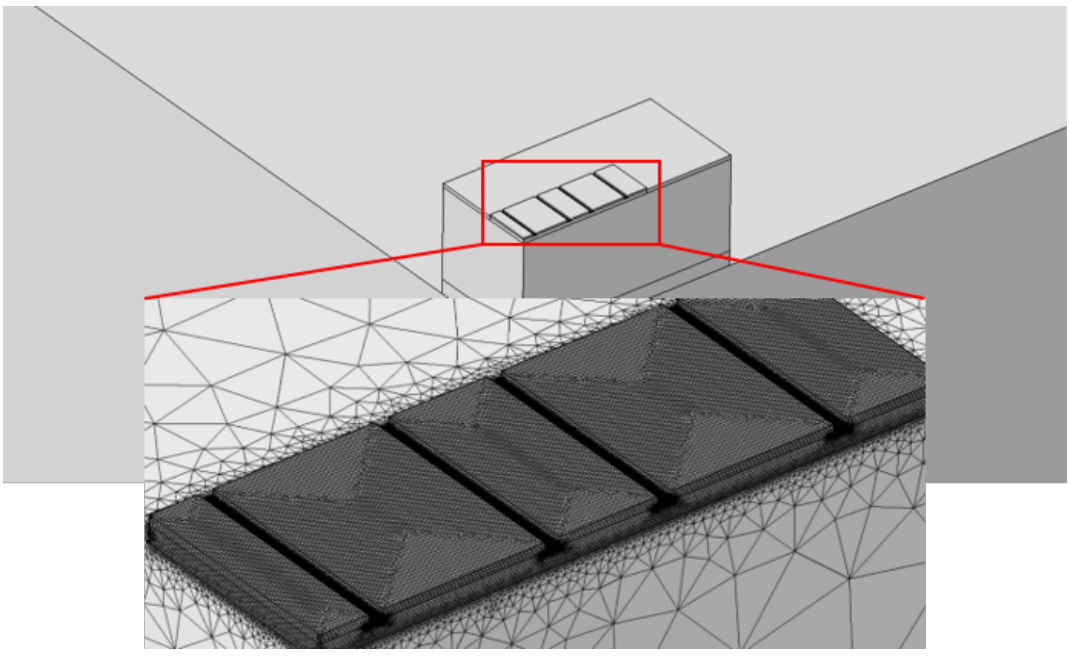


Figure 3.9. 3-D thermal model for diffusive device simulation.

The model is simulated by steady state assumption for all power and basing conditions. Each heat generation data from the electrical model is implemented in the gate field plated device and the device without field plate. Finally, boundary conditions and the average thermal conductivity for phonon BTE model are acquired by the 3-D continuum scale thermal simulations.

3.2.2.2. Sub-continuum Scale Thermal Model. Although the 3-D model accounts for different layers of the device, as shown in Chapter 2, continuum scale thermal analysis cannot estimate the peak temperature values stemming from the localized Joule heating. Nevertheless, solving the phonon BTE for the all device domain is unnecessary because the thermal transport in the far fields takes place diffusely, given that the size effects spawn near the localized hot-spot only. Therefore, to determine the size effects by solving the phonon BTE, the most active domain in the innermost finger is modelled solely. The horizontal length (L) and the vertical length (H) of the simulated 2-D domain should be selected carefully. The lengths of the domain should be long enough

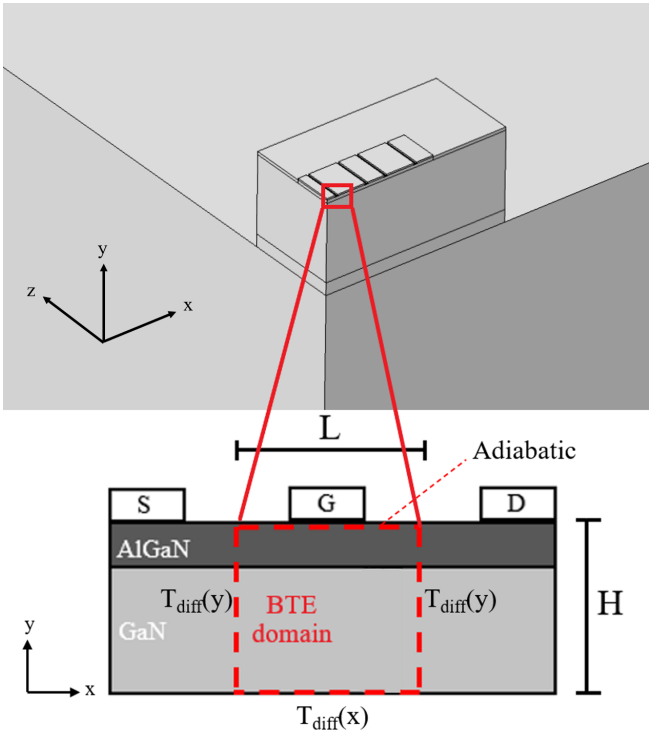


Figure 3.10. Sub-continuum model for the device.

to allow phonons propagate diffusely since the boundary conditions are extracted from the diffusive simulations. Hence, if the size of the domain is adequate for allowing diffusive transport away from the localized heat generation, boundary conditions for the selected region can be implemented in the phonon BTE calculations.

The sub-continuum domain is given by Figure 3.10. In this domain, the AlGaN layer is modelled as GaN due to its thickness. In order to implement the diffusive boundary conditions in this domain, horizontal length is selected as $L = 6$ µm and the vertical length is set to $H = 5$ µm to cover the all GaN buffer layer. The boundary conditions for the vertical walls $T_{diff}(y)$ are obtained from the COMSOL model as a function of the y-axis, similarly, for the bottom boundary diffusive temperature values $T_{diff}(x)$ are set as a function of x-axis. The upper surface of the domain is defined as a diffusive reflective boundary. Finally, the volumetric heat generation data from the electrical simulations are implemented in the domain.

The solution for the phonon BTE method is same as in Chapter 2. For the gray approximation, the mean free path of the phonons is defined as 400 nm. However, since the thermal conductivity of the GaN is defined as temperature dependent in the 3-D diffusive simulations, the thermal conductivity in the sub-continuum approach is acquired from the COMSOL model in a way that the average thermal conductivity within the BTE domain in the 3-D diffusive model is extracted. Finally, the domain is discretized with 300,000 nodal points (600×500), and the S_6 quadratures is selected for angular discretization.

3.3. Results

The heat generation profiles from the electrical simulations are given in Figure 3.11. It can be seen that the localized heat generation occurs at the AlGaN/GaN interface and it is localized at the drain side of the gate. Also, contrary to Chapter 2, the heat generation profile is not uniform. Although the lengths of the horizontal and vertical dimensions of the generation area change with the operation conditions, the

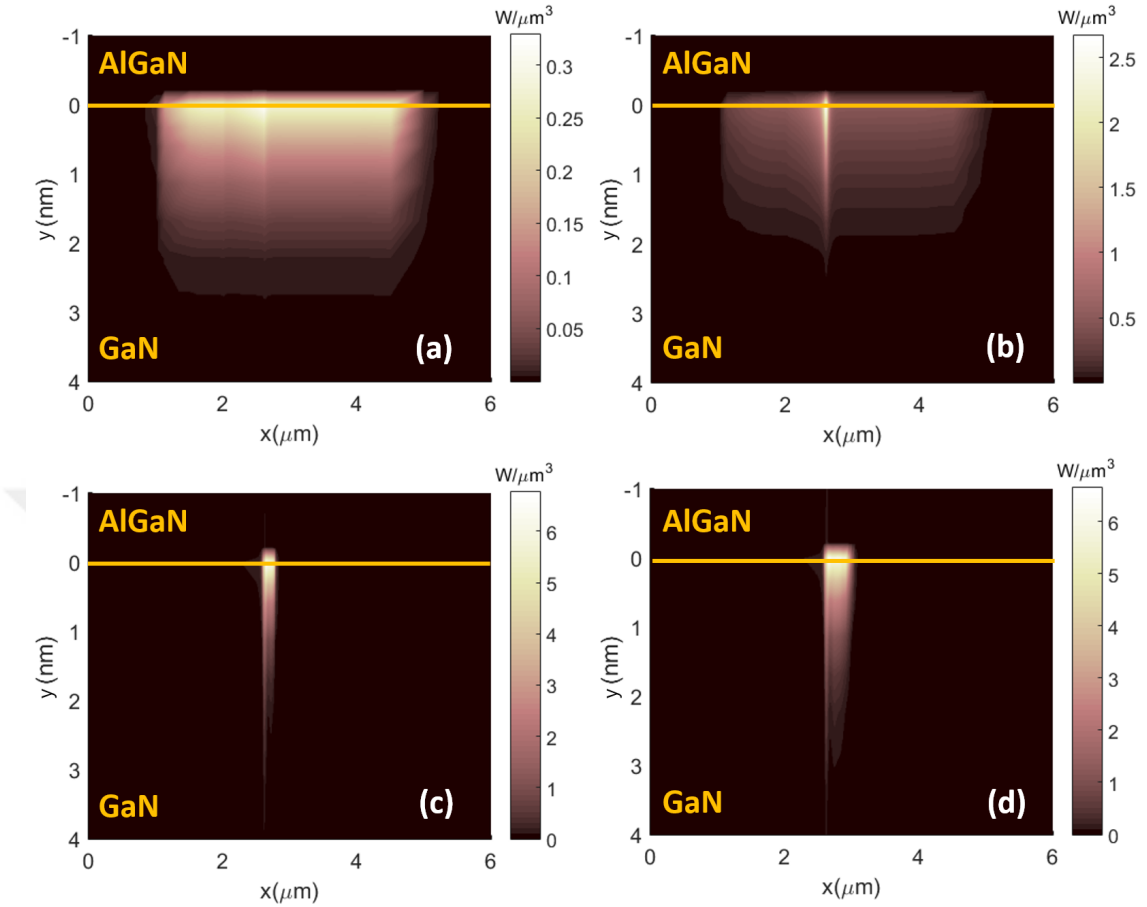


Figure 3.11. Heat generation distribution when device operates at (a) V_G=0, P= 1 W/mm, (b) V_G=0, P= 2 W/mm, (c) V_G=-2 V, P= 1 W/mm, (d) V_G=-2 V, P= 2 W/mm.

volumetric generation value is more intense around the AlGaN/GaN interface and the drain side of the gate which is located at the coordinate of (x=2.4 μm, y= 0 μm) in these figures.

When the device is operated with the open channel condition (V_G = 0 V) for the both power conditions, localized heat generation spreads to virtually entire channel horizontally (Figure 3.11 (a) and (b)). The reason is that in the open channel condition, electron movement is not confined by a steep electric field in the 2DEG region. However, for the open channel condition, the power increase leads to significantly higher volumetric generation around the gate edge, yet the profile remains almost the

same. In terms of the aspect ratio and the area size of the heat generation profiles, it is not possible the calculate exact values as in Chapter 2 since the Joule heating profile is not uniform in the generation area. However, as far as the occupied area by the generation in the domain is concerned approximately, it can be said that for the V_G = 0 V and P = 1 W/mm case, horizontal length of the generation area is slightly higher than 4 µm and the vertical length is ∼3 nm. For the same gate voltage but with higher power (2 W/mm), horizontal length becomes ∼4 µm, and the vertical length is ∼2.5 nm. Thus, regarding the open channel condition, the area size and the aspect ratio of the heat generation are ∼0.01 µm^2 and ∼1400 for both power conditions.

In the partially pinched off condition (V_G= -2 V), the heat generation profile changes significantly compared to the open channel condition, which is shown by Figure 3.11 (c) and (d). By dint of the negative gate voltage and steep electric field, the horizontal length of the heat generation area decreases dramatically, thus localized heat generation occurs in a confined region around drain side of the gate in the 2DEG for both power conditions. When the power is increased, the peak heat generation does not change significantly, yet the size of the generation profile increases briefly along the horizontal axis with the peak generation value. Considering the area size and the aspect ratio of the generation profiles when the device is operated under the partially pinched condition, horizontal length of ∼600 nm and ∼4 nm vertical length are observable for the 1 W/mm condition, which correspond to ∼0.002 µm^2 and aspect ratio of ∼150. Along with the power increment, the horizontal length becomes ∼800 nm and the vertical length stays same, thus the approximate area and aspect ratio become ∼0.003 µm^2 and ∼200, respectively. Thus, compared to open channel condition, horizontal length of the generation profile and the area size reduce dramatically. However, it should be noted that the change of the vertical length of the Joule heating profile is not observable with these results. It can be seen that vertical length remains in the span of ∼3-4 nm, and the aspect ratios of the generation profiles calculated by the electrical simulation are higher than 1 in the all cases.

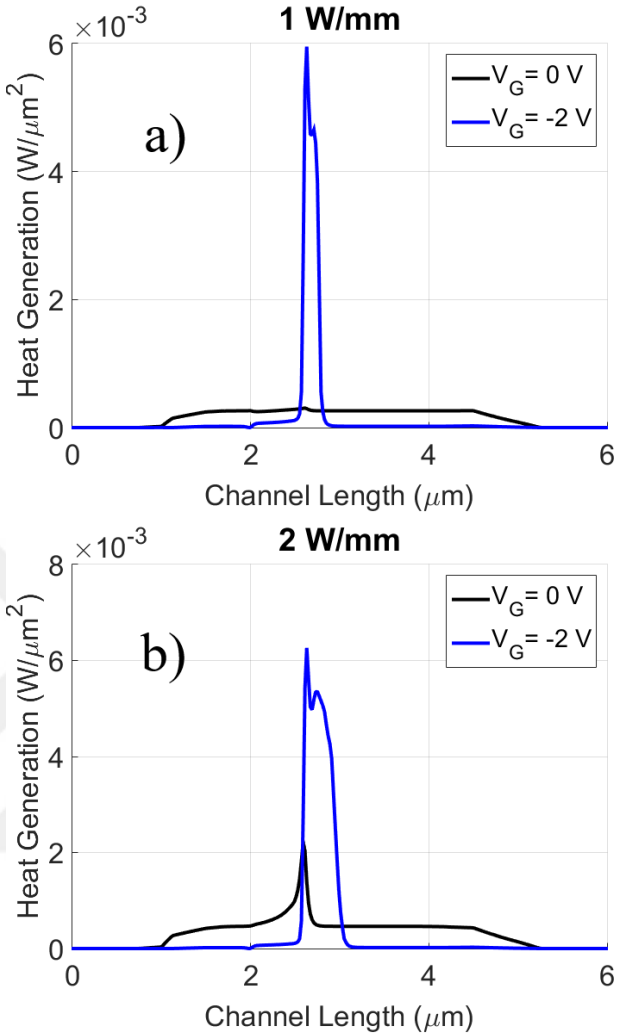


Figure 3.12. Integrated Joule heating data of (a) P = 1 W/mm, (b) P = 2 W/mm.

To perform thermal calculations first the heat generation profiles are integrated along the horizontal axis to be implemented as a boundary flux in the 3-D finite element method. The integrated heat generation data as a function of x are presented in Figure 3.12 for each case. The distinct generation profiles for the open channel and the partially pinched-off conditions are also observable from the heat flux data. Finite element thermal simulations are performed with the acquired heat flux data as boundary condition. The results of this simulation are later used to generate boundary conditions and averaged thermal conductivity values required for sub-continuum simulations. Finally, sub-continuum simulations are performed using the phonon BTE model to understand the thermal size effects of AlGaN/GaN HEMTs.

The temperature distributions along the 2DEG region of the device is given by Figure 3.13. The probe line for the temperature plots is selected on the AlGaN/GaN interface at which the peak temperature values occur. For the all cases, continuum and the sub-continuum results are presented together along the channel to mark the size effects resulting from the volumetric heat generation. It can be seen that for all cases away from the hot-spot region, continuum and the sub-continuum results overlap because phonons propagate without localized generation or boundary interference. However, discrepancy between the two method increases around the localized heat generation considerably compared the other parts in the device.

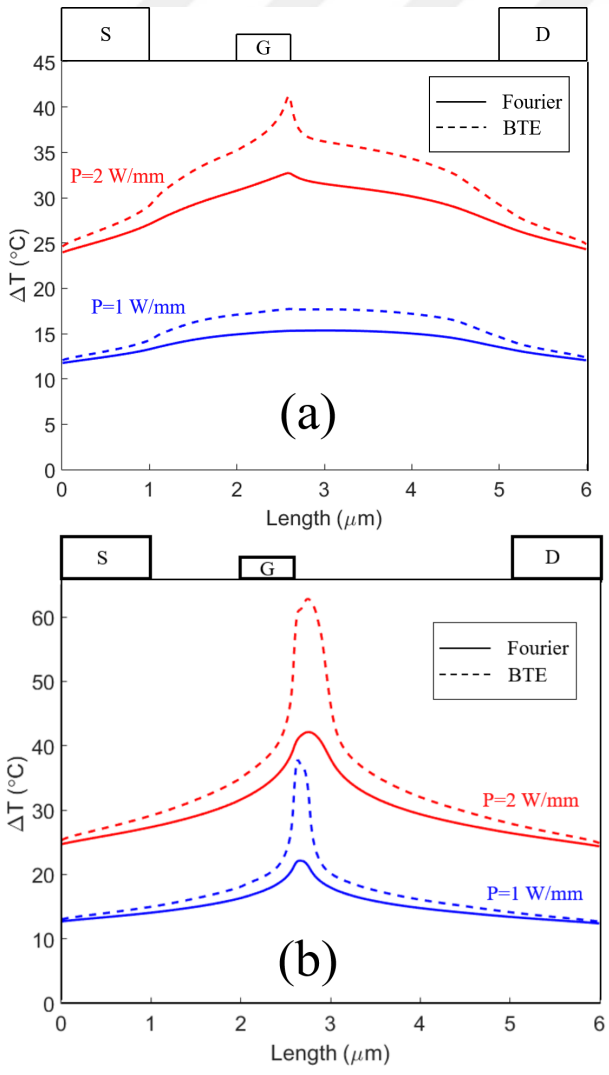


Figure 3.13. Temperature distribution in the device channel when the device operates with (a) V_G= 0 V, (b) V_G = - 2 V.

The temperature distribution in the device operating with the open channel condition is shown by Figure 3.13 (a). The temperature values are given in terms of temperature rise (T-300 K). When the power input is low (1 W/mm), continuum and the sub-continuum methods calculate the maximum temperature rise with a slight difference. The phonon BTE calculates ∼2.3°C higher temperature rise than the Fourier method. Since the heat generation profile spread over the device channel in this case (Figure 3.13 (a)), the size effects are not pronounced. Yet, the small discrepancy stems from the nonuniform profile of the Joule heating area. When the power is increased to 2 W/mm, the difference between the two methods increases around the drain side of the gate as a result of the change in heat generation profile as seen in Figure 3.13 (b). Along with the power change, the diffusive and the phonon BTE estimations rise to ∼32°C and ∼41°C, respectively. Thus, the discrepancy due to the size effects increases to 8°C.

When the device is operated with V_G = -2 V and power of 1 W/mm, the phonon BTE method calculates dramatically higher temperature rise at the drain side of the channel compared the Fourier estimation. At the hotspot, diffusive method calculates maximum of ∼22°C temperature rise, whereas the phonon BTE yields ∼38°C. Thus, size effects contribute to ∼16°C higher peak temperature at the 2DEG region. By increasing the power input from 1 W/mm to 2 W/mm, the channel temperatures increase significantly. For instance, Fourier simulation results ∼42°C temperature rise, and the phonon BTE calculates ∼63°C for the maximum temperature within the device. Therefore, the discrepancy between the continuum and the sub-continuum method increases to ∼21°C. This shows that even for the same operation condition and device structure, the power input has a strong effect on thermal size effects. Also, there is not a linear relationship between the power and maximum temperature as in Chapter 2 due to temperature dependent thermal conductivity used in this chapter.

The discrepancy between the continuum and the sub-continuum method increases significantly for partially pinched-off condition when compared to open channel condition. This stems from the smaller Joule heating area size and the aspect ratio.

Although the Joule heating profiles are not uniform, the results agree with the previous comparative study in Chapter 2. When the negative gate voltage is applied, Joule heating occurs in a much more confined area and the aspect ratio of the profile decreases as well. This behavior leads to a higher temperature rise in the device channel even for the same power condition. Reduced size of the generation profile, size effects become profound and contribute to higher discrepancy between the continuum and the sub-continuum approaches.

Finally, to see the effectiveness of the boundary heat flux approximation in the AlGaN/GaN HEMT, the heat generation data are implemented in the domain as a heat flux boundary. The heat flux boundary functions are acquired by the integration of the volumetric heat data along the vertical axis of the domain with the same steps conducted in Chapter 2. The obtained distributions at the boundary are given in Figure 3.12. Thus, the maximum temperatures calculated by the implementation of the heat flux boundary are compared with the volumetric heat generation results. Errors are calculated using Equation 2.71 and are presented in Figure 3.14.

It can be seen that the heat flux boundary approximation calculates the maximum temperature with a low error when the device is operated with the open channel

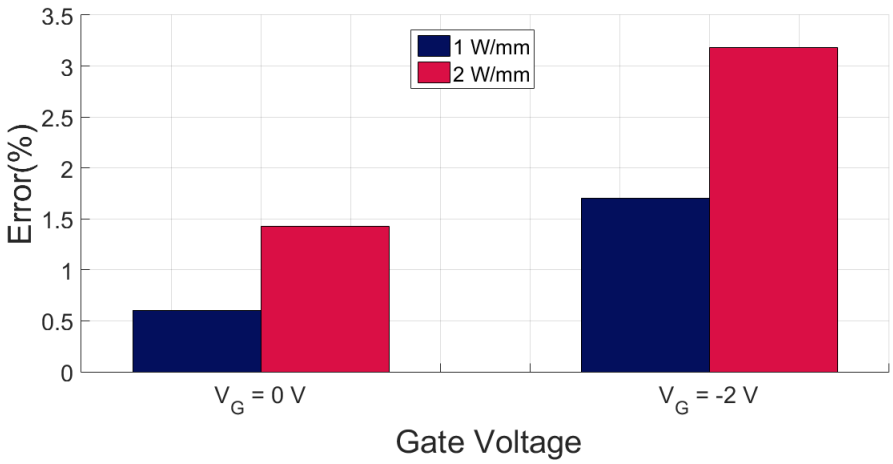


Figure 3.14. Difference between volumetric heat generation and the heat flux boundary approximations.

condition. For the 1 W/mm case, the error is 0.6%, and it rises to 1.4% with the 2 W/mm. Considering the relatively bigger generation area size (∼0.01 µm^2) and aspect ratio (>1000), the results agree well with the comparative study. Also, these errors correspond to ∼1.8°C and ∼4.7°C temperature rise difference. With the partially pinched-off condition, deviation between the two method increases slightly. This increase was anticipated since the overall area size of the generation profile drops to ∼0.002 µm^2. The errors of the heat flux approximation are 1.7% and 3.1% for the power 1 W/mm and 2 W/mm. These error values correspond to ∼5.6°C and ∼11°C difference in terms of the peak temperature. Again, the error of heat flux approximation with the partially pinched-off condition agrees well with Chapter 2, such that when the power is 1 W/mm, the error is close to ∼1.2% which is the maximum error when the area size is A (0.004 µm^2) with the same power at $a_r = 32$. The small difference can be attributed to the smaller generation area size in the partially pinched-off condition. Also, the heat flux boundary error with the V_G = -2 V and P = 2 W/ mm case is in the range of calculated deviations in the previous chapter. By and large, because of the confined heat generation region, the deviation of the boundary flux method increases with the negative gate voltage. Also, the power input affects the error. Results show that, the device with the open channel condition can be modelled by the boundary flux method with the error of ∼0.6-1.4%. Although the deviation increases, partially the pinched-off condition can be modelled with the 1.7-3.1% error. However, it should be noted that the power increase affects the errors as well.

4. COMPARISON OF THERMAL MODELS WITH EXPERIMENTS

In this chapter, imaging and thermal size effect detection capabilities of micro-Raman and thermoreflectance methods commonly used to measure the peak device temperature in AlGaN/GaN HEMTs are analyzed. First, virtual experiments are conducted using the electro-thermal model created in the previous chapter to discuss the expected performance of these experimental techniques. After the numerical investigation of these two experimental methods, actual thermoreflectance thermal imaging (TTI) experiments are conducted for thermal model validations by a collaborative study with Pennsylvania State University, Hongik University, and Sandia National Laboratories.

4.1. Virtual Experiment

4.1.1. Micro-Raman

Micro-Raman thermometry method is based on the Raman scattering premise. If a light is irradiated on a material, photons undergo scattering and leave the molecule with two outcomes: The light is scattered elastically with same energy which is called Rayleigh Scattering. However, after interactions with molecules, their energy may change that is called Raman Scattering. If the scattered photons leave with a higher energy, it is called anti-stokes and the reverse is called stokes. Therefore, these scattered photons convey information about the molecule, and the change of the properties of the light can be evaluated to interpret information about the material. The change between the light source and the scattered photons is called Raman shift and is expressed as in Equation 4.1:

$$\text{Raman Shift } \left(\text{cm}^{-1}\right) = \frac{1}{\lambda_{\text{Source}}} - \frac{1}{\lambda_{\text{Scattered}}} \tag{4.1}$$

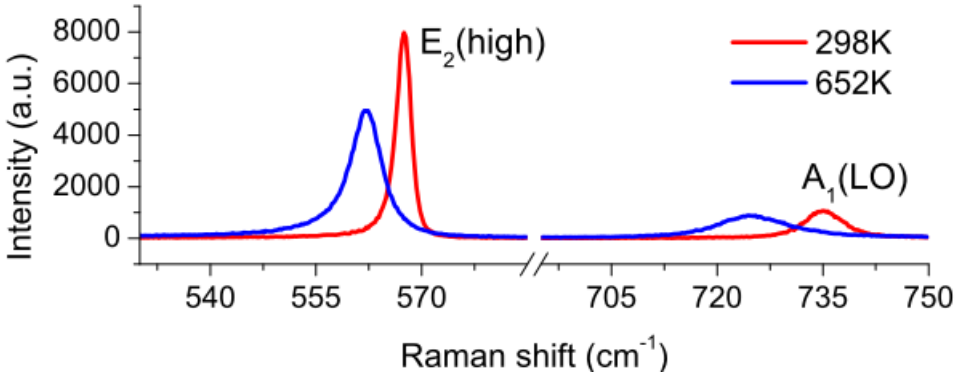


Figure 4.1. Raman shift with the temperature change in GaN [116].

where λ_{Source}, and $\lambda_{\text{Scattered}}$ are wavelengths of the incident and the scattered lights.

Since the molecular vibrations are also responsible for the Raman shift, investigation of the phonon modes in accordance with the temperature enables temperature mapping of the subjected domain. Therefore, temperature measurements with the micro-Raman thermometry conducted widely for semiconductor temperature characterization [78, 114]. Also, it is an optical non-contact method, thus eliminates the drawbacks of the other measurement methods. Depending on the experimental setup and the light source, $\sim$ 1 µm spatial resolution is possible with the current technological developments [78]. Furthermore, with the $\sim$10 ns temporal resolution [115], device thermal characterization can be carried out by both steady and transient conditions.

The Raman shift in GaN as a result of the temperature change is shown by Figure 4.1. The Raman scattering in the GaN medium is observable with the optical phonon modes E2 and A1 as shown in Figure 4.1. It has been reported that when the source laser has a wavelength of 532 nm, Raman shift of the E2 and A1 are reported 568 (cm^{-1}) and 734 (cm^{-1}), respectively [116]. It can be seen that when the temperature increases, Raman spectrum of the GaN changes as well, such that the linewidth of the Raman signals become wider. Therefore, by knowing the relationship between the Raman shift and the corresponding temperature, device temperature rise can be acquired. This can be done by investigating the E2 and the A1 phonon modes separately or simultaneously. The Raman shift of a single peak could give information

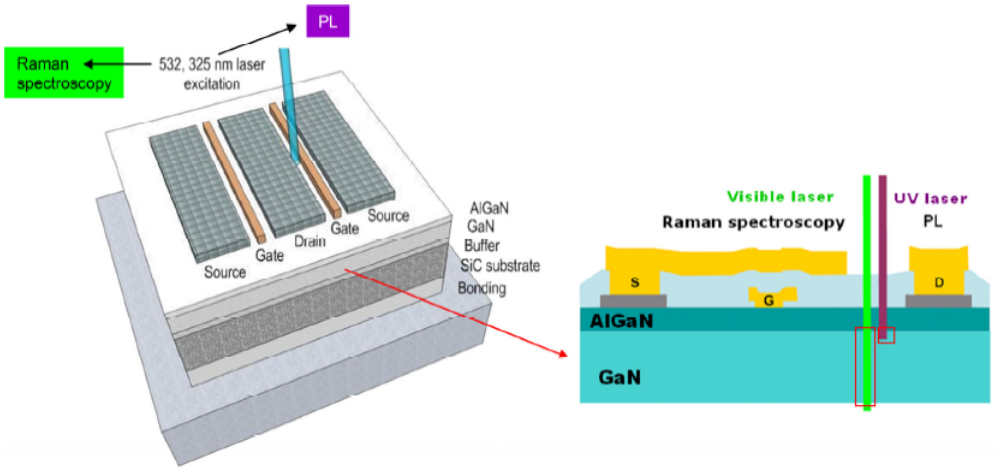


Figure 4.2. Micro-Raman probe region [116].

about device temperature, yet it has been asserted that 1-peak method is susceptible for stress distortion [115]. Another way is the 2-peak method in which the change of the both peak signals (E2 and A1) are assessed to interpret temperature values [114, 115]. Moreover, in the 2-peak method, the temperature rise can be modelled without influence of stresses.

The micro-Raman experiment and the probe region are shown in Figure 4.2. It can be seen that the light penetrates through the GaN layer if the laser is in the visible spectrum. Therefore, the acquired temperature values with the visible laser micro-Raman experiments, in fact, yield the average temperature values within the GaN layer. Moreover, the laser cannot pass through metal contacts. Since the hot-spot occurs under the drain side of the gate, it is not possible to measure hot-spot directly. Also, the use of field plate technology shifts the probe region more. The laser penetration in the GaN layer can be coped with the use of ultraviolet source. As it is shown in Figure 4.2, by using an excitation source with a smaller wavelength, the penetration depth can be confined around the 2 DEG region. However, the use of a laser with a smaller wavelength increases the photon energy inevitably, therefore it may contribute to electron-hole pairs within the probe region of the Raman thermography. This affects electrical behavior of the operating device and the temperature as well [90].

As a result, the accuracy of the micro-Raman method is still questionable and should be investigated.

4.1.2. Thermoreflectance Thermal Imaging

Thermoreflectance thermal imaging (TTI) is another optical method for obtaining operating temperature of devices. Although the thermoreflectance principles have been utilized for understanding the material properties for the past 60 years [83], with the improvements in the optical technology, especially with the charge coupled device (CCD) camera, CCD-based TTI method can be used for high resolution thermal mapping. By using this technique, each captured pixel from the camera can be evaluated for the temperature change at the device surface. It is possible to acquire ∼250 nm spatial resolution and sub-microsecond temporal resolution [117]. Moreover, temperature resolution smaller than ∼0.1°C can be attained by the CCD-based TTI [83].

The functionality of the thermoreflectance method relies upon the relation between material reflectivity and temperature. Since the reflectivity of any medium is a function of temperature, it is possible to track temperature rise by assessing reflectivity change. The basic scheme of the temperature-reflectivity interplay is shown in Figure 4.3. This relation is written as following [83, 118]:

$$\frac{\Delta R}{R} = \left(\frac{1}{R}\frac{\partial R}{\partial T}\right)\Delta T = C_{th}\Delta T \tag{4.2}$$

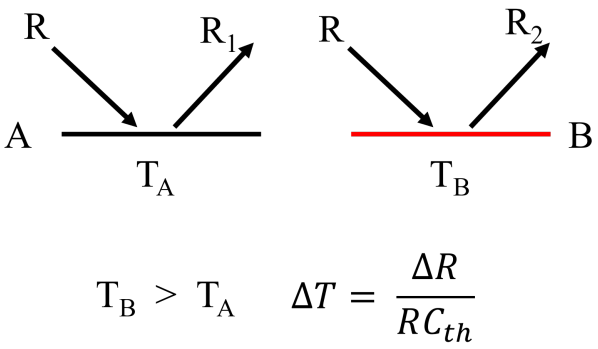


Figure 4.3. Thermoreflectance.

where R is reflectivity of the material, T is temperature, and C_{th} is the thermoreflectance coefficient.

In the TTI method, the selection of the thermoreflectance coefficient is crucial since it determines the reflectivity-temperature relation, hence, the accuracy of the measurement. The thermoreflectance constant is influenced by various factors such as wavelength of the source light, temperature of the material, material properties of the surface, and numerical aperture of the experimental setup. However, the illumination wavelength influences the correct thermoreflectance coefficient significantly, thus the wavelength of the source light and the material type are pillar for the coefficient selection [83, 118, 119].

Moreover, the spatial resolution of the TTI experiment is based on the diffraction limit and is written as following when the medium is air [118]:

$$d = \frac{\lambda}{2NA} \tag{4.3}$$

where d represents the spatial resolution, λ is the wavelength of the source light, and the NA is optical term that indicates the numerical aperture of the lens which defines the allowable set of angles for light to propagate in the lens.

The standard CCD-based TTI experiment scheme is given by Figure 4.4. It is seen that to investigate temperature, the device surface is illuminated by a visible LED light source. Also, by using the lens, the light source is focused on a small domain in accordance with the spatial resolution. The intensity of the reflected light is captured by the CCD camera. Finally, the temperature rise of the focused surface can be acquired by evaluating the intensity change of the light.

Despite the high resolution of this method, only the temperature values from the metal surfaces can be acquired via visible TTI. Thus, the accuracy of this method is questionable for finding the actual peak temperature in the layered devices such as

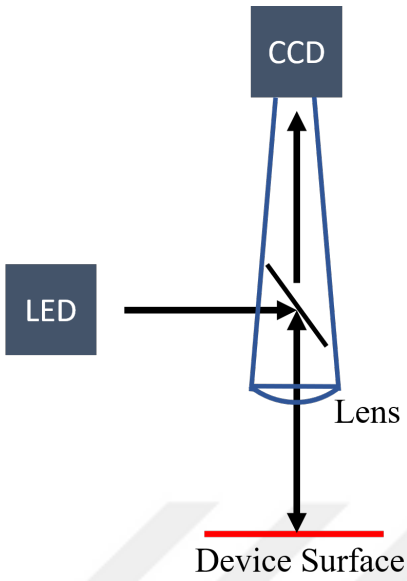


Figure 4.4. CCD-based TTI setup.

AlGaN/GaN HEMTs. Since the localized hot-spot occurs near the highly conductive gate metal contact, one may assert that the investigation of the gate surface may reveal the peak temperature. However, the heat removal takes places towards the reverse direction in the device structures (towards substrate), and more importantly, as a result of the size effects, steep temperature gradient occurs between the hot-spot and the gate contact in the semiconductor medium in spite of the small distance.

In this chapter, the hotspot temperature mapping accuracy of the visible laser micro-Raman and TTI methods in AlGaN/GaN HEMTs is investigated numerically. To do this, the electro-thermal model build in Chapter 3 is used and virtual micro-Raman and TTI probe region is created to mimic experimental results. Thus, experimental deviations are investigated by not only the diffusive model but also accounting for the size effects in this study.

4.1.3. Model

In order to understand micro-Raman and TTI ability to capture the peak temperature values in the semiconductor devices, AlGaN/GaN experiments are modeled

numerically. The same electro-thermal model created in Chapter 3 is used for the virtual experiments. The results from the previous chapter are post-processed to obtain experimental results. However, to show geometrical constraints stemming from the device structure, additional simulations are carried out for the field plated AlGaN/GaN HEMT. The field plate effect on the experimental probe region is seen from the Figure 4.5. It can be seen that when there is a field plate on top of the gate contact, micro-Raman probe region is shifted depending on the horizontal length of the field plate structure since the Raman laser cannot pass through the metal surfaces. Hence, the distance between the averaged GaN layer and hotspot increases. However, Raman probe region can be adjacent to the gate metal contact in the devices without field plates, which may enable to capture the hotspot occurring drain side of the gate. Moreover, considering the TTI, the probe surface is not changed dramatically by the field plate. Since the field plate is a metal contact itself, gold in the modeled device, the probe region becomes the field plate surface.

The device electro-thermal model and the phonon BTE results are same with Chapter 3. In fact, for the device without field plate simulations were not conducted again, micro-Raman and the TTI results were extracted from the results by post-processing. To show the geometrical constraints, electro-thermal model is used for the

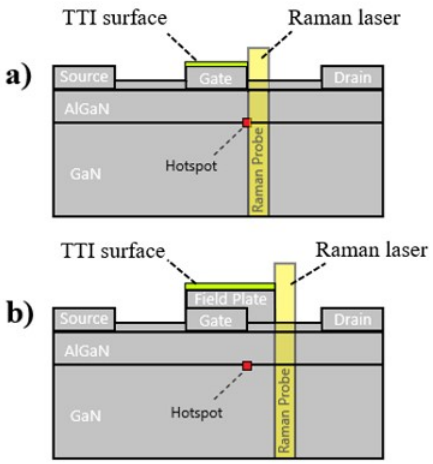


Figure 4.5. Micro-Raman and TTI probe regions in the (a) non-field plated and (b) field plated AlGaN/GaN HEMT.

field plated device in which the length of the field plate is set to L_{FP}=1000 nm. Virtual experiments are conducted only for the partially pinched-off conditions in order to see the worst-case scenario as a result of the confined localized heat generation. Finally, the experimental results from the field plated and without field plated AlGaN/GaN HEMTs are compared.

Figure 4.5 shows the virtual experiment locations in the electro-thermal model. So as to model the micro-Raman experiment, Raman probe region is created in the BTE domain as shown in Figure 4.5. The domain is placed adjacent to the drain side of the gate in the device without field plate and is shifted in the field plated device as in Figure 4.5(b). The length of the Raman probe region is set to 1 µm due to the resolution of the method. Finally, the average temperature value in the Raman probe area is extracted as a numerical micro-Raman temperature. On the other hand, the TTI method measures the metal surfaces, whereas the phonon BTE model does not include metal contacts. Thus, to obtain numerical TTI results, a diffusive 2-D model is crated for the metal contacts only (gate or field plate). As given in Figure 4.6, the temperature distribution adjacent to the gate metal contact is implemented as a boundary condition in the auxiliary domain and the rest is set to adiabatic. The auxiliary domain for TTI

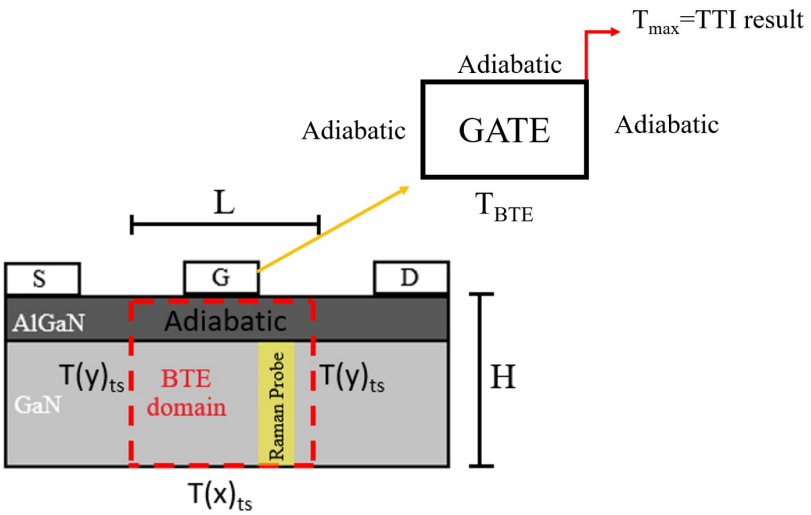


Figure 4.6. Location of the numerical micro-Raman and TTI experiment results in the electro-thermal model coupled with the phonon BTE.

is assumed fully diffusive since the material is highly conductive gold for both gate and field plate. Therefore, the maximum temperature at the gate or the field plate surface is acquired as a TTI result. It is assumed that the TTI method is able to capture the maximum temperature at the surface, given that the temperature distribution at the metal surface does not have a sharp gradient.

4.1.4. Results

The temperature distribution in the device channel is presented in Figure 4.7. Figure 4.7(b) and Figure 3.13 (b) are identical except the field plated device temperature profile simulated additionally in this chapter. For the field plated device, the temperature distribution changes slightly compared the device without field plate. When the power is 1 W/mm, the Fourier and the phonon BTE estimations for the peak temperature are ∼21.5°C and ∼35.5°C, respectively, which corresponds to discrepancy of ∼14°C due to the size effects in the field plated device. This difference is ∼16°C in the non-field plated device with the same power input. By increasing the power in the field plated device, the maximum temperature values become ∼41°C and ∼59°C with Fourier and phonon BTE, hence the discrepancy is ∼17.5°C which is calculated ∼21°C in the non-field plated device. Thus, results show that the field plated device yields ∼2°C and ∼3.5°C fewer temperature differences compared with the non-field plated device. This situation results from the field plate impact on the electric field and the generation profile. Also, along with the higher power, the effect of the field plate increases and leads to higher difference with the non-field plated device results. However, the field-plate effects in this study are limited as the passivation thickness is set to 200 nm. It has been reported that when the passivation thickness is bigger than 200 nm, field plate effects on the Joule heating decrease [32]. Yet, the slight temperature drops are still observable. Since one of the aims of this study is to see geometrical constraints on experimental accuracy, minimizing the field plate effects is favorable.

The virtual micro-Raman temperature deviations from the device peak temperature are shown in Figure 4.8. It is seen that the discrepancy between the peak and the

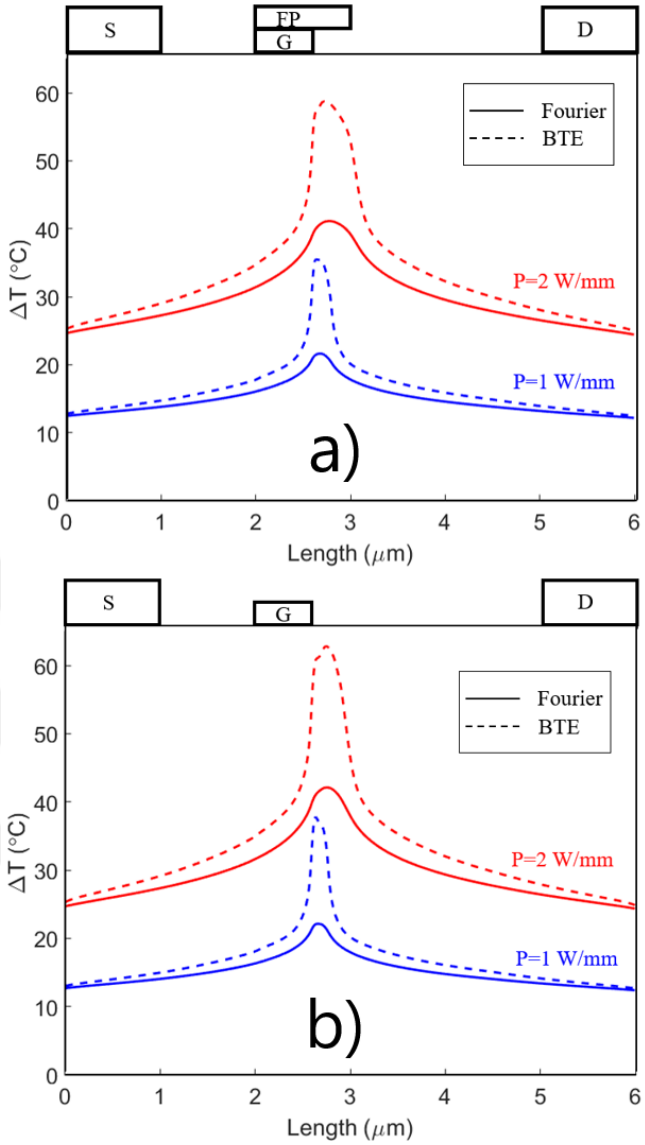


Figure 4.7. Temperature distribution in the 2DEG when the V_G = -2 V for (a) field plated and (b) non-field plated device.

virtual experiment temperatures varies depending on the field plate structure, power condition, and the simulation type. However, results show that the method is not able to capture the peak temperature values in the device active layer even if the phonon events are not accounted for. Considering the diffusive simulations, when the power is 1 W/mm, the discrepancy is ~8°C for both structures with a slight difference. When the power is increased, the discrepancy is almost doubled (~16°C) for both structures. As far as the phonon BTE results are concerned, the deviations increase significantly

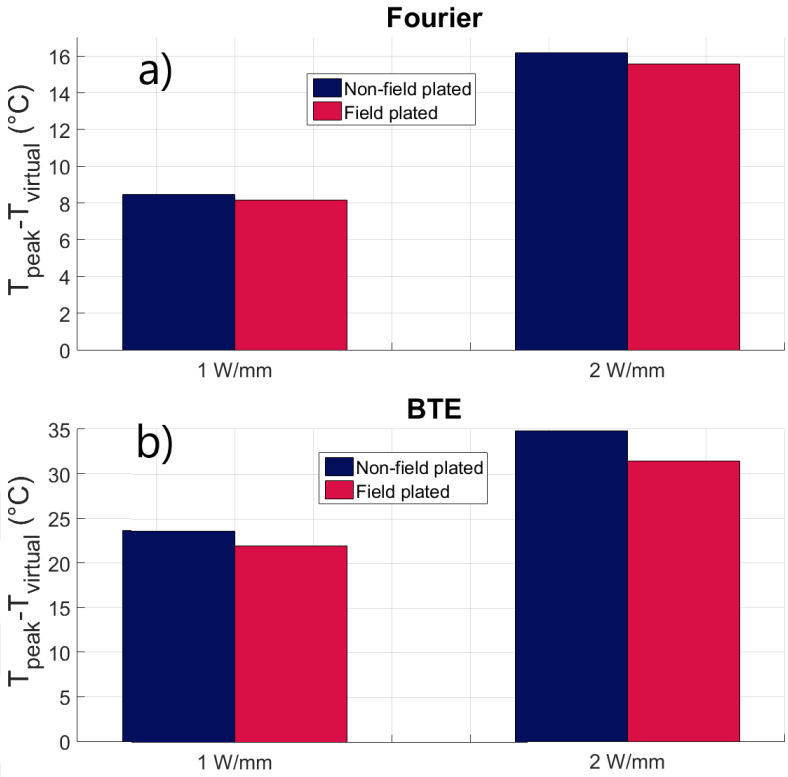


Figure 4.8. Micro-Raman deviation from the device peak temperature with (a) Fourier estimation and (b) phonon BTE estimation.

compared the Fourier case, which implies that the use of diffusive models for experimental validations may contribute to significant errors. It is seen that the deviation from the peak temperature, when the power is 1 W/mm, becomes ∼23.6°C and ∼22°C for the non-field plated and field plated devices, respectively. When the power is 2 W/mm, the discrepancies rise to ∼35°C and ∼31.5°C. Therefore, up to ∼35°C error can be obtained from the micro-Raman method when the phonon BTE is considered. Also, the deviation decreases to ∼22°C in the best case.

Regarding the micro-Raman results, non-field plated device yields higher difference from the peak temperature rise although the reverse was expected as a result of the probe region shift. The reasons are the depth averaging of the micro-Raman method and the field plate effects on the maximum temperature. The field plate structure drops the maximum temperature slightly as shown in Figure 4.8, yet the average temperature value in the Raman probe region changes insignificantly compared the peak temper-

ature change since the size of the hotspot is much smaller than the GaN thickness. Consequently, the difference between the peak and virtual temperature drops.

On the other hand, the virtual TTI experiment results are shown in Figure 4.9. In TTI, the deviation from the peak temperature changes with the power, structure, and the simulation type, similar to the micro-Raman method. This method also cannot measure the peak temperature rise within the device active layer. Nevertheless, TTI yields significantly small deviations compared to micro-Raman method. Regarding the diffusive simulations, the deviation from the peak temperature is ∼3°C for both field and non-field plated devices. Along with the higher power, the difference increases to ∼6°C in both device structures. However, the phonon BTE yields dramatically higher experimental discrepancies as a result of the localized heat generation and the size effects. When the power is 1 W/ mm, the deviation from the peak temperature rise to ∼15°C. At 2 W/mm, TTI discrepancies increase to ∼21°C and ∼19°C for the non-

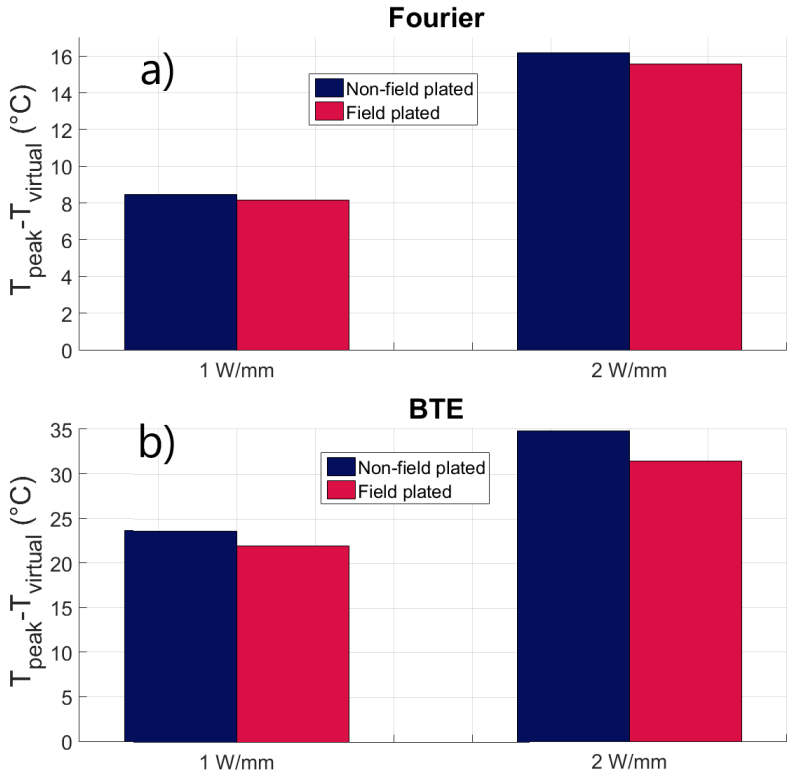


Figure 4.9. TTI deviation from the device peak temperature with (a) Fourier estimation and (b) phonon BTE estimation.

field plated and field plated devices, respectively. Therefore, the deviation between the peak and measured value can be as high as ∼21°C with the TTI method considering the worst case. Yet, the best case yields ∼3°C difference. Thus, it can be asserted that TTI provides much more accurate channel temperature information compared the micro-Raman method.

Moreover, the discrepancies are slightly higher in the non-field plated devices similar to the micro-Raman case. Again, this situation can be attributed to the field plate impacts on the peak temperature. The use of the field plate does not influence the surface temperature significantly which is ∼1.5°C for the all cases. Yet, relatively more temperature drop occurs at the localized heat generation region, which reduces the difference between the peak and the TTI estimation.

In conclusion, it is seen that both virtual experiments cannot estimate the peak temperature rise in the AlGaN/GaN device. Although deviations can be as small as ∼3°C and ∼8°C in the micro-Raman and the TTI, respectively, diffusive estimation underestimates the peak temperature and the experimental discrepancies. When the phonon BTE model is solved, the minimum discrepancies become ∼15°C and ∼22°C in the TTI and micro-Raman, respectively. Along with the power increment, the highest errors become ∼21°C and ∼35°C for TTI and micro-Raman. Despite the marked peak temperature increment, virtual values change slightly since the heat transport is not diffusive in the BTE model, which yields higher experimental errors in the BTE results. However, by comparing the two methods, the visible TTI is able to yield temperature rise closer to the peak. Furthermore, although negative effects were expected by dint of using the field plate structure, the reverse is observed. The field plate impact on the maximum temperature rise decreases the experimental discrepancy since the temperature values at the experimental probe regions are not affected using the field plate. Overall, the experimental error difference of the field plated and the non-field plated devices does not exceed ∼2°C. Also, experimental differences increase with the power input. The results imply that a numerical model accounting for the thermal size effects is needed for accurate device characterization, since experiments underestimate

the peak device temperatures.

4.2. Actual Experiments

As seen in the previous chapter, the virtual experiment results show that neither micro-Raman nor visible TTI experiments are able to determine the actual peak temperature in devices, especially when the operation condition is partially pinched-off. However, the validation of the numerical methods with the actual experiments is crucial, moreover, the sub-continuum thermal transport observation in an actual device with experiments was not reported previously. Thus, in this chapter, an actual AlGaN/GaN HEMT is investigated by using the electro-thermal model, the phonon BTE model and the TTI experiments. Also, the TTI experiments are carried out with two different light sources which are visible and UV sources. It should be noted that the work in this part of the study was carried out as a collaborative study with Pennsylvania State University, Hongik University, and Sandia National Laboratories. The experiments and part of the simulations were conducted by other contributors.

4.2.1. Device Structure and Continuum Model

The investigated AlGaN/GaN HEMT is shown in Figure 4.10 which has slightly different device layout compared to the device modeled in Chapter 3. Unlike the multifinger device modelled previously, the device investigated by experiments has only one finger. The device was fabricated by Sandia National Laboratories. The layout is shown in Figure 4.10(a) and the optical image from above the gate surface is given in Figure 4.10(b). The fabricated device has a symmetrical shape, and the length of the gate (L_G) is 2 µm, and the gaps between the gate and other metal contacts are same (L_{GD}=L_{GS} = 3 µm). Also, the gate has a width of 100 µm. The GaN buffer and the AlGaN layers have the thickness of 4.3 µm and 20 nm, respectively. GaN cap layer is introduced in order to enhance the electrical performance and the experimental accuracy which will be shown later in this section. For the substrate layer, silicon is used. The metal ohmic contacts were created by electron-beam evaporation, which have

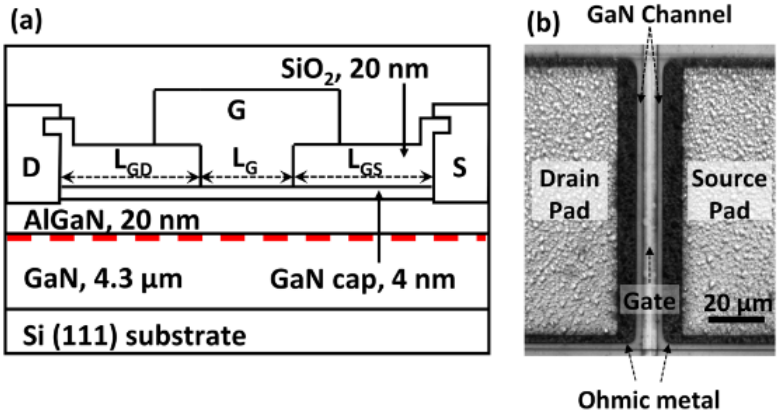


Figure 4.10. (a) 2-D scheme of the fabricated AlGaN/GaN HEMT. (b) Optical image of the device by CDD camera used in the TTI measurements.

Ti/Al/Ni/Au layers with 20 nm, 100 nm, 25 nm, and 50 nm thicknesses, respectively. Also, the gate is formed by Ni/Au Schottky contact which have thickness of 20 nm and 200 nm, respectively. Finally, the plasma enhanced chemical vapor deposition (PECVD) was used for forming 20 nm SiO_2 passivation layer.

To validate the TTI measurements, an electro-thermal model is needed. The steps for the electro-thermal model are same with the procedure fallowed in Chapter 3 and are given in Figure 3.6. Electrical simulations and the diffusive 3-D thermal simulations are done by Sentaurus TCAD and COMSOL Multiphysics software. Moreover, average thermal conductivity in the phonon BTE domain and the boundary conditions for the BTE solution are acquired from the diffusive model as well.

First, to get the Joule heating data, electrical simulations are conducted. To show the bias dependence of the device maximum temperature, the device is simulated with both partially pinched-off and open channel conditions. Therefore, the gate voltage of the device is set to -1 V, 0 V, and 2.5 V in the simulations. Also, two different power conditions (2.5 W/mm and 5 W/mm) are considered in the studies. The acquired I-V curve of the device is presented in Figure 4.11. In order to attain the desired power condition, the drain voltage is increased until the condition is met. For instance, to reach the power dissipation of 2.5 W/mm, in the partially pinched-off condition (V_G

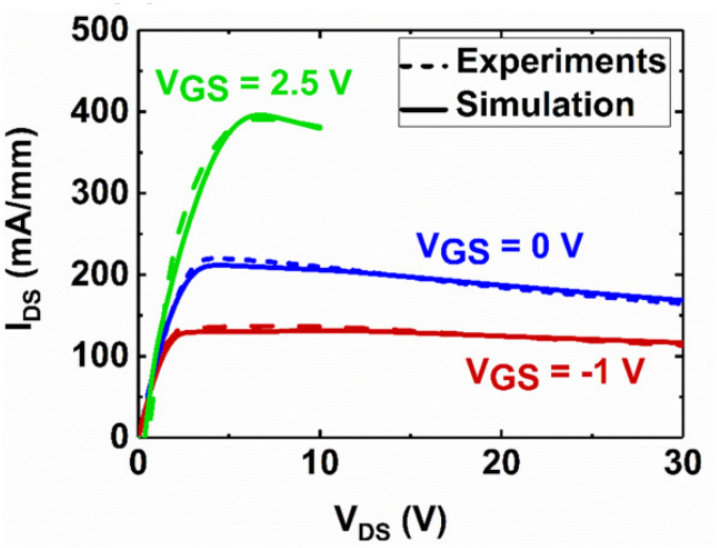


Figure 4.11. I-V curve of the device under DC operating conditions.

= -1 V) the drain voltage is increased to V_{DS}= 20.1 V. In the fully open channel operation (V_{GS}=2.5 V), the drain voltage is raised to 6.3 V as a result of the higher current. Also, electrical behavior of the fabricated device is measured by experiment, and results agree well with the electrical simulations as shown in Figure 4.11.

For the 3-D diffusive thermal model, the fallowed steps are identical to the electro-thermal model created in Chapter 3. Nevertheless, due to the different device structure, the model is defined with few different properties. The thermal conductivity of the AlGaN is set to 0.3 W/cmK and GaN is defined as following [57]:

$$k_{GaN} = 2.67 - 4.25 \times 10^{-3}T + 3 \times 10^{-6}T^2 \,(\mathrm{W/cmK}) \tag{4.4}$$

Moreover, thermal conductivity values for Si substrate, SiO_2 passivation and the metal contacts are set to k_{Si} = 1.5 W/cmK, k_{SiO_2}= 1.4 W/cmK, and k_{Au} = 3.17 W/cmK, respectively [90].

The environment temperature and the base temperature of the substrate layer are defined as 25°C since they are controlled at 25°C while the experiments are con-

ducted. Also, to represent the experimental environment better, it is assumed that all surfaces are subjected to natural convection with the convection coefficient of 5 W/m^{2}K [90]. The Joule heating data is implemented as a volumetric heat generation without computational burden since the device is not a multifinger device.

The Joule heating data from the electrical simulations and the diffusive thermal simulation results for the 2.5 W/mm case are shown in Figure 4.12. Regarding the heat generation distribution in the device, it is seen that the profile changes significantly depending on the biasing condition. When the channel is fully open, the Joule heating occurs through the entire channel. However, in the partially pinched-off condition, the Joule heating occurs in a much more confined region at the drain side of the gate. As a result of the self-heating, the temperature distribution at the device surface is shown in Figure 4.12 (d) and (e). The temperature contours represent the metal contact

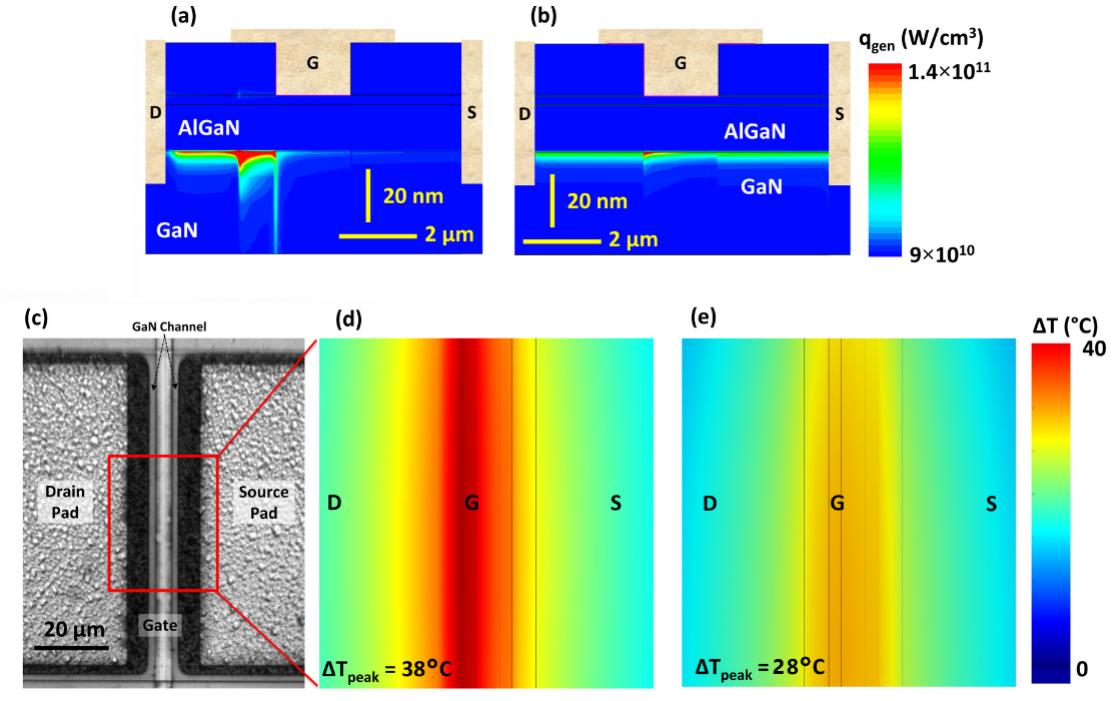


Figure 4.12. Electro-thermal simulation results for the V_G= -1 V and V_G= 2.5 V when the power is 2.5 W/mm. (a)-(b) Joule heating data for partially pinched-off and fully open channel conditions, respectively. (d)-(e) Surface temperature distributions for partially pinched-off and fully open channel, respectively.

surfaces of the device in the 3-D diffusive model and the corresponding region is shown on the real device in Figure 4.12(c). The reason of showing the surface distribution is to compare with the TTI results later in this study. However, it is seen that the biasing condition has a similar influence on the temperature distribution compared to the previously studied model in Chapter 3. When the device is simulated with the partially pinched-off condition, drain side of the gate becomes hotter compared to rest of the surface. Consequently, the peak temperature rise on the gate surface is measured ∼38°C. However, along with the gate voltage increment to 2.5 V, the temperature rise value on the surface decreases to ∼28°C.

It should be noted that the inevitable discrepancy between the gate surface temperature and the peak channel temperature is also seen in these models. For the partially pinched-off condition the peak channel temperature rise is calculated ∼44°C which is higher than the gate surface value by ∼6°C. Similarly, discrepancy of ∼7°C is calculated for the fully open channel condition.

4.2.2. Visible TTI Measurements

Before investigating of the sub-continuum thermal transport, standard visible TTI method is used for measuring the device surface temperature in order to compare with the UV TTI and phonon BTE results.

To acquire surface temperature distribution as a function of the reflectivity change on the metal surface, Microsanj NT-210A thermal imaging system was used, which has same working principle with the experimental setup shown in Figure 4.4. For assessing the change of the intensity of the reflected light, the thermal imaging system operates CCD camera which has 1626×1626 pixel resolution. For the illumination source, visible LED source was utilized that has wavelength of $\lambda = 530$ nm. Moreover, 50x objective lens was used in the thermal imaging system which has numerical aperture value of 0.45, so that 0.59 µm spatial resolution can be attained. Also, the thermoreflectance coefficient for the setup was determined as $2.5 \times 10^{-5} \pm 6.3 \times 10^{-6}°C^{-1}$. So as to

control the device at the quasi-steady state, constant gate voltage was applied. Also, the drain voltage is square with span of 80 µs and this process was reiterated with 800 µs intervals. Finally, for the duration of the measurements, LED pulse span was set to 5 µs.The visible TTI measurements were conducted for the partially pinched-off condition (V_G= -2 V) and the fully open channel condition (V_G = 2.5 V). For the both biasing conditions, the power was set to 2.5 W/mm and 5 W/mm. Also, as stated in the electro-thermal model, the base temperature of the substrate was maintained at 25°C.

The temperature distribution on the metal surfaces, when the power is 2.5 W/mm, are given by Figure 4.13. The results are similar to the electro-thermal simulation results in terms of the surface distribution. Same trends are observable with the TTI experiments, such that when the device operates with partially pinched-off condition,

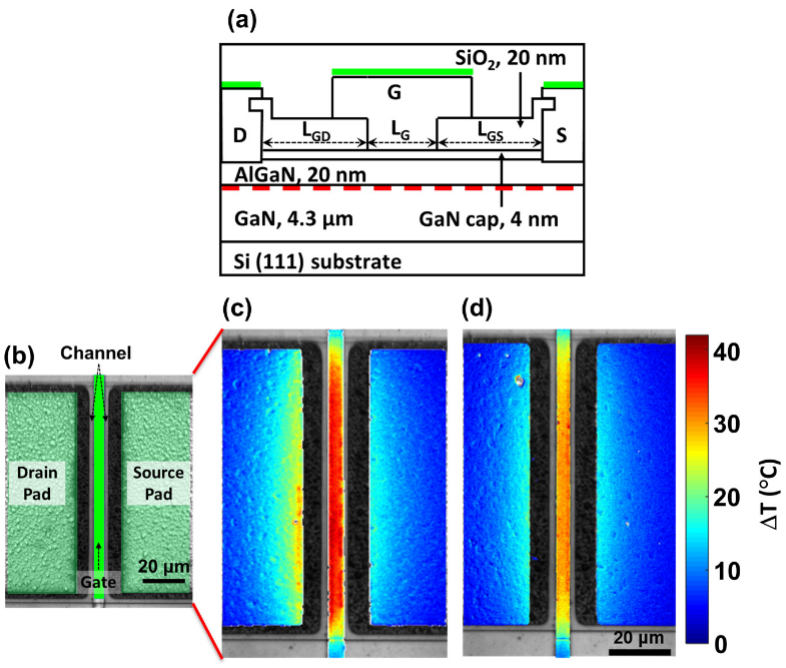


Figure 4.13. TTI results when the power is 2.5 W/mm (a)-(b) Illustration of the TTI probe regions. (c) TTI measurement of the device operated with the partially pinched-off (V_G = -1 V) condition. (d) Results for fully open channel condition (V_G = 2.5 V).

higher temperature values occur at the gate surface, particularly at the drain side of the surface. With the partially pinched-off condition (Figure 4.13(c)), the maximum temperature rise on the gate surface was observed 38 ± 0.96°C. Whereas, for the fully open channel condition, the maximum observable rise on the gate surface was 28 ± 0.71°C. Therefore, as far as the electro-thermal simulation results on the gate surface are considered, visible TTI results show excellent agreement, which is valid for the 5 W/mm case also. In fact, these results signify that visible TTI measurements cannot capture the peak device temperature within the device channel, given that ∼10°C more temperature rise is detected in the 2DEG region by the diffusive electro-thermal model. Furthermore, the actual peak temperature is anticipated to be higher than the calculated value by the diffusive method, especially in the partially pinched-off condition. Since the diffusive and phonon BTE models yield similar temperature rise away from the hot-spot, the size effects and the actual peak temperature cannot be estimated by the diffusive thermal model despite the agreement with the visible TTI on the gate surface. Consequently, sub-continuum effects should be investigated to understand real temperature distribution within the 2DEG region.

4.2.3. UV TTI Measurements

In order to obtain the temperature rise within the device channel, the light source is required to be in the UV spectrum as the penetration depth of a light is a function of the wavelength for a given material. However, a smaller wavelength means photons with higher energy. Thus, as explained previously, using the UV light source can bring about the photocurrent in an operating device, which affects the real temperature measurements since the electrical behavior of the device is altered. Nevertheless, the use of incoherent and low power pulsed illumination source can alleviate this problem. Moreover, the CCD cameras in the modern thermoreflectance imaging systems facilitate the operation of incoherent light source. Therefore, contrary to the UV micro-Raman measurement which uses coherent laser source with high photon density that creates photocurrent inevitably, the TTI technique enables the deployment of the pulsed incoherent low flux source which minimizes these effects. Also, the use of the GaN cap

layer alleviates this problem which will be explained later.

To see the absorption of the UV and visible light sources through the device layout, the electromagnetic solver in the COMSOL Multiphysics was utilized. As a result, the absorption of the both light sources are given in Figure 4.14. Considering Figure 4.14 (b) and (c), it can be seen that when the visible light is used, the absorption occurs through the whole GaN layer. However, when the wavelength is decreased to 365 nm, the light is absorbed predominantly in the near surface region (0-100 nm). Thus, the assessed intensity values by the CCD are acquired from the region near the channel in the UV TTI experiments instead of the gate surface. Also, it is seen that more than half of the light is absorbed in the 2 nm GaN cap layer. This indicates that the photocurrent impacts are eased by this layer profoundly since the cap layer is not subjected to a charge flow in device operation.

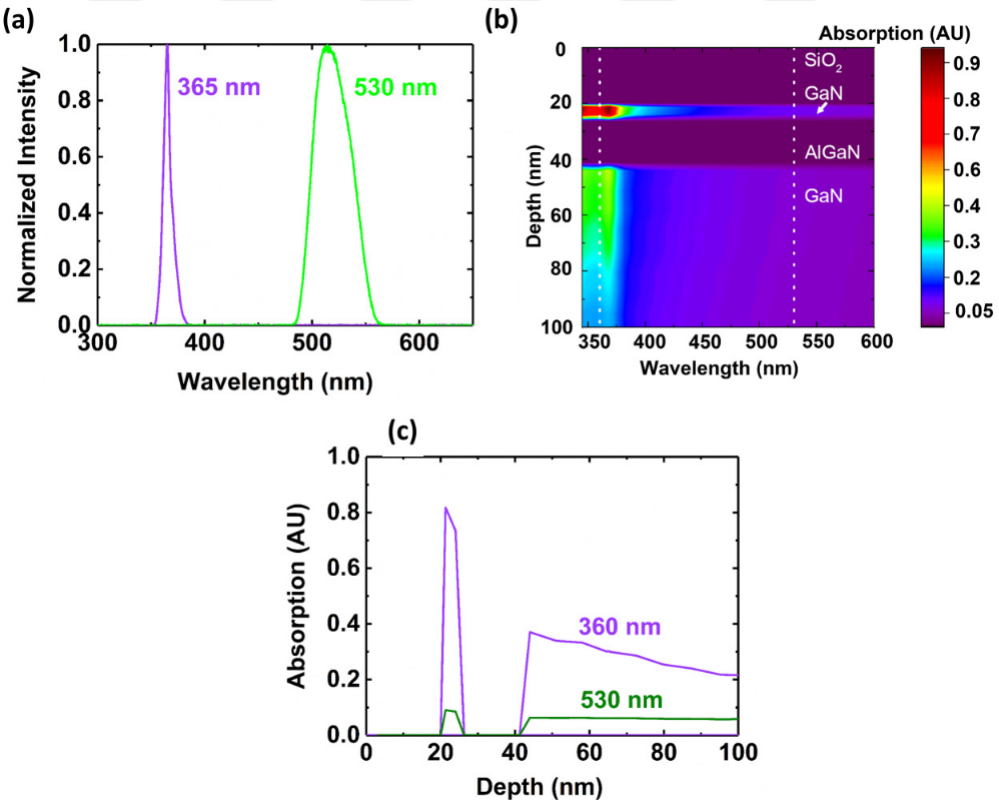


Figure 4.14. (a) Light source spectrum for both UV and visible sources. (b) Absorption in the device layout related to wavelength. (c) Linearized absorption.

UV TTI experiments were conducted by the same procedure with the visible TTI measurements. Yet, to attain finer spatial resolution, lens was replaced with Olympus LUCPFLN 40x with the numerical aperture value of 0.6 which provides 0.3 µm spatial resolution. Finally, the thermoreflectance coefficient for determining the reflectivity change in the GaN layer is set to $-3 \times 10^{-3} \pm 1.63 \times 10^{-5} °C^{-1}$.

Since the UV light is absorbed predominantly around the near surface, the captured temperature values by this method can be interpreted as a weighted average within the probe region in accordance with the absorption ratio of the UV light. Considering this, the UV TTI results are presented in Figure 4.15 for the 5 W/mm case. The probe region of the UV TTI method is shown in Figure 4.15(a), which is the observable region between the ohmic contacts (drain and source) and the gate. These regions are shown on the real device in Figure 4.15. The acquired temperature distribution by the CCD camera for the 5 W/mm power dissipation is presented in Figure 4.15(c) and

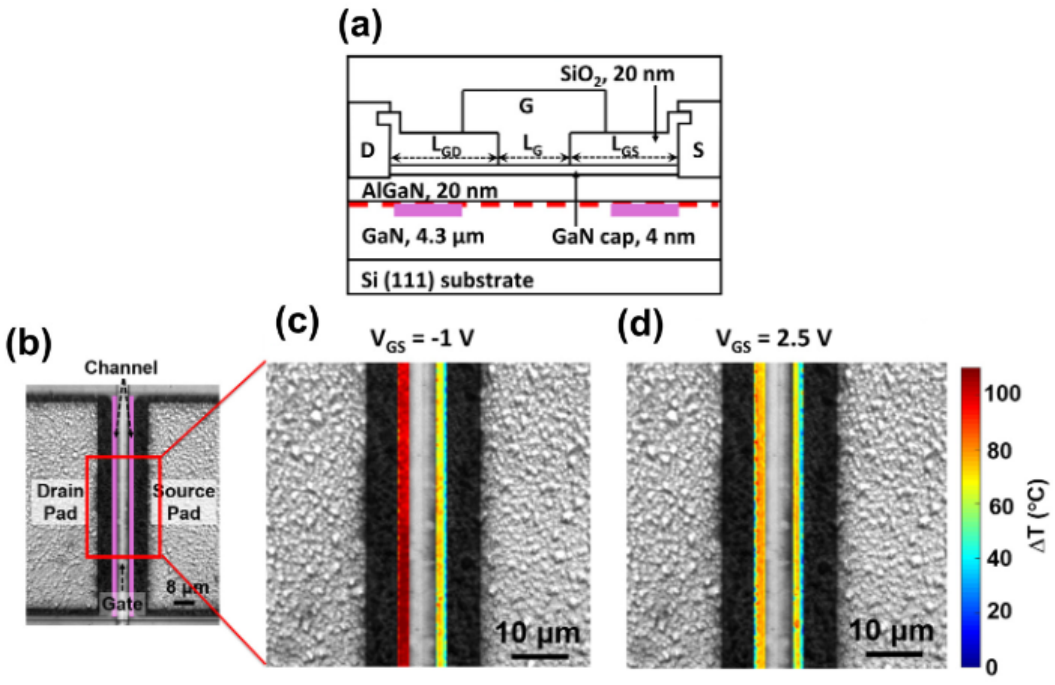


Figure 4.15. (a) UV TTI probe region. (b) Probe region representation on the real device. Temperature distribution in the probe region when the power dissipation is 5 W/mm for (c) partially pinched-off and (d) fully open channel conditions.

(d).

The measured temperature values in their distinct probe regions are compared in Figure 4.16, in terms of the diffusive simulation, visible TTI, and UV TTI. Thus, the gate surface temperature rise can only be assessed by the visible TTI and diffusive model, whereas the temperature rise in the gap between the ohmic contacts and the gate is presented in terms of the UV TTI and the diffusive model. It can be seen that the temperature values acquired from the gate-drain region are significantly higher than the other parts of the device in the partially pinched-off condition. When the power is 2.5 W/mm, the UV TTI measures ∼9°C more temperature rise by probing the gate-drain gap compared to the visible TTI. Also, this discrepancy increases to ∼27°C with the higher power condition (5 W/mm). Hence, these differences show that the visible TTI, by measuring the gate surface, cannot estimate the channel temperature rise and

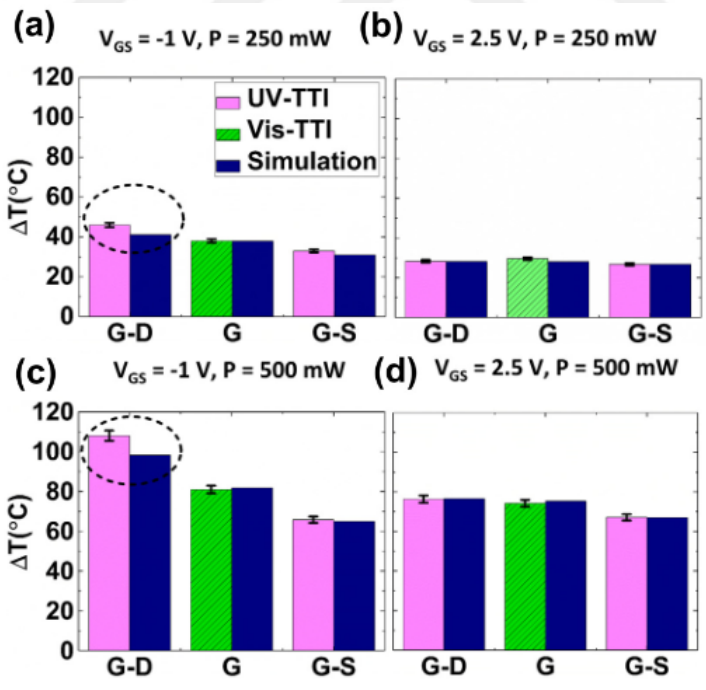


Figure 4.16. UV-TTI, visible TTI, and diffusive simulation comparison for (a) partially pinched-off condition with 2.5 W/mm, (b) fully open channel condition with 2.5 W/mm, (c) partially pinched-off condition with 5 W/mm, (d) fully open channel condition with 5 W/mm.

that error increases with the higher power. Another important aspect of these results is the difference between the UV TTI and the electro-thermal estimations in the gate-drain region. Although the temperature measurements in the gate-drain region yield same results with the Fourier estimation in the fully open channel devices, discrepancies were observed in the partially pinched-off condition. These differences are highlighted with the dashed lines in Figure 4.16. For the power dissipation of 2.5 W/mm, the UV TTI results ∼6°C higher temperature rise in the gate-drain region. By increasing the power (5 W/mm), the difference rises to ∼10°C. Therefore, since the UV TTI captures the weighted average temperature in the GaN layers, the difference between the Fourier results can be interpreted as a sign of the sub-continuum thermal transport that cannot be captured by the diffusive simulations. In the wake of these findings, the partially pinched-off operation condition is modelled with the phonon BTE model to investigate sub-continuum thermal transport.

4.2.4. Sub-continuum Model

The discrepancy between the UV TTI and the Fourier in the gate-drain probe region can be attributed to the sub-continuum thermal transport when the device is operated with the partially pinched-off condition. Therefore, the phonon BTE model introduced in Chapter 2 and 3 is operated to understand the discrepancy in the partially pinched-off condition.

The solution procedure for solving the gray phonon BTE is same with the model used in Chapter 3. The heat generation data obtained from the electrical simulations are implemented as a volumetric heat generation in the BTE domain. The horizontal length of the domain is selected as $L = 7$ µm and the vertical length is set to $H = 3$ µm, so that diffusive propagation is allowed away from the hot-spot since the boundary conditions for the BTE solution are acquired from the 3-D diffusive thermal model. The BTE domain and the boundary conditions are given by Figure 4.17 (a). Similar to the previous model, the AlGaN layer is modelled as GaN in the BTE simulation. The domain is discretized with 240,000 (800×300) nodes spatially, and S_3 quadratures is

used for angular discretization.

As explained before, the solution procedure for the gray approximation can differ in terms of setting the mean free path or the group velocity firstly. In the previous BTE calculations (Chapter 2 and 3), the gray model was solved by considering 400 nm mean free path initially. However, to validate the UV TTI in this section, the initial group velocity approach is also implemented alongside 400 nm initial mean free path.

Therefore, two different sets of temperature values are presented in this study. First set of temperature distribution is calculated by setting the mean free path of the phonons 400 nm in GaN medium. As a result, by using kinetic theory, the relaxation time varies between 900 and ∼1000 ps relying upon the average conductivity calculated for BTE domain in the diffusive simulations. For the second set of the temperature distribution, first, group velocity for the phonons is set, which is the average phonon group velocity in GaN and calculated ∼1800 m/s [120]. With this way, the relaxation time changes between ∼40 and ∼50 ps, and the mean free path varies in the range of 84-97 nm depending on the conductivity.

The phonon BTE temperature rise estimation in the partially pinched-off condition is presented in Figure 4.17 (b) along with the UV TTI results. The shadowed part in the figure indicates the area that cannot be measured by the UV TTI method. It is seen that phonon BTE method calculates higher temperature in the device channel compared the diffusive results. Considering the 2.5 W/mm condition, when the mean free path is 400 nm, the peak temperature rise is calculated ∼53°C which drops to ∼47°C if the fixed velocity approach is considered. Whereas, Fourier calculates ∼44°C temperature rise. Thus, with the both gray methods, higher temperature rise is calculated as a result of the size effects. Along with higher power (5 W/mm), differences stemming from the size effects increase as expected. The maximum temperature rise values are calculated ∼119°C and 102°C for 400 nm and 84-97 nm phonon mean free paths, respectively. However, diffusive simulation results ∼97.5°C temperature rise. It can be seen that although smaller mean free paths contribute to more diffusive ther-

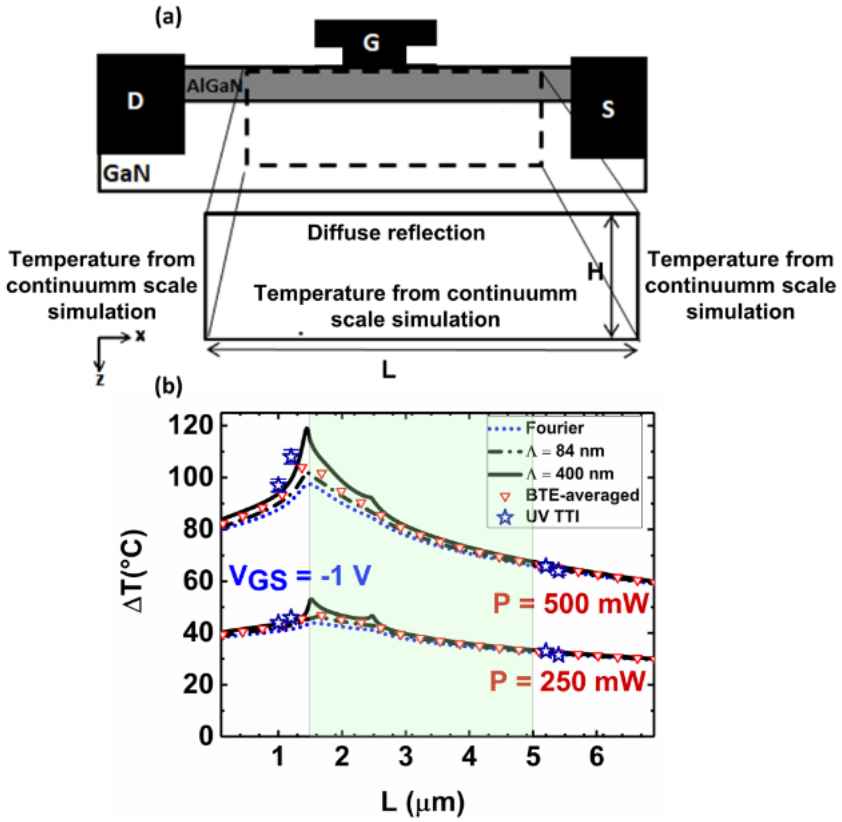


Figure 4.17. (a) Phonon BTE domain, (b) temperature distribution in the device channel.

mal transport, discrepancies still last. Considering the UV TTI results, experiments still cannot capture the actual hot-spot since it mainly spawns under the gate metal. Yet, the UV TTI and phonon BTE results yield similar estimations in the UV TTI probe region. In the 2.5 W/mm case, the UV TTI and the phonon BTE determine almost same temperature rise with a difference smaller than ∼1.5°C in the gate-drain region. Similarly, the experimental and phonon BTE results overlap in the gate-source probe region. Furthermore, they agree well in the 5 W/mm case as well. Especially, in the gate-source region, all methods yield same temperature rise. However, in the gate-drain region, the difference between the UV TTI and the phonon BTE is slightly higher by ∼8°C compared the 2.5 W/mm case. Yet in the second probe point (in the gate-drain probe), the difference becomes <1.5°C. Since the UV TTI still cannot capture the actual hot-spot location, the maximum temperature rise calculated ∼119°C by the phonon BTE is not observable with the experiments. Moreover, the temperature

sets by the two gray initializations are averaged and weighted in accordance with the TTI probing regions considering the previous absorption calculations. These weighted temperatures also agree well with the experiments as shown in Figure 4.17 (b). Consequently, the agreement between the phonon BTE and the UV TTI highlights the size effects in the device channel. So, to capture the temperature rise in channel accurately, especially in the partially pinched-off conditions, sub-continuum heat transport should be considered. This is demonstrated by experiments and the results indicate that micro-Raman and visible TTI experiments, which are conduced prevalently for device characterization, cannot estimate the maximum device temperature as suggested in the virtual experiments section.

5. CONCLUSIONS AND FUTURE RESEARCH

Alongside the trend that achieving smaller sizes in the semiconductor industry, reliability concerns grow. Recent developments have shown that solid-state devices can be produced on the order of nanometers. Approaching atomic scales in novel devices brings concerns about physical limits, and more efficient devices are needed. Particularly in power electronics, smaller devices that withstand extreme conditions are required for cutting edge technologies. Regarding the thermal aspects, devices may undergo extreme self-heating effects making them prone to degradation of device performance and lifetime. Since such confined heat generation impacts cannot be determined by the diffusive thermal transport assumption, in this thesis sub-continuum heat transport resulting from localized Joule heating in semiconductor media was investigated.

In Chapter 2, numerical methods for Fourier's law of heat conduction and gray phonon BTE solutions were introduced. Although the sub-continuum thermal transport was investigated previously, a comprehensive study considering horizontal and vertical lengths, area size and power conditions together is conducted the first time in this thesis. Also, heat flux approximation was implemented to calculate size effects instead of volumetric heat generation. Consequently, it was observed that although aspect ratio of heat generation area alters the size effects, area was found as the main factor. However, for the aspect ratios bigger or smaller than 2, it was seen that the size effects reduce significantly. Also, it was observed that when the heat generation profile spreads horizontally, the phonon BTE model with boundary flux approximation can estimate the size effects stemming from the volumetric heat generation with error span of 0.5-8%. Yet, for the vertically spread profiles, errors were found to be significantly high. Thus, for the devices subjected to horizontally spread generation, boundary heat flux approximation can be used to alleviate computational cost.

In Chapter 3, the size effects were investigated in a realistic AlGaN/GaN HEMT. To do this electro-thermal model coupled with phonon BTE was introduced. It was observed that for all the operational conditions, heat generation profile remains horizontally spread and the vertical length does not change much in the AlGaN/GaN HEMT. However, similar trends with results of Chapter 2 were seen. In the partially pinched-off condition, the area reduces, hence, this leads to higher discrepancy between the continuum and sub-continuum approaches. Yet, bigger generation area size and aspect ratio in the open channel condition lead to significantly smaller discrepancy between the two methods. Finally, the heat flux boundary approximation was implemented for the real device structure. It was observed that for the open channel condition, the approximation calculates with errors as small as $\sim$0.6%. Negative gate voltage influenced errors slightly and the temperature rise with volumetric heat generation was calculated by error of $\sim$1.7-3.1%. Therefore, to reduce the number of mesh elements and computational cost in AlGaN/GaN HEMTs, boundary flux method can be used. Yet, power condition should be considered as it increases errors.

In Chapter 4, the accuracy of two prevalent optical experimental methods for solid-state devices were investigated by both virtual and actual experiments. In the virtual experiment investigation, the micro-Raman and the visible TTI methods were modelled numerically. According to virtual experiment results, it was observed that neither the micro-Raman nor the visible TTI can determine the peak temperature within the device active channel. Also, the use of the phonon BTE method showed that the validation of the experiments cannot be done by continuum scale analysis since they underestimate the peak temperature. It was seen that the errors increase with power condition. Furthermore, the field plate structure reduces the experimental deviation from the peak temperature despite the geometrical constraints for probe region. These numerical calculations were proven by the actual visible TTI and the UV TTI experiments later in this chapter. The agreement between the UV TTI method and the phonon BTE calculations proved the size effects, thus size effects were demonstrated by experimentally in a fabricated HEMT. Moreover, it was observed that the visible TTI method cannot capture maximum device temperature by assessing the metal con-

tact surfaces, and continuum thermal transport underestimates the peak temperature. Considering the mean-time-to-failure calculations for commercial devices, such deviations could lead to detrimental consequences, therefore, the sub-continuum numerical models are imperative for thermal characterization of semiconductor devices.

To enhance the sub-continuum heat transport in semiconductors following topics should be considered in the future:

- In Chapter 2, the heat generation and the heat flux results were investigated by assuming an arbitrary GaN medium. However, in other semiconductor materials, such as Si, SiC, and AlGaAs, different results may be obtained because of the phonon properties. Hence, other materials should be investigated to understand these effects fully.
- In the phonon BTE model, gray approximation was used since the domain was selected GaN. However, gray and full dispersion model impact on the heat flux boundary condition is unknown and should be assessed.
- The aspect ratio in Chapter 2 varies from 1/32 to 32, yet in the AlGaN/GaN HEMT, it was observed that Joule heating occurs with much bigger aspect ratios, hence, wider range of conditions should be investigated in the future.
- For the device simulations, acquired Joule heating data was horizontally spread and profile with an aspect ratio smaller than 2 was not observed. Yet, to see Joule heating profile effects in other devices, for instance, LED, FinFET, and laser structures, such devices should be modelled by electro-thermal models to see different type of heating profiles.
- The modelled device in this study has field plate and passivation with single length and thickness values. It is known that the field plate and the passivation alter Joule heating profile, yet these effects were not investigated for set of lengths and thicknesses by sub-continuum models. Thus, the structural effects can be assessed with the phonon BTE to see real influence on device temperature.
- Although the TTI model was validated by actual experiments, micro-Raman method was assessed by numerical methods only. Thus, comparison of the TTI

and the actual micro-Raman should be done in the future.

- For the gray phonon BTE solution, fixed mean free path or group velocity values are selected to represent overall phonon scattering in the domain. However, correct values for modelling full band events precisely is unknown, and investigation on this subject can increase the accuracy of the gray phonon BTE model.

REFERENCES

1. Chen, G., *Nanoscale Energy Transport and Conversion*, Oxford University Press, 1st edition, 2005.

2. Callister, W. D. and D. G. Rethwisch, *Materials Science and Engineering*, Wiley, 9th edition, 2014.

3. Sommerfeld, A., "Zur Elektronentheorie der Metalle auf Grund der Fermischen Statistik - II. Teil: Thermo-elektrische, galvano-magnetische und thermomagnetische Vorgänge", *Zeitschrift für Physik*, Vol. 47, No. 1-2, pp. 43–60, 1928.

4. Vella, E., F. Messina, M. Cannas and R. Boscaino, "Unraveling exciton dynamics in amorphous silicon dioxide: Interpretation of the optical features from 8 to 11 eV", *Physical Review B - Condensed Matter and Materials Physics*, Vol. 83, No. 17, pp. 1–8, 2011.

5. Johnson, E., "Physical limitations on frequency and power parameters of transistors", *1958 IRE International Convention Record*, Vol. 13, pp. 27–34, 1965.

6. Adinolfi, V. and E. H. Sargent, "Photovoltage field-effect transistors", *Nature*, Vol. 542, No. 7641, pp. 324–327, 2017.

7. Keyes, R. W., "Physical limits of silicon transistors and circuits", *Reports on Progress in Physics*, Vol. 68, No. 12, pp. 2701–2746, 2005.

8. Chau, R., B. Boyanov, B. Doyle, M. Doczy, S. Datta, S. Hareland, B. Jin, J. Kavalieros and M. Metz, "Silicon nano-transistors for logic applications", *Physica E: Low-Dimensional Systems and Nanostructures*, Vol. 19, pp. 1–5, 2003.

9. Sze, S. M. and M.-K. Lee, *Semiconductor Devices: Physics and Technology*, Wiley, 3rd edition, 2012.

10. Mishra, U. K., L. Shen, T. E. Kazior and Y. F. Wu, "GaN-based RF power devices and amplifiers", *Proceedings of the IEEE*, Vol. 96, No. 2, pp. 287–305, 2008.

11. Lundstrom, M., "Applied physics: Moore's law forever?", *Science*, Vol. 299, No. 5604, pp. 210–211, 2003.

12. Ando, H., Y. Yoshida, A. Inoue, I. Sugiyama, T. Asakawa, K. Morita, T. Muta, T. Motokurumada, S. Okada, H. Yamashita, Y. Satsukawa, A. Konmoto, R. Yamashita and H. Sugiyama, "A 1.3GHz fifth generation SPARC64 microprocessor", *Proceedings - Design Automation Conference*, pp. 702–705, 2003.

13. Ye, P., T. Ernst and M. V. Khare, "The last silicon transistor: Nanosheet devices could be the final evolutionary step for Moore's Law", *IEEE Spectrum*, Vol. 56, No. 8, pp. 30–35, 2019.

14. Shalf, J., "The future of computing beyond Moore's Law", *Philosophical Transactions of the Royal Society A: Mathematical, Physical and Engineering Sciences*, Vol. 378, No. 2166, pp. 1–15, 2020.

15. James, W., *Electro-Thermal-Mechanical Modeling of GaN HFETs and MOSHFETs*, M.S. Thesis, Georgia Institute of Technology, 2011.

16. Zhang, Z. M., *Nano/Microscale Heat Transfer*, Mechanical Engineering Series, Springer, Cham, 2nd edition, 2020.

17. Lasance, C. J. and A. Poppe, *Thermal Management for LED Applications*, Springer-Verlag New York, 1st edition, 2014.

18. Sony Global, "Sony Global - Press Release - Sony Announces Important Milestone in Blue-Green Semiconductor Laser Diode Development", `https://www.sony.net/SonyInfo/News/Press_Archive/199601/96D-014E/`, 1996, accessed in July 2020.

19. Huang, M. S., C. C. Hung, Y. C. Fang, W. C. Lai and Y. L. Chen, "Optical design and optimization of light emitting diode automotive head light with digital micromirror device light emitting diode", *Optik*, Vol. 121, No. 10, pp. 944–952, 2010.

20. Lee, S. W., C. H. Lau, S. P. Chan, K. Y. Ma, M. H. Ng, Y. W. Ng, K. H. Lee and J. C. Lo, "Development and prototyping of a HB-LED array module for indoor solid state lighting", *2006 Conference on High Density Microsystem Design and Packaging and Component Failure Analysis, HDP'06*, pp. 141–145, 2006.

21. Werle, P., "A review of recent advances in semiconductor laser based gas monitors", *Spectrochimica Acta Part A: Molecular and Biomolecular Spectroscopy*, Vol. 54, No. 2, pp. 197 – 236, 1998.

22. Moore, G. E., "Cramming more components onto integrated circuits", *Proceedings of the IEEE*, Vol. 86, No. 1, pp. 82–85, 1998.

23. Rupp, K. and S. Selberherr, "The economic limit to Moore's law", *IEEE Transactions on Semiconductor Manufacturing*, Vol. 24, pp. 1–4, 2011.

24. Huang, X., W. C. Lee, C. Kuo, D. Hisamoto, L. Chang, J. Kedzierski, E. Anderson, H. Takeuchi, Y. K. Choi, K. Asano, V. Subramanian, T. J. King, J. Bokor and C. Hu, "Sub 50-nm FinFET: PMOS", *Technical Digest - International Electron Devices Meeting*, pp. 67–70, 1999.

25. Yu, B., L. Chang, S. Ahmed, H. Wang, S. Bell, C. Y. Yang, C. Tabery, C. Ho, Q. Xiang, T. J. King, J. Bokor, C. Hu, M. R. Lin and D. Kyser, "FinFET scaling to 10 nm gate length", *Technical Digest - International Electron Devices Meeting*, pp. 251–254, 2002.

26. Chang, J., Y. H. Chen, G. Chan, H. Cheng, P. S. Wang, Y. Lin, H. Fujiwara, R. Lee, H. J. Liao, P. W. Wang, G. Yeap and Q. Li, "A 5nm 135Mb SRAM

in EUV and High-Mobility-Channel FinFET Technology with Metal Coupling and Charge-Sharing Write-Assist Circuitry Schemes for High-Density and Low-VMIN Applications", *Digest of Technical Papers - IEEE International Solid-State Circuits Conference*, pp. 238–240, 2020.

27. Wood, A., C. Dragon and W. Burger, "High performance silicon LDMOS technology for 2GHz RF power amplifier applications", *Technical Digest - International Electron Devices Meeting*, pp. 87–90, 1996.

28. Sun, S. C. and J. D. Plummer, "Modeling of the On-Resistance of LDMOS, VDMOS, and VMOS Power Transistors", *IEEE Transactions on Electron Devices*, Vol. 27, No. 2, pp. 356–367, 1980.

29. Theeuwen, S. J. and J. H. Qureshi, "LDMOS technology for RF power amplifiers", *IEEE Transactions on Microwave Theory and Techniques*, Vol. 60, No. 6 PART 2, pp. 1755–1763, 2012.

30. Nylander, J., J. Tiren, U. Magnusson, H. Norde, K. Bohlin, F. Masszi and P. A. Tove, "Complementary Si MESFET Concept Using Silicon-on-Sapphire Technology", *IEEE Electron Device Letters*, Vol. 9, No. 1, pp. 47–49, 1988.

31. Beyer, J. B., S. N. Prasad, R. C. Becker, J. E. Nordman and G. K. Hohenwarter, "MESFET Distributed Amplifier Design Guidelines", *IEEE Transactions on Microwave Theory and Techniques*, Vol. 32, No. 3, pp. 268–275, 1984.

32. Dundar, C., D. Kara and N. Donmezer, "The Effects of Gate-Connected Field Plates on Hotspot Temperatures of AlGaN/GaN HEMTs", *IEEE Transactions on Electron Devices*, Vol. 67, No. 1, pp. 57–62, 2020.

33. Sun, R., J. Lai, W. Chen and B. Zhang, "GaN Power Integration for High Frequency and High Efficiency Power applications: a Review", *IEEE Access*, Vol. 8, pp. 15529–15542, 2020.

34. Keshmiri, N., D. Wang, B. Agrawal, R. Hou and A. Emadi, "Current Status and Future Trends of GaN HEMTs in Electrified Transportation", *IEEE Access*, Vol. 8, pp. 70553–70571, 2020.

35. Zhang, H., B. Ge, Y. Liu, S. Bayhan, R. S. Balog and H. Abu-Rub, "Comparison of GaN and SiC power devices in application to MW-scale quasi-Z-source cascaded multilevel inverters", *ECCE 2016 - IEEE Energy Conversion Congress and Exposition, Proceedings*, pp. 1–7, 2016.

36. Mishra, U. K., P. Parikh and Y. F. Wu, "AlGaN/GaN HEMTs - An overview of device operation and applications", *Proceedings of the IEEE*, Vol. 90, No. 6, pp. 1022–1031, 2002.

37. Denninghoff, D., J. Lu, M. Laurent, E. Ahmadi, S. Keller and U. K. Mishra, "N-polar GaN/InAlN MIS-HEMT with 400-GHz f max", *Device Research Conference - Conference Digest, DRC*, pp. 151–152, 2012.

38. Ishida, T., "GaN HEMT technologies for space and radio applications", *Microwave Journal*, Vol. 54, No. 8, pp. 56–66, 2011.

39. Satoh, T., K. Osawa and A. Nitta, "GaN HEMT for Space Applications", *2018 IEEE BiCMOS and Compound Semiconductor Integrated Circuits and Technology Symposium, BCICTS 2018*, pp. 136–139, 2018.

40. Donmezer, N. and S. Graham, "The impact of noncontinuum thermal transport on the temperature of AlGaN/GaN HFETs", *IEEE Transactions on Electron Devices*, Vol. 61, No. 6, pp. 2041–2048, 2014.

41. Venkatachalam, A., W. T. James and S. Graham, "Electro-thermo-mechanical modeling of GaN-based HFETs and MOSHFETs", *Semiconductor Science and Technology*, Vol. 26, No. 8, pp. 1–6, 2011.

42. Xu, C., S. K. Kolluri, K. Endo and K. Banerjee, "Analytical thermal model

for self-heating in advanced FinFET devices with implications for design and reliability", *IEEE Transactions on Computer-Aided Design of Integrated Circuits and Systems*, Vol. 32, No. 7, pp. 1045–1058, 2013.

43. Dallas, J., G. Pavlidis, B. Chatterjee, J. S. Lundh, M. Ji, J. Kim, T. Kao, T. Detchprohm, R. D. Dupuis, S. Shen, S. Graham and S. Choi, "Thermal characterization of gallium nitride p-i-n diodes", *Applied Physics Letters*, Vol. 112, No. 7, pp. 1–5, 2018.

44. Petroski, J., "Spacing of high-brightness LEDs on metal substrate PCB's for proper thermal performance", *Thermomechanical Phenomena in Electronic Systems -Proceedings of the Intersociety Conference*, Vol. 2, pp. 507–514, 2004.

45. Ni, C., Z. Aksamija, J. Y. Murthy and U. Ravaioli, "Coupled electro-thermal simulation of MOSFETs", *Journal of Computational Electronics*, Vol. 11, No. 1, pp. 93–105, 2012.

46. Thurmond, C. D., "The Standard Thermodynamic Functions for the Formation of Electrons and Holes in Ge, Si, GaAs, and GaP", *Journal of The Electrochemical Society*, Vol. 122, No. 8, pp. 1133–1141, 1975.

47. Oates, A. S., "Will reliability limit Moore's law?", *Technical Digest - International Electron Devices Meeting, IEDM*, pp. 1–1, 2015.

48. MacK, C. A., "Fifty years of Moore's law", *IEEE Transactions on Semiconductor Manufacturing*, Vol. 24, pp. 202–207, 2011.

49. Chou, Y. C., D. Leung, I. Smorchkova, M. Wojtowicz, R. Grundbacher, L. Callejo, Q. Kan, R. Lai, P. H. Liu, D. Eng and A. Oki, "Degradation of AlGaN/GaN HEMTs under elevated temperature lifetesting", *Microelectronics Reliability*, Vol. 44, No. 7, pp. 1033–1038, 2004.

50. Singhal, S., T. Li, A. Chaudhari, A. W. Hanson, R. Therrien, J. W. Johnson,

W. Nagy, J. Marquart, P. Rajagopal, J. C. Roberts, E. L. Piner, I. C. Kizilyalli and K. J. Linthicum, "Reliability of large periphery GaN-on-Si HFETs", *Microelectronics Reliability*, Vol. 46, No. 8, pp. 1247–1253, 2006.

51. Kara, D., *Thermal Effects of Gate Connected Field-Plates and Surface Passivation on AlGaN/GaN HEMTs*, M.S. Thesis, Middle East Technical University, 2018.

52. Kerber, A. and T. Nigam, "Bias temperature instability in scaled CMOS technologies: A circuit perspective", *Microelectronics Reliability*, Vol. 81, pp. 31–40, 2018.

53. Su, L. T., J. E. Chung, A. A. Dimitri, K. E. Goodson and M. I. Flik, "Measurement and Modeling of Self-Heating in SOI NMOSFET's", *IEEE Transactions on Electron Devices*, Vol. 41, No. 1, pp. 69–75, 1994.

54. Donmezer, F. N., *Multiscale Eletro-Thermal Modeling of AlGaN/GaN Heterostructure Field Effect Transistors*, Ph.D. Thesis, Georgia Institute of Technology, 2013.

55. Christensen, A. and S. Graham, "Thermal effects in packaging high power light emitting diode arrays", *Applied Thermal Engineering*, Vol. 29, No. 2-3, pp. 364–371, 2009.

56. Narendran, N. and Y. Gu, "Life of LED-based white light sources", *IEEE/OSA Journal of Display Technology*, Vol. 1, No. 1, pp. 167–170, 2005.

57. Heller, E. R. and A. Crespo, "Electro-thermal modeling of multifinger AlGaN/GaN HEMT device operation including thermal substrate effects", *Microelectronics Reliability*, Vol. 48, No. 1, pp. 45–50, 2008.

58. Benbakhti, B., A. Soltani, K. Kalna, M. Rousseau and J. C. De Jaeger, "Effects of self-heating on performance degradation in AlGaN/GaN-based devices", *IEEE Transactions on Electron Devices*, Vol. 56, No. 10, pp. 2178–2185, 2009.

59. Pomeroy, J. W., M. J. Uren, B. Lambert and M. Kuball, "Operating channel temperature in GaN HEMTs: DC versus RF accelerated life testing", *Microelectronics Reliability*, Vol. 55, pp. 2505–2510, 2015.

60. Zhang, Y., M. Sun, Z. Liu, D. Piedra, H. S. Lee, F. Gao, T. Fujishima and T. Palacios, "Electrothermal simulation and thermal performance study of GaN vertical and lateral power transistors", *IEEE Transactions on Electron Devices*, Vol. 60, No. 7, pp. 2224–2230, 2013.

61. Alexeev, A., G. Martin and G. Onushkin, "Multiple heat path dynamic thermal compact modeling for silicone encapsulated LEDs", *Microelectronics Reliability*, Vol. 87, pp. 89–96, 2018.

62. Narumanchi, S. V., J. Y. Murthy and C. H. Amon, "Boltzmann transport equation-based thermal modeling approaches for hotspots in microelectronics", *Heat and Mass Transfer/Waerme- und Stoffuebertragung*, Vol. 42, pp. 478–491, 2006.

63. Yang, R., G. Chen, M. Laroche and Y. Taur, "Simulation of nanoscale multidimensional transient heat conduction problems using ballistic-diffusive equations and phonon Boltzmann equation", *Journal of Heat Transfer*, Vol. 127, No. 3, pp. 298–306, 2005.

64. Hu, Y., L. Zeng, A. J. Minnich, M. S. Dresselhaus and G. Chen, "Spectral mapping of thermal conductivity through nanoscale ballistic transport", *Nature Nanotechnology*, Vol. 10, No. 8, pp. 701–706, 2015.

65. Ziade, E., J. Yang, G. Brummer, D. Nothern, T. Moustakas and A. J. Schmidt, "Thickness dependent thermal conductivity of gallium nitride", *Applied Physics Letters*, Vol. 110, No. 3, 2017.

66. Nasri, F., F. Echouchene, M. F. Ben Aissa, I. Graur and H. Belmabrouk, "In-

vestigation of Self-Heating Effects in a 10-nm SOI-MOSFET with an Insulator Region Using Electrothermal Modeling", *IEEE Transactions on Electron Devices*, Vol. 62, No. 8, pp. 2410–2415, 2015.

67. Donmezer, F. N., M. Islam, S. Graham and D. Yoder, "Modeling the hotspot temperature in AlGaN/GaN high electron mobility transistors using a non-gray phonon BTE solver", *ASME International Mechanical Engineering Congress and Exposition, Proceedings (IMECE)*, Vol. 9, pp. 1175–1188, 2012.

68. Donmezer, F. N., D. Singh, W. James, A. Christensen, S. Graham and J. Y. Murthy, "Lattice boltzmann and discrete ordinates methods for phonon transport modeling: A comparative study", *ASME 2011 International Mechanical Engineering Congress and Exposition, IMECE 2011*, Vol. 10, pp. 333–343, 2011.

69. Sinha, S., E. Pop, R. W. Dutton and K. E. Goodson, "Non-equilibrium phonon distributions in sub-100 nm silicon transistors", *Journal of Heat Transfer*, Vol. 128, No. 7, pp. 638–647, 2006.

70. Narumanchi, S. V., J. Y. Murthy and C. H. Amon, "Comparison of different phonon transport models for predicting heat conduction in silicon-on-insulator transistors", *Journal of Heat Transfer*, Vol. 127, No. 7, pp. 713–723, 2005.

71. Nghiem, T. T., N. Trannoy and J. Randrianalisoa, "Monte Carlo prediction of ballistic effect on phonon transport in silicon in the presence of small localized heat source", *Nanotechnology*, Vol. 30, No. 41, pp. 1–12, 2019.

72. Blackburn, D. L., "Temperature measurements of semiconductor devices - A review", *Annual IEEE Semiconductor Thermal Measurement and Management Symposium*, Vol. 20, pp. 70–80, 2004.

73. Park, J., M. W. Shin and C. C. Lee, "Thermal modeling and measurement of AlGaN-GaN HFETs built on sapphire and SiC substrates", *IEEE Transactions*

on Electron Devices, Vol. 51, No. 11, pp. 1753–1759, 2004.

74. Killat, N., M. Kuball, T. M. Chou, U. Chowdhury and J. Jimenez, "Temperature assessment of AlGaN/GaN HEMTs: A comparative study by Raman, electrical and IR thermography", *IEEE International Reliability Physics Symposium Proceedings*, pp. 528–531, 2010.

75. Conway, A. M., P. M. Asbeck, J. S. Moon and M. Micovic, "Accurate thermal analysis of GaN HFETs", *Solid-State Electronics*, Vol. 52, No. 5, pp. 637–643, 2008.

76. Burzo, M. G., P. L. Komarov and P. E. Raad, "Noncontact transient temperature mapping of active electronic devices using the thermoreflectance method", *IEEE Transactions on Components and Packaging Technologies*, Vol. 28, No. 4, pp. 637–643, 2005.

77. Shigekawa, N., K. Shiojima and T. Suemitsu, "Optical study of high-biased AlGaN/GaN high-electron-mobility transistors", *Journal of Applied Physics*, Vol. 92, No. 1, pp. 531–535, 2002.

78. Kuball, M., S. Rajasingam, A. Sarua, M. J. Uren, T. Martin, B. T. Hughes, K. P. Hilton and R. S. Balmer, "Measurement of temperature distribution in multifinger AlGaN/GaN heterostructure field-effect transistors using micro-Raman spectroscopy", *Applied Physics Letters*, Vol. 82, No. 1, pp. 124–126, 2003.

79. Ostermeir, R., K. Brunner, G. Abstreiter and W. Weber, "Temperature Distribution in Si-MOSFET's Studied by Micro Raman Spectroscopy", *IEEE Transactions on Electron Devices*, Vol. 39, No. 4, pp. 858–863, 1992.

80. Maize, K., A. Ziabari, W. D. French, P. Lindorfer, B. Oconnell and A. Shakouri, "Thermoreflectance CCD imaging of self-heating in power MOSFET arrays", *IEEE Transactions on Electron Devices*, Vol. 61, No. 9, pp. 3047–3053, 2014.

81. Chatterjee, B., J. S. Lundh, D. Shoemaker, T. K. Kim, H. Kim, N. C. Giebnik, J. S. Kwak, J. Cho and S. Choi, "Characterization of the Interdependence Between the Light Output and Self-Heating of Gallium Nitride Light-Emitting Diodes", *Journal of Electronic Packaging*, Vol. 142, No. 3, pp. 1–7, 2020.

82. Maize, K., E. Heller, D. Dorsey and A. Shakouri, "Thermoreflectance CCD imaging of self heating in AlGaN/GaN high electron mobility power transistors at high drain voltage", *Annual IEEE Semiconductor Thermal Measurement and Management Symposium*, pp. 173–181, 2012.

83. Farzaneh, M., K. Maize, D. Lüeren, J. A. Summers, P. M. Mayer, P. E. Raad, K. P. Pipe, A. Shakouri, R. J. Ram and J. A. Hudgings, "CCD-based thermoreflectance microscopy: Principles and applications", *Journal of Physics D: Applied Physics*, Vol. 42, No. 14, pp. 1–20, 2009.

84. Chapuis, P., T. T. T. Nghiem, C. A. Da Cruz and E. Nefzaoui, "Thermal transport phenomena beyond the diffusive regime", *2016 MIXDES - 23rd International Conference Mixed Design of Integrated Circuits and Systems*, pp. 32–37, 2016.

85. Mingo, N. and L. Yang, "Phonon transport in nanowires coated with an amorphous material: An atomistic Green's function approach", *Phys. Rev. B*, Vol. 68, pp. 1–12, 2003.

86. Murthy, J. Y., S. V. J. Narumanchi, J. A. Pascual-Gutierrez, T. Wang, C. Ni and S. R. Mathur, "Review of Multiscale Simulation in Submicron Heat Transfer", *International Journal for Multiscale Computational Engineering*, Vol. 3, No. 1, pp. 5–32, 2005.

87. Donmezer, N., M. Islam, P. D. Yoder and S. Graham, "The Impact of Nongray Thermal Transport on the Temperature of AlGaN/GaN HFETs", *IEEE Transactions on Electron Devices*, Vol. 62, No. 8, pp. 2437–2444, 2015.

88. Wang, K., J. Simon, N. Goel and D. Jena, "Optical study of hot electron transport in GaN: Signatures of the hot-phonon effect", *Applied Physics Letters*, Vol. 88, No. 2, pp. 1–3, 2006.

89. Tsen, K. T., D. K. Ferry, A. Botchkarev, B. Sverdlov, A. Salvador and H. Morkoc, "Time-resolved Raman studies of the decay of the longitudinal optical phonons in wurtzite GaN", *Applied Physics Letters*, Vol. 72, No. 17, pp. 2132–2134, 1998.

90. Chatterjee, B., C. Dundar, T. E. Beechem, E. Heller, D. Kendig, H. Kim, N. Donmezer and S. Choi, "Nanoscale electro-thermal interactions in AlGaN/GaN high electron mobility transistors", *Journal of Applied Physics*, Vol. 127, No. 4, pp. 1–13, 2020.

91. Yang, R. and G. Chen, "Thermal conductivity modeling of periodic two-dimensional nanocomposites", *Physical Review B - Condensed Matter and Materials Physics*, Vol. 69, No. 19, pp. 1–10, 2004.

92. Volz, S., *Microscale and Nanoscale Heat Transfer*, Springer-Verlag Berlin Heidelberg, 1st edition, 2007.

93. Fiveland, W. A., "Selection of discrete ordinate quadrature sets for anisotropic scattering", *American Society of Mechanical Engineers, Heat Transfer Division, HTD*, Vol. 160, pp. 89–96, 1991.

94. Versteeg, H. and W. Malalasekera, *An Introduction to Computational Fluid Dynamics: The Finite Volume Method*, Pearson, 2nd edition, 2007.

95. Scarborough, J. B., *Numerical Mathematical Analysis*, The Johns Hopkins University Press, 6th edition, 1966.

96. Tu, J., G. H. Yeoh and C. Liu, *Computational fluid dynamics: A practical approach*, Butterworth-Heinemann, 3rd edition, 2018.

97. Leonard, B. P., "A stable and accurate convective modelling procedure based on quadratic upstream interpolation", *Computer Methods in Applied Mechanics and Engineering*, Vol. 19, No. 1, pp. 59–98, 1979.

98. Price, H. S., R. S. Varga and J. E. Warren, "Application of Oscillation Matrices to Diffusion-Convection Equations", *Journal of Mathematics and Physics*, Vol. 45, pp. 301–311, 1966.

99. Chen, G., "Thermal conductivity and ballistic-phonon transport in the cross-plane direction of superlattices", *Physical Review B - Condensed Matter and Materials Physics*, Vol. 57, No. 23, pp. 14958–14973, 1998.

100. Karmalkar, S. and U. K. Mishra, "Enhancement of breakdown voltage in AlGaN/GaN high electron mobility transistors using a field plate", *IEEE Transactions on Electron Devices*, Vol. 48, No. 8, pp. 1515–1521, 2001.

101. Asif Khan, M., A. Bhattarai, J. N. Kuznia and D. T. Olson, "High electron mobility transistor based on a GaN-AlxGa 1-xN heterojunction", *Applied Physics Letters*, Vol. 63, No. 9, pp. 1214–1215, 1993.

102. Heller, E., S. Choi, D. Dorsey, R. Vetury and S. Graham, "Electrical and structural dependence of operating temperature of AlGaN/GaN HEMTs", *Microelectronics Reliability*, Vol. 53, No. 6, pp. 872–877, 2013.

103. Šodan, V., H. Oprins, S. Stoffels, M. Baelmans and I. De Wolf, "Influence of Field-Plate Configuration on Power Dissipation and Temperature Profiles in AlGaN/GaN on Silicon HEMTs", *IEEE Transactions on Electron Devices*, Vol. 62, No. 8, pp. 2416–2422, 2015.

104. Ashok, A., D. Vasileska, O. L. Hartin and S. M. Goodnick, "Electrothermal monte carlo simulation of GaN HEMTs including electronelectron interactions", *IEEE Transactions on Electron Devices*, Vol. 57, No. 3, pp. 562–570, 2010.

105. Sadi, T., R. W. Kelsall and N. J. Pilgrim, "Investigation of self-heating effects in submicrometer GaN/AlGaN HEMTs using an electrothermal Monte Carlo method", *IEEE Transactions on Electron Devices*, Vol. 53, No. 12, pp. 2892–2900, 2006.

106. Synopsys, *Sentaurus TCAD User's Manual*, 2009.

107. Kara, D. and F. N. D. Akgun, "Electrothermal analysis of the field-plated AlGaN/GaN HEMTs with SiO 2 passivation", *ASME 2017 International Technical Conference and Exhibition on Packaging and Integration of Electronic and Photonic Microsystems, InterPACK 2017, collocated with the ASME 2017 Conference on Information Storage and Processing Systems*, pp. 1–6, 2017.

108. Yu, L. S., D. J. Qiao, Q. J. Xing, S. S. Lau, K. S. Boutros and J. M. Redwing, "Ni and Ti Schottky barriers on n-AlGaN grown on SiC substrates", *Applied Physics Letters*, Vol. 73, No. 2, pp. 238–240, 1998.

109. Donmezer, F. N., W. James and S. Graham, "The Thermal Response of Gallium Nitride HFET Devices Grown on Silicon and SiC Substrates", *ECS Transactions*, Vol. 41, pp. 13–30, 2011.

110. Ambacher, O., J. Smart, J. R. Shealy, N. G. Weimann, K. Chu, M. Murphy, W. J. Schaff, L. F. Eastman, R. Dimitrov, L. Wittmer, M. Stutzmann, W. Rieger and J. Hilsenbeck, "Two-dimensional electron gases induced by spontaneous and piezoelectric polarization charges in N- And Ga-face AIGaN/GaN heterostructures", *Journal of Applied Physics*, Vol. 85, No. 6, pp. 3222–3233, 1999.

111. Dundar, C. and N. Donmezer, "Thermal characterization of field plated AlGaN/GaN HEMTs", *InterSociety Conference on Thermal and Thermomechanical Phenomena in Electronic Systems, ITHERM*, pp. 755–760, 2019.

112. Cappelluti, F., M. Furno, A. Angelini, F. Bonani, M. Pirola and G. Ghione, "On

the substrate thermal optimization in SiC-based backside-mounted high-power GaN FETs", *IEEE Transactions on Electron Devices*, Vol. 54, No. 7, pp. 1744–1752, 2007.

113. Cho, J., Z. Li, E. Bozorg-Grayeli, T. Kodama, D. Francis, F. Ejeckam, F. Faili, M. Asheghi and K. E. Goodson, "Improved thermal interfaces of GaN-Diamond composite substrates for HEMT applications", *IEEE Transactions on Components, Packaging and Manufacturing Technology*, Vol. 3, No. 1, pp. 79–85, 2013.

114. Batten, T., J. W. Pomeroy, M. J. Uren, T. Martin and M. Kuball, "Simultaneous measurement of temperature and thermal stress in AlGaN/GaN high electron mobility transistors using Raman scattering spectroscopy", *Journal of Applied Physics*, Vol. 106, No. 9, pp. 1–4, 2009.

115. Choi, S., E. R. Heller, D. Dorsey, R. Vetury and S. Graham, "Thermometry of AlGaN/GaN HEMTs using multispectral raman features", *IEEE Transactions on Electron Devices*, Vol. 60, No. 6, pp. 1898–1904, 2013.

116. Choi, S., *Stress Metrology And Thermometry of AlGaN/GaN HEMTs Using Optical Methods*, Ph.D. Thesis, Georgia Institute of Technology, 2013.

117. Mayer, P. M., D. Lüerßen, R. J. Ram and J. A. Hudgings, "Theoretical and experimental investigation of the thermal resolution and dynamic range of CCD-based thermoreflectance imaging", *Journal of the Optical Society of America A*, Vol. 24, No. 4, pp. 1156–1163, 2007.

118. Kendig, D., A. A. Tay and A. Shakouri, "Thermal imaging based on Thermoreflectance addresses the challenges for thermal analysis of today's advanced complex devices", *2016 17th International Conference on Electronic Packaging Technology, ICEPT 2016*, pp. 1517–1521, 2016.

119. Pavlidis, G., D. Kendig, E. R. Heller and S. Graham, "Transient Thermal Char-

acterization of AlGaN/GaN HEMTs Under Pulsed Biasing", *IEEE Transactions on Electron Devices*, Vol. 65, No. 5, pp. 1753–1758, 2018.

120. Pokatilov, E. P., D. L. Nika and A. A. Balandin, "Phonon spectrum and group velocities in AlN/GaN/AlN and related heterostructures", *Superlattices and Microstructures*, Vol. 33, No. 3, pp. 155–171, 2003.